

UNIVERSITY OF BELGRADE
FACULTY OF PHYSICS

Marko Milivojević

SPIN-ORBIT INTERACTION IN
LOW DIMENSIONAL
SYSTEMS: SYMMETRY BASED
APPROACH

Doctoral Dissertation

Belgrade, 2019.

UNIVERZITET U BEOGRADU
FIZIČKI FAKULTET

Marko Milivojević

SPIN-ORBIT INTERAKCIJA
U NISKODIMENZIONALNIM
SYSTEMIMA: SIMETRIJSKI
PRISTUP

doktorska disertacija

Beograd, 2019.

Mentor: dr Tatjana Vuković, vanredni profesor

Fizičkog fakulteta Univerziteta u Beogradu

Članovi komisije: dr Tatjana Vuković, vanredni profesor

Fizičkog fakulteta Univerziteta u Beogradu

dr Milan Damjanović, redovni profesor

Fizičkog fakulteta Univerziteta u Beogradu

dr Vladimir Damljanović, viši naučni saradnik

Instituta za fiziku Univerziteta u Beogradu

dr Saša Dmitrović, docent

Fizičkog fakulteta Univerziteta u Beogradu

dr Nataša Lazić, naučni saradnik

Fizičkog fakulteta Univerziteta u Beogradu

Datum odbrane: _____

Ova disertacija je rađena pod rukovodstvom prof. dr Tatjane Vuković. Zahvaljujem se Tatjani Vuković, Saši Dmitroviću, Milanu Damnjanoviću i Nataši Lazić na razumevanju i svesrdnoj pomoći prilikom izrade ovog rada.

Spin-orbit interakcija u niskodimenzionalnim sistemima: simetrijski pristup

REZIME

Koncept dvostrukih grupa je primenjen na simetrijsku analizu efekata spin-orbit interakcije u niskodimenzionalnim sistemima. Prvi zadatak je konstrukcija dvostrukih grupa za grupu geometrijskih simetrija datog sistema, zajedno sa skupom ireducibilnih reprezentacija. Koristeći simetriju razmatranog sistema i dobijene ireducibilne reprezentacije, može se odrediti da li spin-orbit interakcija izaziva cepanje orbitalnih zona. Klebš-Gordanova serija tenzorskog proizvoda ireducibilnih reprezentacija koje karakterišu orbitalne zone i spinske reprezentacije pruža informaciju da li cepanje zona postoji, dok malo suptilnija grupno-teorijska analiza pokazuje da li je cepanje orbitalnih bendova praćeno ukidanjem spinske degeneracije. Korišćenjem tehnike modifikovanih grupnih projektora, svojstveni problem Hamiltonijana koji opisuje dinamiku sistema se može rešiti numerički, čime se dobijaju elektronske zone sa pridruženim ireducibilnim reprezentacijama i kvantnim brojevima obične/dvostruke grupe. Konačno, razni efekti spin-orbit interakcije se razmatraju kvalitativno ili numerički, uključujući predikciju veličine cepanja zona i analizu spinske polarizacije.

Geometrijske simetrije kvazi-jednodimenzionalnih sistema su opisane grupama koje pripadaju jednoj od 13 beskonačnih familija linijskih grupa. Da bi se ispitali efekti spin-orbit interakcije u kvazi-jednodimenzionalnim sistemima, dvostruke linijske grupe i njihove ireducibilne reprezentacije su konstruisane. Na osnovu tih rezultata pokazuje se da je spinsko cepanje zabranjeno u familijama 6-13 zbog simetrije vertikalne ogledalske ili klizne ravni. Ukoliko je i vremenska inverzija θ uključena u analizu, ispostavlja se da samo grupe iz familija 1 i 5 dozvoljavaju spinsko cepanje zona, jer zajedničko delovanje horizontalne ogledalske ili roto-refleksione ravni sa θ zabranjuje ukidanje spinske degeneracije zona. Dobijeni rezultati ove analize su kasnije primenjeni na ugljenične i MoS₂ nanotube.

Izvršena je detaljna simetrijski zasnovana analiza efekata spin-orbit interakcije u ugljeničnim nanotubama. Kod kiralnih nanotuba se pokazuje da je nenulta očekivana vrednost $\mathbb{1}_o \otimes \sigma$ duž ose tube. Takođe, pravilo nepresecanja zona uništava ukupnu spinsku polarizaciju zone. Specijalna pažnja je posvećena razlici u eksperimentalnim

i teorijskim predviđanjima veličine spinskog cepanja najniže provodne zone u kvazi-metalnim tubama. Dobijeni rezultati pokazuju da postoji anizotropija cepanja valentnih i provodnih zona oko Fermi nivoaa; ona je vrlo osjetljiva na konfiguraciju tube i primenjeno aksijalno istezanje. Aksijalno istezanje drastično povećava cepanje najniže provodne zone, tako da njegovo prisustvo u eksperimentu može biti potencijalno objašnjenje gore navedene razlike između prethodnih teorijskih i eksperimentalnih rezultata.

Simetrije kvazi-dvodimenzionalnih sistema su opisane sa 80 diperiodičnih grupa. Ovde je konstruisana samo dvostruka Dg78 grupa, zajedno sa njenim ireducibilnim reprezentacijama, koja je grupa simetrije familije prelaznih metal-dihalogenidnih slojeva. Efekti spin-orbit interakcije u ovim sistemima su detaljno razmatrani, predviđajući veliko spinsko cepanje. Sa druge strane, efekti spin-orbit interakcije u metal-dihalogenidnim nanotubama nisu proučavani, iako je spinsko cepanje u ugljeničnim nanotubama, u poređenju sa grafenom, često pripisivano postojanju krivine. Među kvazi-dvodimenzionalnim metal-dihalogenidnim materijalima, MoS₂ je najviše proučavana familija, sto je motivisalo fokusiranje upravo na te nanotube. Uvid u rezultate dobijene za tube daje metod savijanja zona sloja MoS₂ i njegova simetrija Dg78, koja omogućava dodeljivanje kvantnih brojeva ireducibilnih reprezentacija elektronskim zonama sloja. Simetrija sloja objašnjava zašto duž određenih pravaca Briluenove zone ne postoji cepanje elektronskih zona, daje detaljan uvid u njihovo cepanje (kada ono postoji), i određuje koje su dozvoljene orbitale u valentnim i provodnim zonama. Konačno, data je analiza efekata spin-orbit interakcije u MoS₂ nanotubama. Kao i u ugljeničnim nanotubama, simetrija daje kvantne brojeve zona koje se ne cepaju kada je uključena spin-orbit interakcija. U odnosu na sloj, u nekim tačkama Briluenove zone cepanje je značajno smanjeno, dok je u drugim tačkama krivina uticala na njegovo povećanje. Dakle, krivina ne utiče uvek povoljno na efekte spin-orbit interakcije.

KLJUČNE REČI: Ugljenične i MoS_2 nanotube, dvostruke grupe, spin-orbit interakcija, spinsko cepanje

NAUČNA OBLAST: Fizika

UŽA NAUČNA OBLAST: Kvantna, matematička i nanofizika (Fizika kondenzovane materije)

UDK BROJ: 538.9

Spin-orbit interaction in low dimensional systems: symmetry based approach

SUMMARY

In order to perform full symmetry analysis of spin-orbit coupling effects on the electronic band structure in low dimensional systems, concept of double groups is applied. First goal is to construct double group of system's geometrical symmetries, along with the set of irreducible representations. Occurrence of orbital band splitting depends purely on the symmetry of the studied system. Clebsch-Gordan series of the tensor product of irreducible representations characterising orbital bands and spin representation provide an information about band splitting, while further symmetry based analysis can show whether obtained splitting of orbital bands is followed by the removal of initial spin degeneracy. Finally, using the modified group projected technique, eigenproblem of the Hamiltonian describing the dynamics of the system is solved numerically. This provides electronic bands assigned by quantum numbers labeling the irreducible representations of single/double groups. Study of spin-orbit coupling effects is then enabled, including the magnitude of the predicted splitting and the study of spin polarization.

Geometrical symmetries of quasi-one dimensional systems are described by groups belonging to the one of 13 infinite families of line groups. In order to investigate spin-orbit coupling effects in quasi-one dimensional systems, all double line groups and their irreducible representations are constructed. Based on these results, it is shown that spin splitting is forbidden in families 6-13 due to vertical mirror or glide plane symmetry. If the time reversal symmetry θ is taken into account, only groups from families 1 and 5 allow spin splitting, since the joint action of horizontal mirror plane or roto-reflection with θ preserves spin degeneracy of the bands. These results are then applied to MoS_2 and single walled carbon nanotubes.

First, thorough symmetry based analysis of spin-orbit coupling effects in single walled carbon nanotubes is performed. For chiral nanotubes, it is proved that nonzero expectation value of $\mathbb{1}_o \otimes \sigma$ must be along the tube's axis. Also, non-crossing rule may destroy the overall band polarization. Special attention was given to the

existing contradictory experimental and theoretical calculations regarding the magnitude of spin splitting in quasi-metallic tubes. It is shown that anisotropic electron and hole splitting near Fermi level is indeed present, but it is highly sensitive on the tube's configuration and applied axial strain, i.e. opposite results regarding the ratio of the magnitude of top valence and lowest conductance bands splitting is obtained. This can be the possible answer of the reported discrepancy, since in an experimental setup a small strain can be indeed present, contributing significantly to the measured results.

Symmetries of quasi-two dimensional systems are gathered into 80 diperiodic groups. Here, only the double group of Dg78 is constructed, along with its irreducible representations; this is the symmetry group of a larger family of transition-metal dichalcogenide monolayers. Spin-orbit coupling effects in these systems have been intensively studied, predicting large spin splitting. Although the order of magnitude larger spin splitting in single walled carbon nanotubes, in comparison to graphene, is attributed to the curvature effect, study of spin-orbit coupling effects in transition-metal dichalcogenide nanotubes is lacking. As among transition-metal dichalcogenide materials, MoS₂ is the best studied family, spin-orbit coupling effects in MoS₂ nanotubes are investigated. In order to elucidate results obtained for the tubes, double Dg78 diperiodic group is applied in order to obtain monolayer electronic bands, assigned by relevant quantum numbers. Symmetry of the monolayer also explains the observed absence of band splitting in particular directions in the Brillouin zone, yielding better insight on the band splitting and orbital contribution in the top valence and the lowest conductance band. Finally, analysis of spin-orbit coupling effects in MoS₂ nanotubes is given. As in single walled carbon nanotubes, symmetry points to quantum numbers of bands which do not split when spin-orbit coupling effects are included. For these which do split, results show significantly suppressed band splitting in some points of the Brillouin zone, compared to the related monolayer values, while in some other points we indeed see the increase of splitting. Thus, curvature does not necessarily enhance spin-orbit coupling effects.

KEYWORDS: Carbon and MoS₂ nanotubes, double groups, spin-orbit interaction, spin splitting

SCIENTIFIC FIELD: Physics

SCIENTIFIC DISCIPLINE: Quantum physics, mathematical physics and nanophysics
(Condensed matter physics)

UDC NUMBER: 538.9

Contents

Introduction	1
1 Symmetry in composite orbital and spin space	4
1.1 Double groups	4
1.1.1 Euclidean group	5
1.1.2 Double Euclidean group	5
1.2 Symmetry of Q1D systems: Line groups	7
1.2.1 Structural properties	7
1.2.2 Irreducible representations of line groups	12
1.2.3 Construction of DLGs	13
1.2.4 Construction of IRs	14
2 Spin-orbit interaction	19
2.1 Origin of SOC	19
2.2 Perturbative approach	22
2.3 Symmetry and SOC in Q1D crystals	24
3 Spin-orbit interaction in SWCNTs	31
3.1 Full geometrical symmetry of SWCNTs	33
3.1.1 Symmetry-adapted relaxation procedure	35
3.2 SOC induced effects in SWCNTs	37
3.2.1 Symmetry based analysis of SOC effects	39
3.2.2 Effects of strain on the magnitude of SOC induced splitting	43
4 Spin-orbit interaction in MoS₂ nanotubes	46
4.1 MoS ₂ monolayer	47
4.1.1 Double group of Dg78	48

4.1.2	SOC effects for the monolayer	50
4.2	MoS ₂ nanotubes	55
4.2.1	Armchair tubes	60
4.2.2	Zig-zag tubes	64
4.2.3	Chiral tubes	68
4.3	Curvature effects on orbital contribution	70
4.3.1	Armchair tubes	71
4.3.2	Zig-zag tubes	76
4.3.3	Chiral tubes	76
Conclusions		81
A Irreducible representations of direct product of groups		84
B Induction procedure		85
B.1	Induction from the invariant subgroup of index 2	86
B.2	Group is semidirect product of its subgroups	86
C Tables of the IRs of DLGs		88

Introduction

Spintronics [1–3], a growing field in the context of electronics, is focused on manipulation of the electron spin. Initially, usage of external magnetic fields was proposed to achieve this goal, but magnetic fields are hard to control at the nanoscale. This difficulty has motivated proposals for spin manipulation by using different spin-orbit coupling (SOC) mechanisms. In solids, spin dependent structure of the electronic bands occurs due to the crystal potential (Dresselhaus effect) [4], vibrational potential of the crystal (spin-phonon coupling) [5–8] or external electric field (Rashba effect) [9, 10].

Band theory of solids is tightly connected to symmetry. Irreducible representations (IRs) of a crystal’s symmetry group can be used to reduce the eigenproblem of the Hamiltonian and get the bands and corresponding eigenstates assigned by quantum numbers (QNs), enabling further applications of selection rules. If SOC is neglected and only the orbital degree of freedom of the electrons are considered, single groups are used, and the obtained orbital bands are thus spin degenerated. Since configurations in space can be three-dimensional, quasi-two dimensional (Q2D) or quasi-one dimensional (Q1D), space groups [11], diperiodic groups [12] and line groups [13], respectively, and their IRs are needed in order to classify and analyse energy bands.

The impact of SOC on the energy bands in solid state systems was first noticed by Elliot [14] and Dresselhaus et al. [15]. Besides topology, SOC also effects the number of bands, since splitting of the orbital bands may occur. Dresselhaus [4] observed that in zinc-blend structures SOC induces band splitting which cancels spin degeneration of the orbital bands, i.e. the so called spin splitting of the bands occurs. This effect (named Dresselhaus effect) is present in crystals without spatial inversion symmetry. If the system has spatial inversion symmetry then, for example, electric field can be used to break this symmetry and induce the spin splitting of

the bands (Rashba effect) [9, 10]. Clearly, the symmetry of the system provides the clarification of the observed impact of SOC.

Proper symmetry analysis of SOC needs to include the full symmetry group of the studied system. When the electron spin degree is included, the action of geometrical transformations on the orbital part of wave function is accompanied by its counterpart in the spin space. It is well known that to each element of the rotational group $\mathbf{SO}(3)$ two elements of the group $\mathbf{SU}(2)$ are assigned in the spin space; on the other hand, spatial inversion and translations act trivially on spin. In order to avoid working with two-valued representations, in physics concept of double groups is introduced [16–19].

Bethe [16] and Opechowski [17] have classified double point groups and their method was easily extended to space groups [11]. However, in Q1D and Q2D crystals, double groups are lacking. The subject of this dissertation, full symmetry analysis of spin dynamics of Q1D systems, assumes derivation of double group symmetries of these structures. Since their geometrical symmetries are described by the line groups [13], the first goal is to derive double line groups (DLGs). First, IRs of DLGs are found, enabling analysis of SOC effects. General results are then applied on concrete systems, giving an insight into all the advantages of symmetry based analysis. We have particularly focused on MoS_2 and single walled carbon nanotubes (SWCNTs), as these are one of the most studied Q1D systems.

Assuming that external fields are not present, within the Born-Oppenheimer approximation the only potential that couples spin and orbital degrees of freedom is the crystal potential. More concretely, we have included Dresselhaus SOC in the on-site approximation. Atomic (on-site or $\mathbf{l} \cdot \mathbf{s}$) approximation assumes that SOC contribution is relevant only close to the atomic cores. Atomic SOC is equal to $\lambda_{so}\mathbf{l} \cdot \mathbf{s}$, where \mathbf{l} is an orbital angular momenta, while $\mathbf{s} = 1/2\boldsymbol{\sigma}$ is electron spin 1/2 operator. In the case of MoS_2 nanotubes, Dresselhaus SOC was not analyzed before, while SOC effects in SWCNTs were studied in several papers. It was shown that spin splitting is possible only in chiral SWCNTs [20, 21], while in the achiral case only band splitting can be present. Furthermore, spin splitting of the top valence and the bottom conductance band was investigated in chiral SWCNTs. Theoretical predictions [22] have confirmed the first experimental results [23]. However, another experimental data [24] do not accommodate to theory and, up to the author’s knowledge, this discrepancy is still unresolved.

To summarize, after the introductory part, the thesis gives a brief overview of Euclidean group and its double group. Afterwards, recapitulation of the line groups is given, DLGs are constructed and corresponding IRs are determined (derived tables of IRs are gathered in Appendix C). In Chapter 2, SOC Hamiltonian is introduced and general remarks about the perturbational approach in the study of SOC effects are given. In the case of Q1D systems, DLG IRs are used in the analysis of spin splitting and spin polarization of the bands. Furthermore, the formalism of DLGs and the modified group projector technique [25] were applied in the study of SOC effects in SWCNTs. We were able to address the discrepancy of the observed experimental and theoretical results, thus closing the mentioned gap in the literature (Chapter 3). It is particularly interesting to mention that in layered carbon system, i.e. graphene, SOC effect is negligible. On the other hand, since in SWCNTs spin splitting is on the meV scale (can be experimentally detected), many authors have attributed this behaviour to the curvature effects. In order to test this hypothesis, we have focused on MoS₂ nanotubes and its layered counterpart. SOC effects in MoS₂ monolayer are studied using the double Dg78 diperiodic group, while for MoS₂ nanotubes groups from DLG families 1, 4 and 8 are needed. Our results show that curvature effects significantly suppress band splitting in some points of the Brillouin zone, although in some others band splitting values are indeed increased, as compared to the layer. Also, SOC interaction effects are more pronounced in the valence bands than in the conductance. In the chiral case, SOC causes spin polarization of the bands, while in the armchair and zig-zag case, band splitting with zero spin polarization is present (Chapter 4).

Chapter 1

Symmetry in composite orbital and spin space

When the spin degree of freedom is included, it is well known that projective (two-valued) representations [26] have to be used. Instead, in physics the group-theoretical apparatus of double groups [16–19] and their IRs are commonly applied to naturally incorporate the spin into the electronic band picture. This approach enables the use of concepts and methods developed for ordinary, i.e. single-valued, representations.

As symmetry groups of low dimensional systems are subgroups of the Euclidean group, in this Chapter we first give short overview of the Euclidean group and its double group [27]. Special attention is paid to double groups of its subgroups, being important for constructing DLGs and double diperiodic groups. Next Section is devoted to the symmetries of Q1D systems, comprised of short introduction on line group structure, their IRs and, finally, results regarding the DLGs. On the other hand, as symmetry group of a Q2D systems is one of 80 diperiodic groups, in Chapter 4 we will construct only the double group of diperiodic group Dg78, along with their IRs, which is relevant for the transition-metal dichalcogenide monolayers [12].

1.1 Double groups

Here, we present general considerations on the structure of double groups, introducing the notation that will be used in this work.

1.1.1 Euclidean group

Each geometrical (point, line, diperiodic or space) group \mathbf{G} of the physical system is a subgroup of the Euclidean group $\mathbf{E}(3)$. As well known, the three-dimensional translational group \mathbf{T} is the invariant subgroup of $\mathbf{E}(3)$, and the Euclidean group can be written as a semidirect product of \mathbf{T} and the orthogonal group $\mathbf{O}(3)$

$$\mathbf{E}(3) = \mathbf{T} \ltimes \mathbf{O}(3). \quad (1.1)$$

On the other hand, orthogonal group is a direct product of the rotational group $\mathbf{SO}(3)$ and the cyclic group $\mathbf{C}_J = \{e, J\}$ of order two, generated by the spatial inversion J . Thus, Euclidean group can be factorized as

$$\mathbf{E}(3) = \mathbf{T} \ltimes (\mathbf{SO}(3) \otimes \mathbf{C}_J), \quad (1.2)$$

with its elements

$$g = g(j, \phi, \mathbf{n}, \mathbf{t}) = (J^j R(\phi, \mathbf{n}) | \mathbf{t}), \quad (1.3)$$

counted by $j = 0, 1$, two three-dimensional real vectors \mathbf{n} , \mathbf{t} and parameter ϕ . Furthermore, $R(\phi, \mathbf{n})$ is rotation for $\phi \in [0, 2\pi)$ around the axis defined by the unit vector \mathbf{n} , while \mathbf{t} is a translational vector. The identity element of $\mathbf{E}(3)$ is denoted by $e = (\mathbf{1}_3 | 0)$.

1.1.2 Double Euclidean group

When the half-integer spin degree of freedom is taken into account, two antipodal elements

$$\pm u(\phi, \mathbf{n}) = \pm e^{\frac{i}{2}\phi \mathbf{n} \cdot \boldsymbol{\sigma}} \quad (1.4)$$

from the covering double group $\mathbf{SU}(2)$ of $\mathbf{SO}(3)$ correspond to each rotation $R(\phi, \mathbf{n})$. Since the spatial inversion and translations do not change the spin, there is an unique double extension

$$\tilde{\mathbf{E}}(3) = \mathbf{T} \ltimes (\mathbf{SU}(2) \otimes \mathbf{C}_J) \quad (1.5)$$

of the Euclidean group $\mathbf{E}(3)$, with elements

$$\tilde{g} = \tilde{g}(j, \phi, \mathbf{n}, \mathbf{t}) = (J^j u(\phi, \mathbf{n}) | \mathbf{t}), \quad \phi \in [0, 4\pi), \quad (1.6)$$

such that the covering homomorphism \mathcal{F} of $\tilde{\mathbf{E}}(3)$ onto $\mathbf{E}(3)$ is the unique trivial (with respect to \mathbf{T} and \mathbf{C}_J) extension of the canonical homomorphism (mapping

$\pm u(\phi, \mathbf{n})$ into $R(\phi, \mathbf{n})$) of $SU(2)$ onto $SO(3)$. Thus, the Euclidean group is identified with $\tilde{\mathbf{E}}(3)/\ker(\mathcal{F})$.

Automatically, for each $g \in \mathbf{E}(3)$ there exist two antipodal elements \tilde{g} and \tilde{g}' such that

$$\mathcal{F}(\tilde{g}) = \mathcal{F}(\tilde{g}') = g. \quad (1.7)$$

Since $\ker(\mathcal{F}) = \{\tilde{e}, \tilde{e}'\}$, where $\tilde{e} = \tilde{g}(0, 0, \mathbf{n}, 0)$ is the group identity for arbitrary \mathbf{n} , while $\tilde{e}' = \tilde{g}(0, 2\pi, \mathbf{n}, 0)$ is rotation for 2π (the only involution in $\tilde{\mathbf{E}}(3)$ which commutes with all its elements), connection between \tilde{g}' and \tilde{g} is the following:

$$\tilde{g}' = \tilde{e}'\tilde{g}. \quad (1.8)$$

It is convenient to identify the elements of $\tilde{\mathbf{E}}(3)$ with the pairs $\tilde{g} = \{g, u\}$ (where $g = g(j, \phi, \mathbf{n}, \mathbf{t})$ and $u = u(\phi, \mathbf{n})$), which act on the pair $\{\mathbf{r}, \mathbf{s}\}$ of spatial (from \mathbb{R}^3) and spin vector (from \mathbb{C}^2) as:

$$\tilde{g}\{\mathbf{r}, \mathbf{s}\} = \{g\mathbf{r}, u\mathbf{s}\} = \{(J^j R(\phi, \mathbf{n}) | \mathbf{t})\mathbf{r}, u(\phi, \mathbf{n})\mathbf{s}\}. \quad (1.9)$$

This is isomorphic presentation, since both components are homomorphisms with the trivial intersection of the kernels. Namely, according to (1.9), g is the image of \tilde{g} by \mathcal{F} , while $u(\tilde{g}(j, \phi, \mathbf{n}, \mathbf{t})) = u(\phi, \mathbf{n})$ is a linear representation of $\tilde{\mathbf{E}}(3)$, with kernel $\mathbf{T} \wedge \mathbf{C}_J$ (as all $u(\tilde{g}(j, 0, \mathbf{n}, \mathbf{t})) = \mathbb{1}$). Representation $u(\tilde{g}(j, \phi, \mathbf{n}, \mathbf{t})) = u(\phi, \mathbf{n})$ will be called *natural spin representation*. In particular, for mirror plane orthogonal to \mathbf{n} , $\sigma_{\mathbf{n}} = JR(\pi, \mathbf{n})$, the natural representation is $u(\tilde{\sigma}_{\mathbf{n}}) = u(\tilde{g}(1, \pi, \mathbf{n}, 0)) = i\mathbf{n} \cdot \boldsymbol{\sigma}$.

For any subgroup \mathbf{G} of the Euclidean group, Noether's isomorphism theorem¹ shows that there is unique double group

$$\tilde{\mathbf{G}} = \mathcal{F}^{-1}(\mathbf{G}) \quad (1.10)$$

of \mathbf{G} , being the subgroup of $\tilde{\mathbf{E}}(3)$ which contains $\ker(\mathcal{F})$ and satisfies

$$\mathcal{F}(\tilde{\mathbf{G}}) = \tilde{\mathbf{G}}/\ker(\mathcal{F}) = \mathbf{G}. \quad (1.11)$$

Finally, we will illustrate the gathered results on the example of cyclic groups, being the starting point in the construction of groups relevant in different types of problems in physics. For cyclic group \mathbf{G} generated by g of order $|g|$, if and only if

$$\tilde{g}^{|g|} = \tilde{e}', \quad (1.12)$$

¹In group theory, Noether isomorphism theorem is often referred as the first group isomorphism theorem; see, for example, mathworld.wolfram.com/FirstGroupIsomorphismTheorem.html

its double group $\tilde{\mathbf{G}}$ is cyclic, generated by \tilde{g} (of order $2|g|$). If the relation (1.12) is not satisfied, double group is equal to

$$\tilde{\mathbf{G}} = \mathbf{G}' \otimes \ker(\mathcal{F}) = \mathbf{G}' \otimes \{\tilde{e}, \tilde{e}'\}, \quad (1.13)$$

where \mathbf{G}' is cyclic (isomorphic to \mathbf{G}), generated by \tilde{g} (of order $|g|$).

Specifically, cyclic finite subgroups of $\mathbf{SO}(3)$ (generated by $R(\frac{2\pi}{n}, \mathbf{n})$) and mirror plane groups $\{e, \sigma_{\mathbf{n}} = JR(\pi, \mathbf{n})\}$ have cyclic double groups with $|\tilde{R}(\frac{2\pi}{n}, \mathbf{n})| = 2n$ and $|\tilde{\sigma}_{\mathbf{n}}| = 4$, respectively.

The double group of the roto-reflectional group \mathbf{S}_{2n} , generated by $g = (JR(\pi + \frac{\pi}{n}, \mathbf{n}) | 0)$ (of order $|g| = n$) is cyclic if n is odd, while otherwise it is of the product type (1.13). Double \mathbf{C}_J group is also cyclic, as well as double infinite groups (translational, helical axis and glide plane group).

1.2 Symmetry of Q1D systems: Line groups

A Q1D system is comprised of monomers periodically arranged along one direction, conventionally denoted as z-axis. Geometrical symmetry groups of such systems are called line groups [13]. Unlike for the case of 3D and 2D periodic systems, there are infinitely many symmetry groups of Q1D systems which, on the other hand, are gathered within 13 infinite families of line groups. Their structure and IRs have been successfully used in study of various properties of nanotubes [13, 28–31]. First, we give brief remainder of the line groups and necessary details regarding their IRs. Next, DLGs are constructed along with their IRs, following [27].

1.2.1 Structural properties

Periodic system is a system generated with the help of pure translations from its minimal part, called an *elementary cell*. However, a Q1D system can be an infinite chain of monomers regularly arranged along z-axis (not necessarily possessing the translational symmetry), i.e. it can be generated from a single monomer by the action of more general geometric transformation $g = (X|\mathbf{f})$. Here, translational part $\mathbf{f} = f\mathbf{e}_z$ may be period, or its part (fractional translation); however, in some cases, so called *incommensurate*, there is no translational period at all. Another part of g is the orthogonal transformation X , which must leave z-axis invariant. As $g^2 = (X|\mathbf{f})^2 = (X^2|X\mathbf{f} + \mathbf{f})$, this allows only one possible action of X on \mathbf{e}_z if

we want to generate the infinite system: $X\mathbf{e}_z = \mathbf{e}_z$. Only two types of orthogonal transformations have this feature: rotation C_Q around z-axis for an angle $\frac{2\pi}{Q}$ (here Q can be any real number, but for the sake of uniqueness we use $Q \geq 1$; note that $Q=1$ gives identity transformation $C_1 = \mathbb{1}_3$) and vertical mirror plane σ_v (i.e. any plane containing the z-axis). Mirror plane symmetries are involutions, so we have $g^2 = (\mathbb{1}_3|2\mathbf{f})$, i.e. the system has a translational period $\mathbf{a} = 2\mathbf{f}$. Further on, we will use convention to write f and a instead of \mathbf{f} and \mathbf{a} (keeping in mind the z direction of the vectors).

Thus, we can construct two types of groups \mathbf{Z} which are cyclic and infinite:

1. *screw axes group* $\mathbf{T}_Q(f)$ generated using $g_{\mathbf{Z}} = (C_Q|f)$,
2. *glide plane group* $\mathbf{T}'(a/2)$ generated using $g_{\mathbf{Z}} = (\sigma_v|a/2)$.

Arrangement defined by the screw axis group is translationally periodic if there is a translational subgroup $\mathbf{T}(a)$ of $\mathbf{T}_Q(f)$. We will call this type of system, *commensurate* in order to distinguish it from *incommensurate* which do not have translational periodicity. Translational group is also cyclic: generated by element $(\mathbb{1}_3|a)$. In order to find the element of $\mathbf{T}_Q(f)$ which is pure translation, we must find minimal natural number q such that $(X|f)^q = (X^q|qf) = (\mathbb{1}_3|a)$. This equation gives us two conditions: $X^q = \mathbb{1}_3$ and $a = qf$. For the screw axis group, the first condition yields $Q = q/r$, where r is a natural number less or equal than q (because $Q \geq 1$), i.e. system has translational periodicity only when Q is a rational number. By the convention we take that q and r are coprimes. Obtained period $a = qf$ means that elementary cell contains q monomers. Generator of the screw axis group becomes $(C_q^r|a/q)$. Especially, for $q = 1$ we obtain pure translational group with $Q = q = r = 1$. For $q > 2$ or irrational Q , generator is usually called helical generator.

To conclude, there are two types of periodic arrangements, which correspond to the generalized translation groups \mathbf{Z} :

1. *screw axis group*, $\mathbf{T}_Q(f)$, generated with the help of $(C_Q|f)$. For the special case of rational $Q = q/r$, screw axis $\mathbf{T}_q^r(f)$ is *commensurate*, with the period $a = qf$; for $q = 1$ and $q = 2$, screw axis group degenerates into *translational* and *zig-zag group*, respectively.

2. *glide plane group*, $\mathbf{T}'(f = a/2)$, generated with $(\sigma_v|a/2)$, has a halving subgroup of pure translations with the period $a = 2f$.

On the other hand, monomer, being a building block of Q1D system, is a finite set of atoms which possesses its own symmetries, gathered into point group \mathbf{P}_M . However, in order to be the symmetry of Q1D systems, an element of \mathbf{P}_M must leave the z-axis unchanged. Maximal such point group is $\mathbf{D}_{\infty h}$, concluding that the axial point group $\mathbf{P} = \mathbf{P}_M \cap \mathbf{D}_{\infty h}$ is a maximal subgroup relevant for Q1D systems. Generators of this subgroup can be rotation C_n for an angle $\phi = 2\pi/n$ around z-axis, rotation U for an angle π around an axis perpendicular to the z-axis, horizontal and vertical glide planes σ_h i σ_v and roto-reflection plane $S_{2n} = C_{2n}\sigma_h$ (note that S_2 is actually spatial inversion J). It turns out that with these operations one can make 7 infinite families of an axial point groups

$$\mathbf{C}_n, \mathbf{S}_{2n}, \mathbf{C}_{nh}, \mathbf{D}_n, \mathbf{C}_{nv}, \mathbf{D}_{nd} \quad \text{and} \quad \mathbf{D}_{nh}, \quad (1.14)$$

while within each family groups differ from one to another by number $n = 1, 2, 3, \dots$, representing the order of a principal axis, i.e. z-axis.

Last part in the construction of the line groups is inquiry of compatibility between intrinsic monomer symmetry \mathbf{P}_M and an arrangement symmetry \mathbf{Z} . We want to construct group \mathbf{L} whose each element $l \in \mathbf{L}$ can be written as a product $\ell = l_Z l_P$, where $l_Z \in \mathbf{Z}$ and $l_P \in \mathbf{P}$. In other words, we wish to find all possible pairs \mathbf{P} and \mathbf{Z} for which the set \mathbf{PZ} has a group structure. Product of two subgroups is a group if and only if the two subgroups commute with one another [32]. In our case, if for every l_P and l_Z there exist l'_P and l'_Z such that $l_P l_Z = l'_Z l'_P$, we obtain a group. Thus, compatibility of each axial point group with every generalized translation group needs to be examined.

Group \mathbf{C}_n is compatible with each generalized translation group $\mathbf{T}_Q(f)$, since rotation C_n commutes with the the generalized translation generator $(C_Q|f)$. Their product $\mathbf{T}_Q(f)\mathbf{C}_n$ comprise the first family line groups $\mathbf{L}^{(1)}$. Line groups from this family are the simplest line groups and are subgroups of all line groups from other families. Screw axis group $\mathbf{T}_Q(f)$ is also compatible with \mathbf{D}_n , because $U(C_Q|f) = (C_Q^{-1}| - f)U$. Horizontal mirror plane commutes with rotations around the z-axis, so $\sigma_h(C_Q^t|tf) = (C_Q^t| - tf)\sigma_h = (C_Q^{-t}| - tf)C_Q^{2t}\sigma_h$. It follows that for every integer t rotation C_Q^{2t} must be an element of \mathbf{P} , i.e. there is an integer s for which $2t/Q = s/n$. Clearly, solution exists only if Q is rational. Solving the condition over s yields

that Q must be of the form $Q = 2n/j$ where $j = 1, 2, \dots$. For j even, generator of the screw axis becomes $(C_Q|f) = (C_{2n}^j|f) = (C_n^{j/2}|f) = C_n^{j/2}(\mathbb{1}_3|f)$, yielding that $f = a$ and $\mathbf{T}_Q(f)\mathbf{C}_n = \mathbf{T}(a)\mathbf{C}_n$. In case of odd j , the generator can be written as $(C_{2n}^j|f) = (C_{2n}^{2j'+1}|f) = (C_{2n}^1|f)C_n^{j'}$, i.e. following sets are identical: $\mathbf{T}_{2n}^j(f)\mathbf{C}_n = \mathbf{T}_{2n}^1(f = a/2)\mathbf{C}_n$. To conclude, we have shown that the following line groups can be constructed: $\mathbf{T}(a)\mathbf{C}_{nh}, \mathbf{T}(a)\mathbf{D}_{nh}, \mathbf{T}_{2n}^1(a/2)\mathbf{C}_{nh}, \mathbf{T}_{2n}^1(a/2)\mathbf{D}_{nh}$. The similar conclusions can be drawn for roto-reflection $S_{2n} = C_{2n}\sigma_h$. As for vertical mirror symmetry σ_v , we test the relation $\sigma_v(C_Q^t|tf) = (C_Q^{-t}|tf)\sigma_v = (C_Q^t|tf)C_Q^{-2t}\sigma_v$, concluding that rotation C_Q^{-2t} must be from \mathbf{P} . Condition $s/n = -2t/Q$ differs from the one for horizontal mirror plane only by sign, thus the compatibility must be the same.

It remains to examine compatibility of \mathbf{P} with the glide plane group $\mathbf{T}'(a/2)$. First, $C_n(\sigma_v|a/2) = (\sigma_v|a/2)C_n^{-1}$ and $\sigma_h(\sigma_v|a/2) = (\sigma_v| - a/2)\sigma_h = (\sigma_v|a/2)^{-1}\sigma_h$, yielding that both $\mathbf{T}'(a/2)\mathbf{C}_n$ and $\mathbf{T}'(a/2)\mathbf{C}_{nh}$ have group structure. If we have another σ'_v , it follows that $\sigma'_v(\sigma_v|a/2) = (C_Q|a/2)$, such that π/Q is the angle between these two vertical planes. As $(C_Q|a/2)^2 = (C_Q^2|a)$, we conclude that these mirror planes coincide (this case actually means that the system has translational period $a/2$, rather than a) or that σ_v bisects two mirror planes from the set $\{\sigma'_v C_n^s|s = 1, 2, \dots, n-1\}$. Similar conclusion can be made for U , i.e. it is in the plane σ_v or σ_v bisects the angle between horizontal axes from \mathbf{P} .

To summarize, we have found all the products of axial point groups \mathbf{P} and groups of generalized translation \mathbf{Z} generating line group $\mathbf{L} = \mathbf{ZP}$. Although with different factors, some of these product are equal, giving different factorizations of the same line group. Since section of \mathbf{P} and \mathbf{Z} is the identity element only, product is at least semi-direct (\wedge , with only the first factor invariant). If both subgroups are invariant subgroups, \mathbf{L} is their direct product (\otimes). In total, there are 13 infinite families of line groups listed in Table 1.1 along with their factorizations, invariant subgroup from the first family, generators and isogonal point group \mathbf{P}_I (point group obtained when the translational part of the line group symmetry is neglected). Each family includes all groups of the specific type differing among each other by parameters n , a , and/or Q , and f . Incommensurate line groups are either from the first or from the fifth family (commensurate between them are excluded by the condition $Q = q/r$), while in all other families generalized translation group is glide plane group, pure translation $\mathbf{T}(a)$ or the zig-zag group $\mathbf{T}_{2n}^1(a/2)$.

Table 1.1: Factorization of the line group families. For every family we give different factorization, subgroup from the first family $\mathbf{L}^{(1)}$, generators and isogonal point group \mathbf{P}_I .

\mathbf{F}	Factorized notation	$\mathbf{L}^{(1)}$	Generators	\mathbf{P}_I
1	$\mathbf{T}_Q \otimes \mathbf{C}_n$	$\mathbf{T}_Q \otimes \mathbf{C}_n$	$(C_Q f), C_n$	\mathbf{C}_q
2	$\mathbf{T} \wedge \mathbf{S}_{2n}$	$\mathbf{T} \otimes \mathbf{C}_n$	$(\mathbb{1}_3 a), S_{2n}$	\mathbf{S}_{2n}
3	$\mathbf{T} \wedge \mathbf{C}_{nh}$	$\mathbf{T} \otimes \mathbf{C}_n$	$(\mathbb{1}_3 a), C_n, \sigma_h$	\mathbf{C}_{nh}
4	$\mathbf{T}_{2n}^1 \mathbf{C}_{nh} = \mathbf{T}_{2n}^1 \mathbf{S}_{2n}$	$\mathbf{T}_{2n}^1 \mathbf{C}_n$	$(C_{2n} \frac{a}{2}), C_n, \sigma_h$	\mathbf{C}_{2nh}
5	$\mathbf{T}_Q \wedge \mathbf{D}_n$	$\mathbf{T}_Q \otimes \mathbf{C}_n$	$(C_Q f), C_n, U$	\mathbf{D}_q
6	$\mathbf{T} \otimes \mathbf{C}_{nv} = \mathbf{C}_{nv} \wedge \mathbf{T}'$	$\mathbf{T} \otimes \mathbf{C}_n$	$(\mathbb{1}_3 a), C_n, \sigma_v$	\mathbf{C}_{nv}
7	$\mathbf{C}_n \wedge \mathbf{T}'$	$\mathbf{T} \otimes \mathbf{C}_n$	$(\sigma_v \frac{a}{2}), C_n$	\mathbf{C}_{nv}
8	$\mathbf{C}_{nv} \wedge \mathbf{T}_{2n}^1 = \mathbf{C}_{nv} \wedge \mathbf{T}'_d$	$\mathbf{T}_{2n}^1 \mathbf{C}_n$	$(C_{2n} \frac{a}{2}), C_n, \sigma_v$	\mathbf{C}_{2nv}
9	$\mathbf{T} \wedge \mathbf{D}_{nd} = \mathbf{T}' \wedge \mathbf{D}_{nd}$	$\mathbf{T} \otimes \mathbf{C}_n$	$(\mathbb{1}_3 a), C_n, U_d, \sigma_v$	\mathbf{D}_{nd}
10	$\mathbf{T}' \mathbf{S}_{2n} = \mathbf{T}'_d \mathbf{D}_n$	$\mathbf{T} \otimes \mathbf{C}_n$	$(\sigma_v \frac{a}{2}), S_{2n}$	\mathbf{D}_{nd}
11	$\mathbf{T} \wedge \mathbf{D}_{nh} = \mathbf{T}' \mathbf{D}_{nh}$	$\mathbf{T} \otimes \mathbf{C}_n$	$(\mathbb{1}_3 a), C_n, U, \sigma_v$	\mathbf{D}_{nv}
12	$\mathbf{T}' \mathbf{C}_{nh} = \mathbf{T}' \mathbf{D}_n$	$\mathbf{T} \otimes \mathbf{C}_n$	$(\sigma_v \frac{a}{2}), C_n, \sigma_h$	\mathbf{D}_{nh}
13	$\mathbf{T}_{2n}^1 \mathbf{D}_{nh} = \mathbf{T}_{2n}^1 \mathbf{D}_{nd} =$ $\mathbf{T}'_d \mathbf{D}_{nh} = \mathbf{T}'_d \mathbf{D}_{nd}$	$\mathbf{T}_{2n}^1 \otimes \mathbf{C}_n$	$(C_{2n} \frac{a}{2}), C_n, U, \sigma_v$	\mathbf{D}_{2nh}

Further, we discuss the relation of different line groups with respect to the first family line group $\mathbf{L}^{(1)}$. Groups of the first family $\mathbf{L}^{(1)}$ are invariant subgroups of index 2 of the groups from the families $\mathbf{L}^{(F')}$ ($F' = 2, \dots, 8$). As evident from the Table 1.1, additional generators for these families are $C_{2n}\sigma_h, \sigma_h, \sigma_h, U, \sigma_v, (\sigma_v|a/2), \sigma_v$, respectively. For families $\mathbf{L}^{(F'')}$ ($F'' = 9, \dots, 13$), a group from the first family $\mathbf{L}^{(1)}$ is an invariant subgroup of index 4, while the groups from the following families $\mathbf{L}^{(F')}$ are invariant subgroups of index 2: $\mathbf{L}^{(6)}, \mathbf{L}^{(7)}, \mathbf{L}^{(7)}, \mathbf{L}^{(7)}, \mathbf{L}^{(8)}$ respectively, with additional generators U_d, U_d, U, U, U . To conclude:

$$\mathbf{L}^{(1)} \stackrel{2}{<} \mathbf{L}^{(F')} \stackrel{2}{<} \mathbf{L}^{(F'')}, \quad (1.15)$$

while each element ℓ of a line group \mathbf{L} can be uniquely factorized as a product of generators to the integer power:

$$\ell = \ell_1^{i_1} \ell_2^{i_2} \ell_3^{i_3} \ell_4^{i_4}, \quad i_1 \in \mathbb{Z}, i_2 = 0, \dots, n-1, i_3 = 0, 1, i_4 = 0, 1, \quad (1.16)$$

where the first two generators are the ones from the invariant subgroup belonging to $\mathbf{L}^{(1)}$. Using (1.16), any group representation can be given in terms of matrices corresponding to these generators.

1.2.2 Irreducible representations of line groups

The structure of line groups indicate the procedure for construction of their IRs. Namely, first the IRs of the first family line group should be found. Then, IRs for families 2-8 are constructed using the induction procedure [33] from its halving subgroup belonging to $\mathbf{L}^{(1)}$, while the IRs for families 9-13 are constructed using the same procedure, only the halving subgroup is different (see previous paragraph).

IRs of the first family line groups

First family line group $\mathbf{L}^{(1)}$ is a direct product of a screw axis group $\mathbf{T}_Q(f)$ and an axial point group \mathbf{C}_n . This is very suitable since IRs in this case can be constructed as a direct product of IRs denoting each subgroup. On the other hand, since both subgroups are cyclic, we know that all their IRs are one-dimensional. For finite rotational group of the order n generated by C_n , n inequivalent IRs are characterized by integer \tilde{m} from the interval $(-\frac{n}{2}, \frac{n}{2}]$: $D^{(m)}(C_n^s) = e^{i\frac{2\pi\tilde{m}}{n}s}$.

On the other hand, as screw axis group $\mathbf{T}_Q(f)$ is infinite, there are infinitely many IRs. We classify them with the help of the parameter \tilde{k}

$$D^{(\tilde{k})}((C_Q|f)^t) = e^{i\tilde{k}ft}. \quad (1.17)$$

Obviously, for $\tilde{k} \in (-\frac{\pi}{f}, \frac{\pi}{f}]$ a set of inequivalent IRs is obtained.

Finally, we conclude that the first family line group \mathbf{L} has infinitely many IRs which we label as $_{\tilde{k}}A_{\tilde{m}}(L)$ defined as

$$_{\tilde{k}}A_{\tilde{m}}(C_Q|f) = e^{i\tilde{k}f}, \quad _{\tilde{k}}A_{\tilde{m}}(C_n) = e^{i\tilde{m}\frac{2\pi}{n}}. \quad (1.18)$$

QNs \tilde{k} and \tilde{m} classifying IRs can be interpreted as quasi-momentum and z component of an angular quasi-momentum, respectively. As for nontrivial Q , action of the line group elements on a monomer generates a helical arrangement along the z -axis, \tilde{k} and \tilde{m} are called *helical QNs*. Domain of \tilde{k} , i.e $(-\frac{\pi}{f}, \frac{\pi}{f}]$ is called *helical Brillouin zone*.

For commensurate systems ($Q = q/r$, $GCD(q, r) = 1$, with translational period $a = qf$), group can be written as $\mathbf{T}_q^r(a/q) \otimes \mathbf{C}_n$. In this case, we can make different choice of QNs based on the IRs of translational subgroup $\mathbf{T}(a)$

$$D^{(k)}((\mathbf{1}_3|a)) = e^{ika}, \quad k \in (-\frac{\pi}{a}, \frac{\pi}{a}], \quad (1.19)$$

and IRs of the isogonal group \mathbf{C}_q

$$D^{(m)}(C_q) = e^{im\frac{2\pi}{q}}, \quad m \in (-\frac{q}{2}, \frac{q}{2}]. \quad (1.20)$$

Domain $(-\frac{\pi}{a}, \frac{\pi}{a}]$ of the linear momentum k is well-known as Brillouin zone. While \tilde{m} represents only a part of an angular quasi-momentum not present in \tilde{k} , QN m , corresponds to the full angular quasi-momentum. Since \mathbf{C}_q is not a subgroup of \mathbf{L} , when one multiplies these two representations we will not get the representation of \mathbf{L} . It can be shown [34, 35] that resulting representations written in terms of generators $(C_q^r|f)$ and C_n , using QNs k and m , are

$${}_k A_m(C_q^r|f) = e^{ikf + im\frac{2\pi r}{q}}, \quad {}_k A_m(C_n) = e^{im\frac{2\pi}{n}}. \quad (1.21)$$

Other families

After finding the IRs of first family line groups, IRs of other families can be constructed using the inductive procedure explained in Appendix B.

It is convenient to present IRs by matrices representing generators of the group since any group element can be written as a monomial over generators (1.16). Each IR is characterized by a set of QNs which obviously contains the helical (\tilde{k} and \tilde{m}) or linear (k and m) momenta. Beside them, in families $F' = 2, \dots, 8$ parity QNs Π_h , Π_h , Π_U , Π_v , Π_v and Π_v , correspondingly, are present. In families $F'' = 9, \dots, 13$ two additional generators induce three parity QNs. ²

1.2.3 Construction of DLGs

According to Noether isomorphism theorem DLGs follow the classification of line groups. There are thirteen families $\tilde{\mathbf{L}}^{(F)}$ of DLGs, having the relation between them

$$\tilde{\mathbf{L}}^{(1)} \stackrel{2}{<} \tilde{\mathbf{L}}^{(F')} \stackrel{2}{<} \tilde{\mathbf{L}}^{(F'')}, \quad (1.22)$$

where $\tilde{\mathbf{L}}^{(i)}$ is i -th family DLG, with $F' = 2, \dots, 8$ and $F'' = 9, \dots, 13$.

Each DLG is a product of Abelian double groups

$$\tilde{\mathbf{L}} = \prod_{p=1}^K \tilde{\mathbf{L}}_p. \quad (1.23)$$

²Since $\sigma_h \sigma_v = U$, parity Π_U is a product of parities of horizontal and vertical mirror plane symmetry.

Infinite cyclic subgroups $\mathbf{T}_Q(f)$, $\mathbf{T}(a)$, $\mathbf{T}_{2n}^1(\frac{a}{2})$ and $\mathbf{T}'(\frac{a}{2})$ with corresponding generators $(C_Q|f)$, $(\mathbb{1}_3|a)$, $(C_{2n}|\frac{a}{2})$ and $(\sigma_v|\frac{a}{2})$ remain of infinite dimension. Translational double group $\widetilde{\mathbf{T}}(a)$ with generator $(\mathbb{1}_3|a)$ has trivial action in the spin space. On the other hand, double groups $\widetilde{\mathbf{T}}_Q(f)$, $\widetilde{\mathbf{T}}_{2n}^1(\frac{a}{2})$ and $\widetilde{\mathbf{T}}'(\frac{a}{2})$ have generators $(\widetilde{C_Q|f})$, $(\widetilde{C_{2n}|\frac{a}{2}})$ and $(\widetilde{\sigma_v|\frac{a}{2}})$ with nontrivial action in the spin space (due to the existence of nontrivial rotational part in the group generator).

Regarding the generators of axial double point groups, the situation is the following: \widetilde{C}_n and \widetilde{S}_{2n} are of order $2|n|$, while $\widetilde{\sigma}_h$, $\widetilde{\sigma}_v$ and \widetilde{U} are of order 4. Axial double point groups are cyclic in the case of \widetilde{C}_n , \widetilde{C}_{nh} , \widetilde{D}_n , \widetilde{C}_{nv} , \widetilde{D}_{nd} and \widetilde{S}_{2n} (n - odd). If n is even, \widetilde{S}_{2n} can be written in the product form.

To summarize, in the case of cyclic groups $\widetilde{\mathbf{L}}$, we can connect each element ℓ_p of the single cyclic group \mathbf{L}_p with two double group elements $\tilde{\ell}_p$ and $\tilde{\ell}'_p = \tilde{e}'\tilde{\ell}_p$ that belong to the doubled group $\widetilde{\mathbf{L}}_p$. For cyclic double groups $\widetilde{\mathbf{L}}_p$ we can write

$$\widetilde{\mathbf{L}}_p = \{\tilde{e}, \tilde{\ell}_p, \dots, \tilde{\ell}_p^{2|\ell_p|}\}, \tilde{\ell}_p^{|\ell_p|+i} = \tilde{e}'\tilde{\ell}_p^i \quad (0 \leq i < |\ell_p|). \quad (1.24)$$

If this is not the case, $\widetilde{\mathbf{L}}_p$ can be written in the product form

$$\widetilde{\mathbf{L}}_p = \{\tilde{e}, \tilde{\ell}_p, \dots, \tilde{\ell}_p^{|\ell_p|-1}\} \otimes \{\tilde{e}, \tilde{e}'\}. \quad (1.25)$$

In both situations, double group element $\tilde{\ell}$ of the group $\widetilde{\mathbf{L}}$ can be written as a product of generators to the i_p integer power, similarly as in line groups. However, in the second case exponents i_p are not unique. This problem can be overcome by considering \tilde{e}' as an additional generator (although not necessary, the same can be done for cyclic groups), yielding a unique presentation of double group elements

$$\tilde{\ell} = \tilde{\ell}_1^{i_1} \dots \tilde{\ell}_K^{i_K} \tilde{e}'^\varepsilon, \quad 0 \leq i_p < |\ell_p|, \quad \varepsilon = 0, 1. \quad (1.26)$$

Using the (1.26), any group representation can be given in terms of matrices corresponding to these generators. We conclude this subsection with the summary, given in Table 1.2, of obtained results that describe the structure and generators of DLGs.

1.2.4 Construction of IRs

The structure of DLGs (1.22) implies that IRs of DLGs can be constructed by a following procedure: as first step we construct IRs of the first family DLGs, being

Table 1.2: **Double line groups.** For each family $F = 1, \dots, 13$ factorization, generators and their orders are tabulated. In the last column, values of $|\ell_p|$ to be used in (1.26) for generators, as well as the order of \tilde{e}' , are given.

F	Factorization	Generators (1.26)	Orders	$ \ell_p $ with $ \tilde{e}' $
1	$\tilde{T}_Q(f)\tilde{C}_n$	$(\widetilde{C_Q f}), \tilde{C}_n$	$\infty, 2n$	$\infty, n, 2$
2	$\tilde{T}(a)\tilde{S}_{2n}$	$n \text{ odd } (\mathbb{1}_3 a), \tilde{S}_{2n}, \tilde{e}'$ $n \text{ even } (\mathbb{1}_3 a), \tilde{S}_{2n}$	$\infty, 2n, 2$ $\infty, 4n$	$\infty, 2n, 2$
3	$\tilde{T}(a)\tilde{C}_{nh}$	$(\mathbb{1}_3 a), \tilde{C}_n, \tilde{\sigma}_h$	$\infty, 2n, 4$	$\infty, n, 2, 2$
4	$\tilde{T}_{2n}^1(\frac{a}{2})\tilde{C}_{nh}$	$(\widetilde{C_{2n} \frac{a}{2}}), \tilde{C}_n, \tilde{\sigma}_h$	$\infty, 2n, 4$	$\infty, n, 2, 2$
5	$\tilde{T}_Q(f)\tilde{D}_n$	$(\widetilde{C_Q f}), \tilde{C}_n, \tilde{U}$	$\infty, 2n, 4$	$\infty, n, 2, 2$
6	$\tilde{T}(a)\tilde{C}_{nv}$	$(\mathbb{1}_3 a), \tilde{C}_n, \tilde{\sigma}_v$	$\infty, 2n, 4$	$\infty, n, 2, 2$
7	$\tilde{C}_n\tilde{T}'(\frac{a}{2})$	$(\widetilde{\sigma_v \frac{a}{2}}), \tilde{C}_n$	$\infty, 2n$	$\infty, n, 2$
8	$\tilde{C}_{nv}\tilde{T}_{2n}^1(\frac{a}{2})$	$(\widetilde{C_{2n} \frac{a}{2}}), \tilde{C}_n, \tilde{\sigma}_v$	$\infty, 2n, 4$	$\infty, n, 2, 2$
9	$\tilde{T}(a)\tilde{D}_{nd}$	$(\mathbb{1}_3 a), \tilde{C}_n, \tilde{U}_d, \tilde{\sigma}_v$	$\infty, 2n, 4, 4$	$\infty, n, 2, 2, 2$
10	$\tilde{T}'(\frac{a}{2})\tilde{S}_{2n}$	$n \text{ odd } (\widetilde{\sigma_v \frac{a}{2}}), \tilde{S}_{2n}, \tilde{e}'$ $n \text{ even } (\widetilde{\sigma_v \frac{a}{2}}), \tilde{S}_{2n}$	$\infty, 2n, 2$ $\infty, 4n$	$\infty, 2n, 2$
11	$\tilde{T}(a)\tilde{D}_{nh}$	$(\mathbb{1}_3 a), \tilde{C}_n, \tilde{\sigma}_v, \tilde{\sigma}_h$	$\infty, 2n, 4, 4$	$\infty, n, 2, 2, 2$
12	$\tilde{T}'(\frac{a}{2})\tilde{C}_{nh}$	$(\widetilde{\sigma_v \frac{a}{2}}), \tilde{C}_n, \tilde{\sigma}_h$	$\infty, 2n, 4$	$\infty, n, 2, 2$
13	$\tilde{T}_{2n}^1(\frac{a}{2})\tilde{D}_{nh}$	$(\widetilde{C_{2n} \frac{a}{2}}), \tilde{C}_n, \tilde{U}, \tilde{\sigma}_v$	$\infty, 2n, 4, 4$	$\infty, n, 2, 2, 2$

the direct product of cyclic groups, just by multiplying IRs of cyclic subgroups (see Appendix A). IRs of other groups can be found by inductive method [33] (see also Appendix B) from IRs of a halving subgroup: for $\tilde{L}^{(F')}$ this is the first family DLG, while for $\tilde{L}^{(F'')}$ halving subgroups belong to $\tilde{L}^{(F')}$.

IRs of the first family DLG

First family DLG $\tilde{L}^{(1)}$ is a direct product $T_Q(f) \otimes \tilde{C}_n$ of the screw axis $T_Q(f)$ and double axial point group \tilde{C}_n . Due to their product structure, IRs can be directly obtained (see Appendix A).

In helical QNs, IRs represent arbitrary element $(\widetilde{C_Q|f})^t \tilde{C}_n^s$ of the first family DLG as

$$\tilde{k} A_{\tilde{m}}((\widetilde{C_Q|f})^t \tilde{C}_n^s) = e^{i\tilde{k}f} e^{i\frac{2\pi}{n}\tilde{m}}, \quad (1.27)$$

where \tilde{k} takes continuous values from the range $\tilde{k} \in (-\pi/f, \pi/f]$. Allowed values of

\tilde{m} , belonging to the domain $(-n/2, n/2]$ are obtained from the equation

$$\tilde{k}A_{\tilde{m}}(\tilde{C}_n^{2n}) = e^{i\frac{2\pi}{n}\tilde{m}2n} = e^{i4\pi\tilde{m}} = 1, \quad (1.28)$$

yielding integer and half integer \tilde{m} values. It should be noted that sometimes domain $(0, n]$ of allowed values of \tilde{m} is used. However, since equation (1.28) is independent on the choice of domain region, half integer and integer \tilde{m} values remain.

Furthermore, if the system is translationally periodic along z-axis ($Q = q/r$) linear QNs are used. Generators in this case are represented as

$${}_kA_m(\widetilde{(C_q^r|f)}) = e^{ikf+i\frac{2\pi r}{q}m}, {}_kA_m(\tilde{C}_n) = e^{i\frac{2\pi}{n}m}, \quad (1.29)$$

with $k \in (-\pi/a, \pi/a]$ and $m \in (-\pi/q, \pi/q]$. Again, allowed values of m are determined from the equation

$${}_kA_m(\tilde{C}_n^{2n}) = e^{i\frac{2\pi}{n}m2n} = e^{i4\pi m} = 1, \quad (1.30)$$

giving integer and half integer values of m . The results are presented in Table C.1.

IRs of the fifth family DLG

In order to illustrate the induction procedure from the halving subgroup (see Appendix B for theoretical details) used to obtain IRs of the remaining families of DLGs, we give detailed construction of IRs for the fifth family DLG $\tilde{\mathbf{L}}^{(5)} = \tilde{\mathbf{T}}_Q(f)\tilde{\mathbf{D}}_n$. Beside the generators from the index two subgroup $\tilde{\mathbf{L}}^{(1)} = \tilde{\mathbf{T}}_Q(f)\tilde{\mathbf{C}}_n$, these groups have \tilde{U} -axis as an additional generator.

We label the additional element as $\tilde{l} = \tilde{U}$, while elements of $\tilde{\mathbf{L}}^{(1)}$ are $(\widetilde{C_Q|f})^t \tilde{C}_n^s$. \tilde{l} -conjugation of the first family DLG element gives us

$$\tilde{l}^{-1}(\widetilde{C_Q|f})^t \tilde{l} = (\widetilde{C_Q|f})^{-t}, \quad (1.31)$$

$$\tilde{l}^{-1}\tilde{C}_n^s \tilde{l} = \tilde{C}_n^{-s}, \quad (1.32)$$

$$\tilde{l}^{-1}(\widetilde{C_Q|f})^t \tilde{C}_n^s \tilde{l} = (\widetilde{C_Q|f})^{-t} \tilde{C}_n^{-s}. \quad (1.33)$$

For the fixed IR $\tilde{k}A_{\tilde{m}}(\tilde{\mathbf{L}}^{(1)})$ its orbit is singleton if \tilde{l} -conjugation transforms IR into an equivalent set. In helical QNs this leads to the equation

$$\tilde{k}A_{\tilde{m}}(\widetilde{(C_Q|f)}^t \tilde{C}_n^s) = \tilde{k}A_{\tilde{m}}(\widetilde{(C_Q|f)}^{-t} \tilde{C}_n^{-s}), \quad (1.34)$$

which is satisfied for $\tilde{k} = 0, \pi/f$ and $\tilde{m} = 0, n/2$. Induced representation for the element \tilde{l} can be found by solving the equation

$$\tilde{k}A_{\tilde{m}}(\tilde{l}^2) = \tilde{k}A_{\tilde{m}}(\tilde{C}_n^m) = e^{i2\tilde{m}\pi} \rightarrow \tilde{k}A_{\tilde{m}}^{\Pi_U}(\tilde{l}) = \pm e^{i\tilde{m}\pi}, \quad (1.35)$$

introducing new parity QN $\Pi_U = \pm i$ for half integer \tilde{m} and $\Pi_U = \pm 1$ for integer \tilde{m} .

Condition to obtain singleton orbit for representation ${}_kA_m(\tilde{\mathbf{L}}^{(1)})$

$${}_kA_m((\widetilde{C_Q|f})^t \tilde{C}_n^s) = {}_kA_m((\widetilde{C_Q|f})^{-t} \tilde{C}_n^{-s}), \quad (1.36)$$

yields the following four possibilities: $k = 0$ and $m = 0$, $k = 0$ and $m = q/2$, $k = \pi/a$ and $m = -p/2$ or $k = \pi/a$ and $m = (q - p)/2$. Induced representation for the element \tilde{l} is found from equation

$${}_kA_m(\tilde{l}^2) = {}_kA_m(\tilde{C}_n^m) = e^{i2m\pi} \rightarrow {}_kA_m^{\Pi_U}(\tilde{l}) = \pm e^{im\pi}. \quad (1.37)$$

Clearly, in this case additional QN is introduced: parity Π_U being ± 1 for integer and $\pm i$ for half integer m .

For other pairs of QNs: $\tilde{k} = 0, \pi/f$, $\tilde{m} \in (0, n/2)$ and $\tilde{k} \in (0, \pi/f)$, $\tilde{m} \in (-n/2, n/2]$ ($k \in (0, \pi/a)$, $m \in (-q/2, q/2]$; $k = 0$, $m \in (0, q/2)$ and $k = \pi/a$, $m \in (p/2, (q - p)/2)$) induced IRs are of doubled dimensions. Representation of generators in helical QNs are

$$\begin{aligned} \tilde{k}E_{\tilde{m}}((\widetilde{C_Q|f})) &= \begin{pmatrix} \tilde{k}A_{\tilde{m}}((\widetilde{C_Q|f})) & 0 \\ 0 & \tilde{k}A_{\tilde{m}}((\widetilde{C_Q|f})^{-1}) \end{pmatrix} = \begin{pmatrix} e^{i\tilde{k}f} & 0 \\ 0 & e^{-i\tilde{k}f} \end{pmatrix}, \\ \tilde{k}E_{\tilde{m}}(\tilde{C}_n) &= \begin{pmatrix} \tilde{k}A_{\tilde{m}}(\tilde{C}_n) & 0 \\ 0 & \tilde{k}A_{\tilde{m}}(\tilde{C}_n^{-1}) \end{pmatrix} = \begin{pmatrix} e^{i\frac{2\pi}{n}\tilde{m}} & 0 \\ 0 & e^{-i\frac{2\pi}{n}\tilde{m}} \end{pmatrix}, \\ \tilde{k}E_{\tilde{m}}(\tilde{U}) &= \begin{pmatrix} 0 & \tilde{k}A_{\tilde{m}}(\tilde{U}^2) \\ 1 & 0 \end{pmatrix} = \begin{pmatrix} 0 & (-1)^{2\tilde{m}} \\ 1 & 0 \end{pmatrix}, \end{aligned} \quad (1.38)$$

while in linear QNs we get

$$\begin{aligned} {}_kE_m((\widetilde{C_Q|f})) &= \begin{pmatrix} e^{ikf+i\frac{2\pi}{Q}m} & 0 \\ 0 & e^{-ikf-i\frac{2\pi}{Q}m} \end{pmatrix}, \\ {}_kE_m(\tilde{C}_n) &= \begin{pmatrix} e^{i\frac{2\pi}{n}m} & 0 \\ 0 & e^{-i\frac{2\pi}{n}m} \end{pmatrix}, \\ {}_kE_m(\tilde{U}) &= \begin{pmatrix} 0 & (-1)^{2m} \\ 1 & 0 \end{pmatrix}. \end{aligned} \quad (1.39)$$

In the definition of $_{\tilde{k}}E_{\tilde{m}}(\tilde{U})$ (1.38) and $_kE_m(\tilde{U})$ (1.39) we introduce a parity number $\Pi_{\tilde{e}'} = \pm 1$, being 1 for integer and -1 for half integer values of \tilde{m} and m . In Table C.5, IRs of $\tilde{\mathbf{L}}^{(5)}$ are tabulated on generators. The complete set of IRs of all DLGs is given in Appendix C, while the general analysis of the constructed IRs will be given below. The matrices of generator \tilde{e}' are not included in Tables given in Appendix C as it is a priori known that they are equal to $\mathbb{1}_{|\mu|}$ for integer and $-\mathbb{1}_{|\mu|}$ for half integer IRs, where $|\mu|$ is dimension of an IR.

General classification of IRs

As evident from the presented results for DLGs belonging to the first and fifth family, classification of IRs is essentially the same as for line groups [13], with a few important subtleties. For convenience, in what follows we will use \bar{k} and \bar{m} for both helical and linear momenta. Similarly as in single line groups, \bar{k} takes values from the Brillouin zone $(-\bar{k}_{\partial}, \bar{k}_{\partial}]$ ($\tilde{k}_{\partial} = \pi/f$, $k_{\partial} = \pi/a$). All IRs are classified by \bar{k} from the irreducible domain, which is the Brillouin zone for $F = 1, 6, 7, 8$ and $[0, \bar{k}_{\partial}]$ otherwise. The angular momentum \bar{m} can be integer or half integer, belonging to the interval $(-\bar{m}_{\partial}, \bar{m}_{\partial}]$ ($\tilde{m}_{\partial} = n/2$, $m_{\partial} = q/2$). Furthermore, additional generators $\tilde{\ell}_p$ are present for the groups $F > 1$, thus introducing new parity QNs Π_p . In line groups parities takes values $\Pi_p = \pm 1$, while in DLGs parities can take four values $\Pi_p = \pm 1, \pm i$. Finally, for an additional generator \tilde{e}' parity $\Pi_{\tilde{e}'} = \pm 1$ is introduced.

The representations with $\Pi_{\tilde{e}'} = 1$ are also representations of \mathbf{L} , extended to $\tilde{\mathbf{L}}$. Hence, integer IRs of DLGs form a complete set of IRs of line groups, extended to the double group, while half-integer IRs are additional ones present in DLGs only. Thus, Π_p takes only values $\Pi_p = \pm 1$ for the integer IRs (when $(-1)^{2\bar{m}} = 1$) and $\Pi_p = \pm i$ in the half-integer cases (when $(-1)^{2\bar{m}} = -1$). Finally, as in line groups, the general label of an IR of DLG is $\mu = (\bar{k}, \bar{m}, \Pi)$, where Π is the set of parities.

Chapter 2

Spin-orbit interaction

In solid-state physics, the nonrelativistic Schrödinger equation is used for an electron band-structure calculations. Without relativistic corrections, it leads to even-degenerate bands, spin-up and spin-down. Spin-dependent term in the Hamiltonian arise as a relativistic correction, which can cause splitting of the orbital bands. In some cases, this leads to removal of spin degeneracy. Effects of SOC are tightly related with symmetry.

In this Chapter, starting from Dirac equation, we first introduce the well known origin of the SOC term. Also, general remarks concerning the SOC dependent terms in solid state systems are given, followed by some details regarding the perturbative approach and symmetry bans which are commonly used. In last Section, results from Chapter 1 are applied in order to perform full symmetry based analysis of SOC effects in Q1D systems. More details can be found in [27, 36].

2.1 Origin of SOC

To gain the insight into the relativistic correction of the Schrödinger equation, we will start from the Dirac Hamiltonian for spin 1/2 particle in the presence of the external potential $V(\mathbf{r})$

$$H = c\boldsymbol{\alpha} \cdot \mathbf{p} + \beta mc^2 + V(\mathbf{r})\mathbb{1}_4. \quad (2.1)$$

Here m is the electron rest mass, c is the speed of light in vacuum, $\mathbb{1}_4$ is 4×4 identity matrix, while β , α_x , α_y and α_z are 4×4 matrices

$$\beta = \begin{pmatrix} \mathbb{1}_2 & \\ & -\mathbb{1}_2 \end{pmatrix}, \alpha_x = \begin{pmatrix} & \sigma_x \\ \sigma_x & \end{pmatrix}, \alpha_y = \begin{pmatrix} & \sigma_y \\ \sigma_y & \end{pmatrix}, \alpha_z = \begin{pmatrix} & \sigma_z \\ \sigma_z & \end{pmatrix}, \quad (2.2)$$

where $\mathbb{1}_2$ is the identity matrix 2×2 , while σ_i are the Pauli matrices

$$\sigma_x = \begin{pmatrix} 0 & 1 \\ 1 & 0 \end{pmatrix}, \sigma_y = \begin{pmatrix} 0 & -i \\ i & 0 \end{pmatrix}, \sigma_z = \begin{pmatrix} 1 & 0 \\ 0 & -1 \end{pmatrix}. \quad (2.3)$$

Eigenvector ψ of H , i.e. $H\psi = E\psi$, is the four component wave function which can be expressed in terms of spinor functions ψ_1 and ψ_2

$$\psi = \begin{pmatrix} \psi_1 \\ \psi_2 \end{pmatrix}. \quad (2.4)$$

Consequently, $(H - E)\psi = 0$ becomes

$$\begin{pmatrix} (E - V(\mathbf{r}) - mc^2)\mathbb{1}_2 & -c\boldsymbol{\sigma} \cdot \mathbf{p} \\ -c\boldsymbol{\sigma} \cdot \mathbf{p} & (E - V(\mathbf{r}) + mc^2)\mathbb{1}_2 \end{pmatrix} \begin{pmatrix} \psi_1 \\ \psi_2 \end{pmatrix} = \begin{pmatrix} 0 \\ 0 \end{pmatrix}. \quad (2.5)$$

This gives us

$$(E - V(\mathbf{r}) - mc^2)\psi_1 - c\boldsymbol{\sigma} \cdot \mathbf{p}\psi_2 = 0, \quad (2.6)$$

$$-c\boldsymbol{\sigma} \cdot \mathbf{p}\psi_1 + (E - V(\mathbf{r}) + mc^2)\psi_2 = 0. \quad (2.7)$$

From (2.7) we obtain

$$\psi_2 = \frac{c\boldsymbol{\sigma} \cdot \mathbf{p}}{(E - V(\mathbf{r}) + mc^2)}\psi_1, \quad (2.8)$$

and insert it into (2.6)

$$(E - mc^2)\psi_1 = V(\mathbf{r})\psi_1 + c\boldsymbol{\sigma} \cdot \mathbf{p} \frac{c\boldsymbol{\sigma} \cdot \mathbf{p}}{(E - V(\mathbf{r}) + mc^2)}\psi_1. \quad (2.9)$$

Next, we will define new parameter $E' = E - mc^2$ and transform the previous equation to

$$E'\psi_1 = V(\mathbf{r})\psi_1 + \frac{1}{2m}\boldsymbol{\sigma} \cdot \mathbf{p} \left(1 + \frac{E' - V(\mathbf{r})}{2mc^2}\right)^{-1} \boldsymbol{\sigma} \cdot \mathbf{p}\psi_1. \quad (2.10)$$

In the nonrelativistic limit $E' \ll mc^2$, we can keep only the dominant contribution of $\left(1 + \frac{E' - V(\mathbf{r})}{2mc^2}\right)^{-1}$

$$\left(1 + \frac{E' - V(\mathbf{r})}{2mc^2}\right)^{-1} \approx 1 - \frac{E' - V(\mathbf{r})}{2mc^2}. \quad (2.11)$$

Furthermore, by noticing that

$$\begin{aligned} \mathbf{p}V(\mathbf{r}) &= V(\mathbf{r})\mathbf{p} - i\hbar\nabla V(\mathbf{r}), \\ (\boldsymbol{\sigma} \cdot \nabla V(\mathbf{r}))(\boldsymbol{\sigma} \cdot \mathbf{p}) &= (\nabla V(\mathbf{r}) \cdot \boldsymbol{\sigma}) + i\boldsymbol{\sigma} \cdot (\nabla V(\mathbf{r}) \times \mathbf{p}), \\ (\boldsymbol{\sigma} \cdot \mathbf{p})(\boldsymbol{\sigma} \cdot \mathbf{p}) &= p^2, \end{aligned} \quad (2.12)$$

equation (2.10) can be written as

$$E'\psi_1 = \left[V(\mathbf{r}) + \left(1 - \frac{E' - V(\mathbf{r})}{2mc^2} \right) \frac{p^2}{2m} \right] \psi_1 - \frac{\hbar^2}{4m^2c^2} (\nabla V(\mathbf{r})) (\nabla \psi_1) + \frac{\hbar}{4m^2c^2} \boldsymbol{\sigma} \cdot (\nabla V(\mathbf{r}) \times \mathbf{p}) \psi_1. \quad (2.13)$$

Nonrelativistic approximation further implies $E' - V(\mathbf{r}) \approx p^2/2m$ and $(E' - V(\mathbf{r}))p^2 \approx p^4/2m$, obtaining the desired form of the Dirac Hamiltonian

$$E'\psi_1 = \left(\frac{p^2}{2m} - \frac{p^4}{8m^3c^2} + V(\mathbf{r}) - \frac{\hbar^2}{4m^2c^2} (\nabla V(\mathbf{r})) \cdot \nabla + \frac{\hbar}{4m^2c^2} \boldsymbol{\sigma} \cdot (\nabla V(\mathbf{r}) \times \mathbf{p}) \right) \psi_1. \quad (2.14)$$

The first and third term in (2.14) describe the nonrelativistic Schrödinger equation, the second term is the classical relativistic correction, while the fourth term is a spin independent relativistic correction that does not have a classical analog, called the Darwin term. The last term is the SOC Hamiltonian H_{so} , describing the coupling of spin and orbital degrees of freedom. In what follows, to the nonrelativistic Hamiltonian, we will add only the H_{so} term,

$$H_{\text{so}} = \frac{\hbar}{4m^2c^2} (\nabla V(\mathbf{r}) \times \mathbf{p}) \cdot \boldsymbol{\sigma}. \quad (2.15)$$

In solids, being the subject of this dissertation, crystal potential $V_c(\mathbf{r})$ of the surrounding ions creates external potential which couples to spin due to SOC. This coupling mechanism is called Dresselhaus [4] SOC. Since $\nabla V_c(\mathbf{r})$ and \mathbf{p} are polar vectors, the cross product $\nabla V_c(\mathbf{r}) \times \mathbf{p}$ transforms as an axial vector. We may label this product as \mathbf{L}_D , since it has the same transformation properties as angular momentum $\boldsymbol{\ell}$. Thus, Dresselhaus SOC term can be written as

$$H_D = \frac{\hbar}{4m^2c^2} \mathbf{L}_D \cdot \boldsymbol{\sigma}, \quad (2.16)$$

resembling the atomic $\boldsymbol{\ell} \cdot \boldsymbol{\sigma}$ coupling.

Actually, it turns out than in most cases atomic approximation of Dresselhaus SOC interaction is a good approximation, since SOC contribution is relevant only close to the atomic cores. In other words, we will use atomic SOC Hamiltonian

$$\lambda_{\text{so}} \boldsymbol{\ell} \cdot \mathbf{s}, \quad (2.17)$$

where $\mathbf{s} = 1/2\boldsymbol{\sigma}$ is electron's spin operator. Note that both operators are defined assuming $\hbar = 1$, thus parameter λ_{so} is given in energy units.

In an isolated atom, it is well known that λ_{so} increases rapidly with the atomic number Z . In the theory of atomic spectra [37], perturbative correction of energy due to SOC reads [38]

$$E_{nl} = E_{nl}^0 + \frac{1}{2}\lambda_{nl}[j(j+1) - l(l+1) - \frac{3}{4}], \quad (2.18)$$

where n , l and j are principal, angular and total angular QNs, respectively, while the atomic SOC parameter is equal to

$$\lambda_{nl} = \frac{(\frac{1}{137})^2 Z^4}{n^3 l(l + \frac{1}{2})(l + 1)} R_y. \quad (2.19)$$

For carbon atom, $n = 2$, $l = 1$ and $Z = 4$ (effective nuclear charge seen by p -electrons). In this case we obtain SOC constant close to 12 meV, in accordance with the common value of λ_{so} found in a literature [39]. However, it is to be noted that other λ_{so} values are also used [40, 41].

The Z^4 scaling of λ_{nl} in (2.19) does not take into account that outer electrons are the only relevant electrons for SOC, whose QNs n and l change with Z . If we do not want to worry about them, SOC strength should be scaled like Z^2 [18].

Finally, we note that if other sources of potential are present, different SOC interaction Hamiltonians arise. For example, if an uniform electric field \mathbf{E} is present, equation (2.15) is equal to the *Rashba* [9] SOC term

$$H_R = \frac{\hbar|e|}{4m^2c^2}(\mathbf{E} \times \mathbf{p}) \cdot \boldsymbol{\sigma}, \quad (2.20)$$

as the external potential $V(\mathbf{r})$ satisfies

$$V(\mathbf{r}) = - \underbrace{q}_{=-|e|} \mathbf{E} \cdot \mathbf{r} = |e|\mathbf{E} \cdot \mathbf{r}. \quad (2.21)$$

In this dissertation, we focus on the Dresselhaus SOC solely.

2.2 Perturbative approach

In solid-state physics, it is a first task to analyze Schrödinger equation for the electrons in lattice-periodic potential. Bloch's theorem gives the solutions of this differential equation in the form

$$\psi_{n,\mathbf{k}}(\mathbf{r}) = e^{i\mathbf{k} \cdot \mathbf{r}} u_{n,\mathbf{k}}(\mathbf{r}), \quad (2.22)$$

where \mathbf{k} is the wavevector, n is the band index, and $u_{n,\mathbf{k}}(\mathbf{r})$ is a function with the same periodicity as the crystal lattice. For Hamiltonian H

$$H = \frac{p^2}{2m} + V(\mathbf{r}) + \frac{\hbar}{4m^2c^2}(\nabla V(\mathbf{r}) \times \mathbf{p}) \cdot \boldsymbol{\sigma}, \quad (2.23)$$

eigenequation $H\psi_{n,\mathbf{k}}(\mathbf{r}) = E_{n,\mathbf{k}}\psi_{n,\mathbf{k}}(\mathbf{r})$ can be rewritten in terms of invariant functions $u_{n,\mathbf{k}}(\mathbf{r})$

$$H_{\mathbf{k}}u_{n,\mathbf{k}}(\mathbf{r}) = E_{n,\mathbf{k}}u_{n,\mathbf{k}}(\mathbf{r}), \quad (2.24)$$

where $H_{\mathbf{k}}$ is equal to

$$H_{\mathbf{k}} = \frac{\mathbf{p}^2}{2m} + \frac{\hbar^2\mathbf{k}^2}{2m} + \frac{\hbar}{m}\mathbf{k} \cdot \mathbf{p} + V(\mathbf{r}) + \frac{\hbar}{4m^2c^2}(\nabla V \times (\mathbf{p} + \hbar\mathbf{k})) \cdot \boldsymbol{\sigma}. \quad (2.25)$$

Commonly, analysis of SOC effects on electron bands in the vicinity of band gap is based on $\mathbf{k} \cdot \mathbf{p}$ [42] perturbation theory [43–50]. Within this approach, the "unperturbed Hamiltonian"

$$H_0 = \frac{\mathbf{p}^2}{2m} + V(\mathbf{r}), \quad (2.26)$$

equals the exact Hamiltonian without SOC, while

$$H' = \frac{\hbar^2\mathbf{k}^2}{2m} + \frac{\hbar}{m}\mathbf{k} \cdot \mathbf{p} + \frac{\hbar}{4m^2c^2}(\nabla V \times (\mathbf{p} + \hbar\mathbf{k})) \cdot \boldsymbol{\sigma} \quad (2.27)$$

is treated as a perturbation. Finally, if one is interested in a point in Brillouin zone other than $\mathbf{k} = 0$, i.e. \mathbf{k}_0 , instead of (2.22) one can use different set of functions [51]

$$\psi_{n,\mathbf{k}}(\mathbf{r}) = e^{i\mathbf{k} \cdot \mathbf{r}}(e^{i\mathbf{k}_0 \cdot \mathbf{r}}u_{n,\mathbf{k}}(\mathbf{r})) = e^{i\mathbf{k} \cdot \mathbf{r}}\chi_{n,\mathbf{k}}(\mathbf{r}), \quad (2.28)$$

and write the effective eigenequation (2.24) in terms of $\chi_{n,\mathbf{k}}(\mathbf{r})$ instead of $u_{n,\mathbf{k}}(\mathbf{r})$.

Within the perturbative approach, some general results regarding the spin degeneracy of the bands can be given just by analyzing whether the system of interest possesses both the time reversal and/or spatial inversion symmetry.

Time reversal symmetry operator θ is an antiunitary operator, represented as a product $\theta = UK$ of an unitary operator U and complex conjugation K . For electrons with spin 1/2, θ is equal to

$$\theta = e^{-i\pi\sigma_y/2}K, \quad (2.29)$$

where σ_y is the y component of the vector operator made of Pauli matrices. It is well known that momentum \mathbf{p} and position operator \mathbf{x} are odd under time reversal,

while angular momentum \mathbf{L} and spin $\boldsymbol{\sigma}$ are even. Thus, nonrelativistic Hamiltonian (2.26) describing the motion of an electron in a crystal is invariant under time reversal symmetry. The same holds for Dresselhaus SOC H_D , since a scalar product of two operators even under θ (\mathbf{L}_D and $\boldsymbol{\sigma}$) is invariant.

Thus, in an isolated solid at any point \mathbf{k} in the Brillouin zone energy of the electron with spin \mathbf{s} is equal to the energy of the electron with opposite spin but at $-\mathbf{k}$. Therefore:

$$E_{\mathbf{k}}(\mathbf{s}) = E_{-\mathbf{k}}(-\mathbf{s}). \quad (2.30)$$

If, in addition, the crystal has inversion symmetry, one gets

$$E_{\mathbf{k}}(\mathbf{s}) = E_{-\mathbf{k}}(\mathbf{s}). \quad (2.31)$$

From (2.30) and (2.31) it becomes clear that if both inversion and time reversal symmetry are present, the bands are spin degenerate

$$E_{\mathbf{k}}(\mathbf{s}) = E_{\mathbf{k}}(-\mathbf{s}), \quad (2.32)$$

while in the absence of spatial inversion spin degeneracy is lifted.

Spatial inversion can be broken by applying the electric field, since $\mathbf{r} \rightarrow -\mathbf{r}$ alters the H_R term. In other words, Rashba SOC offers a simple toll to break the spin degeneracy and to induce tunable spin splitting of the bands, directly dependent on the electric field strength.

Magnetic field offers a possibility to induce spin splitting at the cost of breaking the time reversal symmetry. This happens due to the Zeeman coupling $\mathbf{B} \cdot \boldsymbol{\sigma}$ of magnetic field and spin, which anticommutes with θ . However, since magnetic field is hard to control at the nanoscale, electrical production of spin polarization is more convenient.

2.3 Symmetry and SOC in Q1D crystals

The derived IRs of DLGs are to be used in the analysis of electron dynamics in Q1D systems when the spin degree of freedom is included. In this case, state space is composed of orbital and spin factors, $\mathcal{S} = \mathcal{S}_o \otimes \mathcal{C}^2$. Dynamics is governed by Hamiltonian

$$H = H_o \otimes \mathbb{1}_2 + H_{so}, \quad (2.33)$$

where H_o is the spin independent Hamiltonian, while H_{so} is the SOC term.

Hamiltonian (2.33) can be diagonalized with the help of DLG IRs and eigenstates (which are labeled by QNs) can be found, thus providing the possibility to obtain selection rules necessary for the efficient calculation of transition probabilities. Helical QNs are the most suitable to study spin dependent properties of systems described by the first or the fifth family DLGs, or for finite length nanotubes [52], while in all other cases linear QNs are usually applied. In the first step, we will perform the group theory based analysis in order to determine whether SOC induces splitting of the bands or not.

SOC and orbital bands splitting

Let \mathbf{L} be the geometrical symmetry group, which in \mathcal{S}_o acts by the representation $D_o(\mathbf{L})$. Representation $D_o(\mathbf{L})$ commutes with H_o , i.e. $[D_o(\mathbf{L}), H_o] = 0$. In the total space \mathcal{S} acts the double group $\tilde{\mathbf{L}}$ by the representation $D(\tilde{\mathbf{L}}) = D_o(\tilde{\mathbf{L}}) \otimes u(\tilde{\mathbf{L}})$.

The eigenproblem of H_o is solved by taking the full advantage of the system's symmetry. As the result, the eigenvalues and eigenvectors (forming symmetry adapted basis (SAB)) are assigned by QNs of corresponding IRs. Namely, for each IR $D^{(\mu)}(\mathbf{L})$ appearing in decomposition

$$D_o(\mathbf{L}) = \sum_{\mu} f_{D_o}^{(\mu)}(\mathbf{L}) D^{(\mu)}(\mathbf{L}), \quad (2.34)$$

there are $f_{D_o}^{(\mu)}(\mathbf{L})$ bands $\mathcal{E}_{\bar{m}\Pi}^b(\bar{k})$ (counted by the superscript b) of the Hamiltonian H_o . Thus, to each energy assigned by QNs $\mu = (\bar{k}, \bar{m}, \Pi)$ corresponds a multiplet of the degenerate eigenvectors $\{|\mu, j; b\rangle, j = 1, \dots, |\mu|\}$ (where $|\mu|$ is the dimension of the IR), i.e for every j

$$H_o |\mu, j; b\rangle = \mathcal{E}_{\bar{m}\Pi}^b(\bar{k}) |\mu, j; b\rangle, \quad (2.35)$$

while for every symmetry element $l \in \mathbf{L}$

$$D_o(l) |\mu, j; b\rangle = \sum_{j'=1}^{|\mu|} D^{(\mu)}(l) |\mu, j'; b\rangle. \quad (2.36)$$

In the total state space \mathcal{S} , the orbital Hamiltonian, trivially extended to $H_o \otimes \mathbb{1}_2$, commutes with

$$D(\tilde{\mathbf{L}}) = D_o(\tilde{\mathbf{L}}) \otimes u(\tilde{\mathbf{L}}) = \sum_{\mu} f_{D_o}^{(\mu)}(\mathbf{L}) \left(D^{(\mu)}(\tilde{\mathbf{L}}) \otimes u(\tilde{\mathbf{L}}) \right). \quad (2.37)$$

Furthermore, $D^{(\mu)}(\tilde{\mathbf{L}}) \otimes u(\tilde{\mathbf{L}})$ is either an IR, or can be decomposed in two IRs of $\tilde{\mathbf{L}}$ of the same dimension

$$D^{(\mu)}(\tilde{\mathbf{L}}) \otimes u(\tilde{\mathbf{L}}) = D^{(\mu')}(\tilde{\mathbf{L}}), \quad (2.38)$$

$$D^{(\mu)}(\tilde{\mathbf{L}}) \otimes u(\tilde{\mathbf{L}}) = D^{(\mu^+)}(\tilde{\mathbf{L}}) \oplus D^{(\mu^-)}(\tilde{\mathbf{L}}). \quad (2.39)$$

In the (2.38) case, dimension of an IR labeled by μ' is doubled: $|\mu'| = 2|\mu|$. In the (2.39) case, $|\mu^\pm| = |\mu|$. New QNs μ^\pm are $(k, m \pm 1/2, \Pi)$ in linear QNs and $(\tilde{k} \pm \pi/(Qf), \tilde{m} \pm 1/2, \Pi)$ in helical QNs¹. In some trivial cases, QNs can be equal: $\mu^+ = \mu^-$. Degeneracy arising from the doubled dimension in (2.38) is removable only at the cost of symmetry breaking. It is thus clear that SOC may lift only the second type of degeneracy (2.39), giving rise to band splitting into two branches labeled by μ^+ and μ^- .

Spin splitting

Provided that the presence of SOC has induced a band splitting (case (2.39) occurs), spin degeneracy of the branches remains to be investigated. First, we note that electron spin polarization [53] in Q1D systems having nontrivial ($n > 1$) rotational symmetry is possible only along the z-axis. This conclusion naturally arises when possible values of the means in the eigenstate $|\psi\rangle$ of the operators $\mathbf{1}_o \otimes \sigma_i$ are analyzed

$$\langle \sigma_i \rangle_{|\psi\rangle} = \langle \psi | \mathbf{1}_o \otimes \sigma_i | \psi \rangle. \quad (2.40)$$

Consider a band $\mathcal{E}_{\bar{m}\Pi}^b(\bar{k})$ of H assigned by the IR μ of \tilde{L} (\bar{m} is half integer). At any fixed value of \bar{k} eigenstate $|\bar{k}, \bar{m}\rangle$ (possible parity labels are omitted as the analysis is independent of them) can be expressed as the sum of two terms which are the tensor product of vectors $|\bar{k} \pm \bar{k}_u, \bar{m} \pm \frac{1}{2}\rangle \in \mathcal{S}_o$ and the spin states $|\downarrow\rangle$ and $|\uparrow\rangle$:

$$|\bar{k}, \bar{m}\rangle = |\bar{k} - \bar{k}_u, \bar{m} - \frac{1}{2}\rangle |\uparrow\rangle + |\bar{k} + \bar{k}_u, \bar{m} + \frac{1}{2}\rangle |\downarrow\rangle. \quad (2.41)$$

Having in mind that eigenvectors of the Hamiltonian H_0 are orthogonal, and that nonzero matrix elements of Pauli matrices are

$$\begin{aligned} \langle \uparrow | \sigma_x | \downarrow \rangle &= 1, \langle \downarrow | \sigma_x | \uparrow \rangle = 1, \\ \langle \uparrow | \sigma_y | \downarrow \rangle &= -i, \langle \downarrow | \sigma_y | \uparrow \rangle = i, \\ \langle \uparrow | \sigma_z | \uparrow \rangle &= 1, \langle \downarrow | \sigma_z | \downarrow \rangle = -1, \end{aligned} \quad (2.42)$$

¹In order to simplify the notation, when convenient, we use joint notation $|\bar{k}\bar{m}\rangle$ for both linear and helical QNs. In this notation, $\mu^\pm = (\bar{k} \pm \bar{k}_u, \bar{m} \pm 1/2, \Pi)$, where $\bar{k}_u = 0$ in linear QNs and $\bar{k}_u = \pi/(Qf)$ in helical QNs.

it is simple to show

$$\begin{aligned}
\langle \sigma_z \rangle_{|\bar{k}, \bar{m}\rangle} &= \langle \bar{k} - \bar{k}_u, \bar{m} - \frac{1}{2} | \bar{k} - \bar{k}_u, \bar{m} - \frac{1}{2} \rangle - \langle \bar{k} + \bar{k}_u, \bar{m} + \frac{1}{2} | \bar{k} + \bar{k}_u, \bar{m} + \frac{1}{2} \rangle, \\
\langle \sigma_x \rangle_{|\bar{k}, \bar{m}\rangle} &= 0, \\
\langle \sigma_y \rangle_{|\bar{k}, \bar{m}\rangle} &= 0,
\end{aligned} \tag{2.43}$$

thus proving the previously stated assumption.

Next, we analyze mean value of $\mathbb{1}_o \otimes \sigma_z$ in the eigenstates $|\psi\rangle = D(\tilde{\ell}_p) |\bar{k}, \bar{m}\rangle$ obtained by the action of generators $\tilde{\ell}_p$ of the DLG on $|\bar{k}, \bar{m}\rangle$. The resulting $|\psi\rangle$ states are eigenstates that correspond to the same energy as $|\bar{k}, \bar{m}\rangle$. It is easy to see that action of $D(\tilde{\ell}_p)$ induces either a change of sign of QNs i.e $|\bar{k}, -\bar{m}\rangle, |-\bar{k}, \bar{m}\rangle$ and $|-\bar{k}, -\bar{m}\rangle$ are obtained, or QNs are preserved and only the phase of $|\bar{k}, \bar{m}\rangle$ is possibly changed

$$\begin{aligned}
D(\tilde{C}_n) |\bar{k}, \bar{m}\rangle &= e^{i\frac{2\pi}{n}\bar{m}} |\bar{k}, \bar{m}\rangle, \\
D(\tilde{S}_{2n}) |\bar{k}, \bar{m}\rangle &= |-\bar{k}, \bar{m}\rangle = e^{i(\frac{\pi}{n}+\pi)\bar{m}} (|-\bar{k} - \bar{k}_u, \bar{m} - \frac{1}{2}\rangle |\uparrow\rangle + |-\bar{k} + \bar{k}_u, \bar{m} + \frac{1}{2}\rangle |\downarrow\rangle), \\
D(\tilde{\sigma}_h) |\bar{k}, \bar{m}\rangle &= |-\bar{k}, \bar{m}\rangle = i(|-\bar{k} - \bar{k}_u, \bar{m} - \frac{1}{2}\rangle |\uparrow\rangle - |-\bar{k} + \bar{k}_u, \bar{m} + \frac{1}{2}\rangle |\downarrow\rangle), \\
D(\tilde{\sigma}_v) |\bar{k}, \bar{m}\rangle &= |\bar{k}, -\bar{m}\rangle = -|\bar{k} - \bar{k}_u, -\bar{m} - \frac{1}{2}\rangle |\uparrow\rangle + |\bar{k} + \bar{k}_u, -\bar{m} + \frac{1}{2}\rangle |\downarrow\rangle, \\
\widetilde{D((\sigma_v|\frac{a}{2}))} |\bar{k}, \bar{m}\rangle &= |\bar{k}, -\bar{m}\rangle = -|\bar{k} - \bar{k}_u, -\bar{m} - \frac{1}{2}\rangle |\uparrow\rangle + |\bar{k} + \bar{k}_u, -\bar{m} + \frac{1}{2}\rangle |\downarrow\rangle, \\
D(\tilde{U}) |\bar{k}, \bar{m}\rangle &= |-\bar{k}, -\bar{m}\rangle = i(|-\bar{k} + \bar{k}_u, -\bar{m} - \frac{1}{2}\rangle |\uparrow\rangle + |-\bar{k} - \bar{k}_u, -\bar{m} + \frac{1}{2}\rangle |\downarrow\rangle).
\end{aligned} \tag{2.44}$$

After calculating $\langle \sigma_z \rangle_{|\psi\rangle}$, it turns out that mean value $\langle \sigma_z \rangle_{|\psi\rangle}$ can differ from $\langle \sigma_z \rangle_{|\bar{k}, \bar{m}\rangle}$ in sign only. Results are listed in Table 2.1.

It is evident that if vertical mirror or glide plane is a geometrical symmetry of the system, there are two eigenstates $|\bar{k}, \bar{m}\rangle$ and $|\bar{k}, -\bar{m}\rangle$ having the opposite mean value of spin. Therefore, in such systems band splitting does not lift the spin degeneracy. These are the only pure geometrical obstacles to achieve spin dependent band structure.

If, in addition, the total Hamiltonian H commutes with time reversal θ , conditions for spin splitting of the bands are even more rigid. The time reversal has the same effect on $|\bar{k}, \bar{m}\rangle$ (up to phase i) and $\mathbb{1}_o \otimes \sigma_z$ as \tilde{U} . Consequently, joint effect of θ and horizontal mirror plane or \tilde{S}_{2n} maps $|\bar{k}, \bar{m}\rangle$ onto $|\bar{k}, -\bar{m}\rangle$ with identical

Table 2.1: DLG generators $\tilde{\ell}_p$ are in the first column, with parameters defining them in the second. In the third column mean values $\langle \sigma_z \rangle_{|\psi\rangle}$ are expressed through $\langle \sigma_z \rangle_{|\bar{k}, \bar{m}\rangle}$.

$\tilde{\ell}_p$	$(j, \varphi, \mathbf{n}, t)$	$\langle \sigma_z \rangle_{ \psi\rangle}$
\tilde{C}_n	$(0, 2\pi/n, \mathbf{e}_z, 0)$	$\langle \sigma_z \rangle_{ \bar{k}, \bar{m}\rangle}$
\tilde{S}_{2n}	$(1, \pi + \pi/n, \mathbf{e}_z, 0)$	$\langle \sigma_z \rangle_{ \bar{k}, \bar{m}\rangle}$
$\tilde{\sigma}_h$	$(1, \pi, \mathbf{e}_z, 0)$	$\langle \sigma_z \rangle_{ \bar{k}, \bar{m}\rangle}$
$\tilde{\sigma}_v$	$(1, \pi, \mathbf{e}_y, 0)$	$-\langle \sigma_z \rangle_{ \bar{k}, \bar{m}\rangle}$
$\widetilde{(\sigma_v \frac{a}{2})}$	$(1, \pi, \mathbf{e}_y, a/2)$	$-\langle \sigma_z \rangle_{ \bar{k}, \bar{m}\rangle}$
\tilde{U}	$(0, \pi, \mathbf{e}_x, 0)$	$-\langle \sigma_z \rangle_{ \bar{k}, \bar{m}\rangle}$

mean value of spin. Therefore, if the system possesses time reversal symmetry, SOC induced band splitting in the case (2.39) removes the spin degeneracy, i.e spin splitting occurs only in systems whose symmetry group belongs to the first or the fifth family only. Without the time reversal symmetry, purely geometrical constraints allow nonzero polarization in Q1D systems within the families $F = 2, 3$ and 4 also.

Spin splitting can be induced by breaking some of the system symmetries. First, homogeneous collinear magnetic field can break time reversal, vertical mirror/glide planes and U -axes, thus leaving symmetries of the families 1-4 that allow spin splitting. On the other hand, collinear electric field cannot break time reversal, vertical mirror and glide planes, and reduces the symmetry to families 1,6,7,8, where only the first family DLG allows spin splitting. In other words, if collinear electric field is applied in systems having symmetry group from families 1-5, spin splitting can be induced. Lastly, non-collinear electric field conserves U -axis and mirror/glide plane, while breaking rotational symmetry.

SOC effects on band structure

Finally, we address the SOC effects on bands topology in the entire Brillouin zone using both linear and helical QNs, whose common application gives us interesting insight into band splitting. Take, for example, the band $\mathcal{E}_{\bar{m}, \Pi}(\bar{k})$ of H_o and the corresponding bands $\mathcal{E}_{\bar{m}^\pm, \tilde{\Pi}}(\bar{k})$ of $H_o \otimes \mathbb{1}_2$. For linear QNs these bands are exactly

the same

$$\mathcal{E}_{m,\Pi}(k) = \mathcal{E}_{m \pm \frac{1}{2}, \tilde{\Pi}}(k). \quad (2.45)$$

On the other hand, when using helical QNs, there is an additional shift of \tilde{k} for $\pm \tilde{k}_u$, such that $\mathcal{E}_{\tilde{m},\Pi}(\tilde{k})$ splits into two branches $\mathcal{E}_{\tilde{m} \pm \frac{1}{2}, \tilde{\Pi}}(\tilde{k})$ which correspond to two shifted original orbital bands along \tilde{k} in opposite directions, i.e.

$$\mathcal{E}_{\tilde{m} \pm \frac{1}{2}, \tilde{\Pi}}(\tilde{k} \mp \tilde{k}_u) = \mathcal{E}_{\tilde{m},\Pi}(\tilde{k}). \quad (2.46)$$

Clearly, we see that in helical QNs band splitting is observable even without SOC, due to opposite shift of the same energies along the Brillouin zone. If parts of the shifted bands are pushed out of the irreducible domain, they can be seen on the other band, complicating the tracing of band splitting.

Additional complexity when relating bands of H_o and $H_o \otimes \mathbb{1}_2$ appears if crossing of the band $\mathcal{E}_{\bar{m}}(\bar{k})$ with the bands assigned by $\bar{m}' = \bar{m} \pm 1$ is present, regardless of the type of QNs. In this situation bands with the same QNs (in DLG picture) cross at some point \bar{k}_\times of the Brillouin zone. Then, the non-crossing rule [18] must be applied, such that two new bands arise: one new band joins the parts of the initial bands above the crossing level, and the parts below form the other band. Finally, the presence of SOC induces an energy gap at \bar{k}_\times .

In systems whose symmetry belongs to the first or fifth family DLGs, spin polarization of the splitted branches is allowed. In the first family DLG case, each (one-dimensional) band $\mathcal{E}_{\bar{m}}(\bar{k})$ of total Hamiltonian H , with an eigenstate $|\bar{k}\bar{m}\rangle$, has fixed sign of the polarization, except in the cases where there are crossing points with other bands having identical QNs. If the band crossing occurs, the non-crossing rule rearranges the two bands, with a change of polarization sign at \bar{k}_\times , i.e. the rearranged bands are not overall polarized. In the fifth family DLG case, U -axis symmetry is present, yielding a double degenerate bands of H for any particular value of $\bar{k} \in (0, \pi_\partial)$ with eigenstates $|\bar{k}\bar{m}\rangle$ and $|\bar{k}, -\bar{m}\rangle$ oppositely polarized ($\pm\sigma$ along the z-axis).

As an illustration of the non-crossing rule and spin polarization of the bands, in Fig. 2.1 we analyze conduction bands of (15, 5) chiral SWCNT in both helical and linear QNs. In the H_o case, orbital bands whose angular quantum numbers differ by 1 cross (blue and green curves in Fig. 2.1). When the Hamiltonian $H_o \otimes \mathbb{1}_2$ is analyzed, DLG usage activates non-crossing rule, yielding rearrangements of the

bands and change of spin polarization. Finally, in the case of Hamiltonian H , SOC induces spin splitting of the bands.

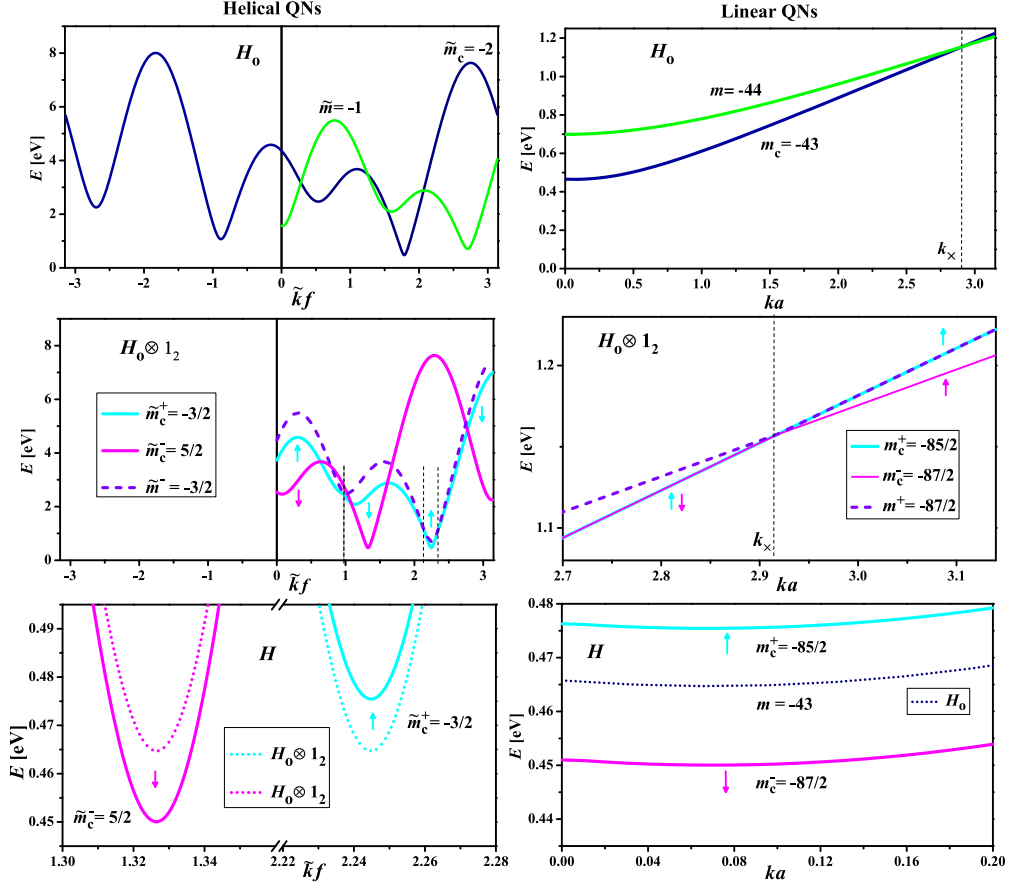


Figure 2.1: Conducting band $\mathcal{E}_{\bar{m}_c}(\bar{k})$ (blue) of SWCNT (15, 5) for Hamiltonian H_0 , branched into $\mathcal{E}_{\bar{m}_c^\pm}(\bar{k})$ (cyan and magenta) for $H_0 \otimes 1_2$ and H for helical and linear QNs (left and right column). Crossing with another orbital band $\mathcal{E}_{\bar{m}}(k)$ (green) at k_\times , such that one of its branches with $m-1/2$ and $\tilde{m}+1/2$ (dashed purple) equals \bar{m}_c^+ or \bar{m}_c^- , activating non-crossing rule: spin polarization along the rearranged bands (arrows) varies due to sign switches at crossing points (vertical dashed lines). Full Brillouin zone is plotted for $\mathcal{E}_{\bar{m}_c}(\tilde{k})$ to comprehend the shift of $\mathcal{E}_{\bar{m}_c^\pm}(\tilde{k})$ for $\pm\tilde{k}_u$. In the last row, bands of unperturbed Hamiltonian (dotted) are supplied to illustrate the effects of SOC on spin splitting. Figure is taken from [27].

Chapter 3

Spin-orbit interaction in SWCNTs

Carbon nanotubes (CNTs) are cylindrical molecules made from rolled-up sheets of graphene. CNTs can be single walled or multi walled (MWCNT), made from more than one concentric SWCNT. In the pioneer work of Iijima [54], MWCNTs were created using an arc-discharge evaporation method. Due to small diameters (4–30nm) of MWCNTs produced, as compared to their length (1 μ m), these systems can be considered Q1D.

Experimental observation of MWCNTs and two years later discovery of SWCNTs of even smaller diameters (1 nm) [55] was followed by theoretical works in which electronic structure of SWCNTs was studied using the tight-binding [56–58] and local-density-functional approach [59]. It was shown that SWCNTs electronic properties are strongly dependent on the way in which graphene sheet is rolled-up into a nanotube, varying from a conductor to the 1 eV band gap semiconductor [28, 60]. Tunability of electron properties through small change of chirality has made them the best candidates for replacing the silicon materials in modern electronics.

Furthermore, measurements of intrinsic thermal vibrations of SWCNTs in the transmission electron microscope [61] have suggested excellent mechanical properties and potential usage of nanotubes as lightweight nanoscale fibres. Also, thermal properties were studied [62] by measuring the specific heat and thermal conductivity, suggesting that 1D quantisation of the phonon band structure greatly enhances thermal properties of the structure.

As mentioned above, structure of SWCNTs can be defined using the graphene rolling along the particular direction: for defined graphene lattice basis vectors \mathbf{a}_1

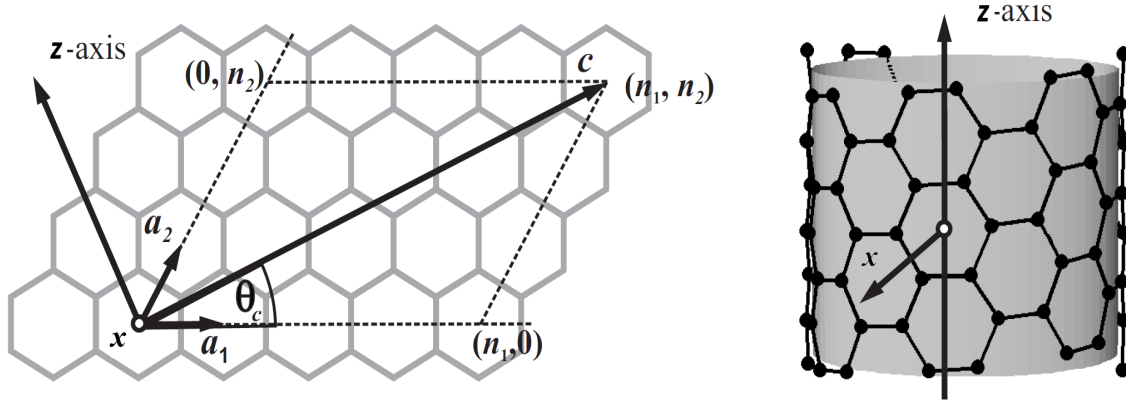


Figure 3.1: Graphene: vectors \mathbf{a}_1 and \mathbf{a}_2 build an elementary cell of a graphene honeycomb, where $|\mathbf{a}_1| = |\mathbf{a}_2| = a_0 = 2,461\text{\AA}$ and the angle between them is 60° . Chiral vector $\mathbf{c} = (n_1, n_2)$ (θ_c is a chiral angle) defines a rolled-up configuration of SWCNT (n_1, n_2) : tube is obtained by cutting the graphene in such a way that \mathbf{c} becomes the circumference of the tube.

and \mathbf{a}_2 and integer numbers n_1 and n_2 , chiral vector

$$\mathbf{c} = n_1\mathbf{a}_1 + n_2\mathbf{a}_2 \quad (3.1)$$

will become circumference of the tube (see Fig. 3.1). By convention, nanotube axis corresponds with the z-axis, while x-axis passes through the center of carbon hexagons. The angle θ_c between the vectors \mathbf{a}_1 and \mathbf{c} is called a chiral angle. SWCNTs are commonly labeled as (n_1, n_2) . Due to symmetries of the graphene plane, it is enough to consider only nonnegative n_1 and n_2 values to obtain all possible configurations. Depending on the choice of n_1 and n_2 , all SWCNTs can be gathered into three different classes

- chiral (\mathcal{C}) for $n_1 \neq n_2 > 0$,
- armchair (\mathcal{A}) for $n_1 = n_2 = n$, i.e. (n, n) ,
- zig-zag (\mathcal{Z}) for $n_1 = n, n_2 = 0$, i.e. $(n, 0)$.

Values $\theta_c = 0^\circ, 30^\circ$ correspond to \mathcal{Z} $((n, 0))$ and \mathcal{A} $((n, n))$ tubes, respectively. Due to the mirror plane symmetry of their configurations, both types are achiral, while for each chiral tube (n_1, n_2) its optical isomer is (n_2, n_1) . In most situations

(e.g. study of electronic and mechanical properties), it suffice to consider only chiral tubes with θ_c within the range $(0, 30^\circ)$ (i.e. tubes with $n_1 > n_2 > 0$).

Finally, SWCNTs can be classified according to their conductance properties [56–59]. They are conducting if the value $p \doteq n_1 - n_2 \pmod{3}$ is equal 0; on the other hand, if $p = \pm 1$ we obtain semiconducting ones. In other words, all armchair tubes are conducting, while among chiral and zig-zag tubes all three above mentioned classes are present.

3.1 Full geometrical symmetry of SWCNTs

In order to define the geometrical symmetry of SWCNT, we start from the single layer of graphite, i.e. graphene [63], whose symmetry group is the symmorphic diperiodic group DG80 [12], with the isogonal point group \mathbf{D}_{6h} and hexagonal lattice with periods $a_0 = 0.246\text{nm}$ (rhombic with an angle $\alpha = 60^\circ$ between them).

Diameter D of the tube (n_1, n_2) is equal to

$$D = \frac{a_0}{\pi} \sqrt{n_1^2 + n_2^2 + n_1 n_2}, \quad (3.2)$$

while the chiral vector θ_c is

$$\sin \theta_c = \frac{\sqrt{3} n_2 a_0}{2|\mathbf{c}|}. \quad (3.3)$$

Geometrical symmetries of chiral and achiral SWCNTs [64]

$$\mathbf{L}_C = \mathbf{T}_q^r(f) \mathbf{D}_n, \quad \mathbf{L}_{Z,A} = \mathbf{T}_{2n}^1\left(\frac{a}{2}\right) \mathbf{D}_{nh}, \quad (3.4)$$

belong to the fifth and thirteenth family line groups. For chiral (n_1, n_2) tubes group parameters (order of principal rotational axis n ; parameters q, r and fractional translation f defining the screw axis $(C_q^r|f)$) are defined as

$$\begin{aligned} n &= \text{GCD}(n_1, n_2), \quad q = 2 \frac{n_1 n_2 + n_1^2 + n_2^2}{n \mathcal{R}}, \\ r &= \frac{q}{n} \text{Fr} \left[\frac{n}{q \mathcal{R}} \left(3 - 2 \frac{n_1 - n_2}{n_1} \right) + \frac{n}{n_1} \left(\frac{n_1 - n_2}{n} \right)^{\text{Eu}(\frac{n_1}{n}) - 1} \right], \\ f &= \frac{a_0 n}{\sqrt{n_1^2 + n_2^2 + n_1 n_2}}, \quad a = \frac{a_0 \sqrt{3} \sqrt{n_1^2 + n_2^2 + n_1 n_2}}{n \mathcal{R}}. \end{aligned} \quad (3.5)$$

In (3.5), \mathcal{R} is 3 if $(n_1 - n_2)/3n$ is an integer number or 1 if it is not. $\text{Eu}(x)$ is an Euler function giving the number of the coprimes with x being less than or equal to

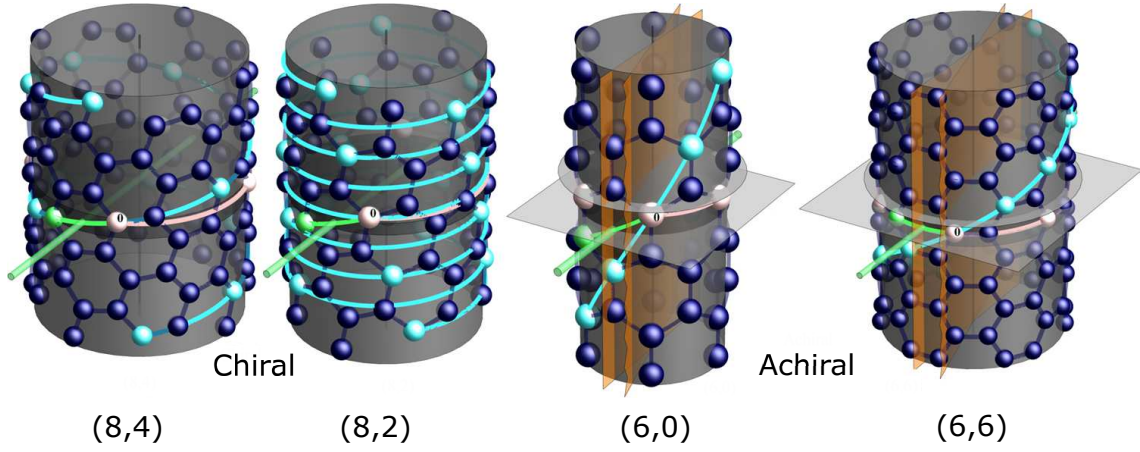


Figure 3.2: In the left panel, chiral (8,2) and (8,4) tubes are given, while in the right panel, achiral zig-zag (6,0) and armchair (6,6) tubes are presented. U -axis is along x -axis, while parallelograms are vertical and horizontal mirror planes. Figure is taken from [13].

x , while $\text{Fr}(x) = x - [x]$ is the fractional part of the rational number x . For both zig-zag $(n, 0)$ and armchair (n, n) tubes group parameters are n , $q = 2n$, $r = 1$, $f = a/2$, while $a = \sqrt{3}a_0$ in the zig-zag and $a = a_0$ in the armchair case. An illustration of chiral (8,2) and (8,4) tubes, as well as achiral (6,0) and (6,6) tubes is given in Fig. 3.2.

Arbitrary element of tube's symmetry group \mathbf{L}_C and $\mathbf{L}_{A/Z}$ can be expressed in the following way

$$\ell_{tsu} = (C_q^r|f)^t C_n^s U^u, \quad (3.6)$$

$$\ell_{tsuv} = (C_{2n}^1|\frac{a}{2})^t C_n^s U^u \sigma_v^v, \quad (3.7)$$

respectively. Here $(C_q^r|f)^t$ with $t = 0, \pm 1, \dots$ is an element of the screw axis subgroup $\mathbf{T}_q^r(f)$; elements of the rotation group \mathbf{C}_n around the z -axis are C_n^s with $s = 0, \dots, n-1$; U is the rotation around the x -axis for an angle π (thus $u = 0, 1$). For achiral tubes additional generator σ_v is the vertical xz mirror plane ($v = 0, 1$).

Each SWCNT is a single orbit system, i.e. the whole tube can be constructed by the action of tube's symmetry group on a single carbon atom. In the chiral cases stabilizer of any atom is trivial (the identity element only) and the whole nanotube represents generic orbit of the fifth family line groups. In the case of achiral tubes stabilizer has two elements: $\{e, C_n \sigma_x\}$ for zig-zag and $\{e, \sigma_h\}$ for armchair tubes. Therefore, in order to reconstruct the whole tube for the achiral case, it is enough

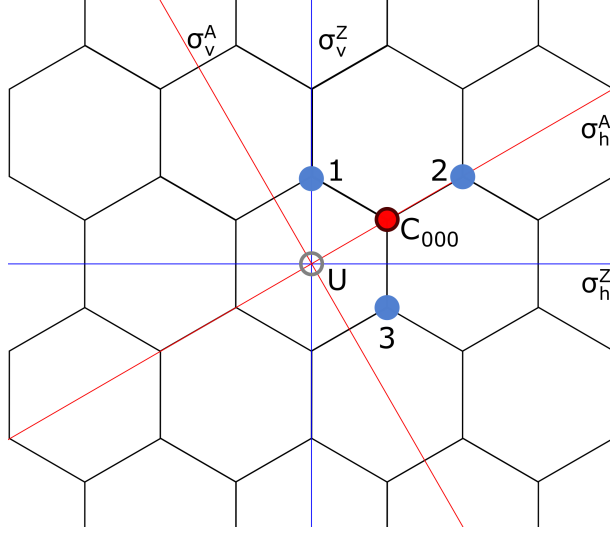


Figure 3.3: Symcell atom C_{000} and its nearest neighbors 1,2 and 3 at honeycomb are represented. C_2 -axis perpendicular to the plane becomes U -axis of the nanotube, i.e. x-axis on Fig. 3.1. In case of zig-zag and armchair tube the graphene mirror planes, marked by blue and red lines respectively, survives the rolling becoming σ_h and σ_v symmetries of the tube.

to use the elements from the fifth family subgroup: $\ell_{tsu0} \in \mathbf{T}_{2n}^1(a/2)\mathbf{D}_n$. These elements are usually called transversal elements ¹.

As the symcell atom we choose the atom C_{000} of graphene honeycomb (Fig. 3.3). After rolling, its cylindrical coordinates are

$$\mathbf{r}_{000} = \left(\frac{D}{2}, \varphi_{000}, z_{000}\right), \quad \varphi_{000} = 2\pi \frac{n_1 + n_2}{nqR}, \quad z_{000} = \frac{n_1 - n_2}{\sqrt{6qn}R}a_0. \quad (3.8)$$

Acting by the transversal element ℓ_{tsu} on \mathbf{r}_{000} we get coordinates of any other atom

$$\mathbf{r}_{tsu} = \ell_{tsu}\mathbf{r}_{000} = \left(\frac{D}{2}, (-1)^u\varphi_{000} + 2\pi\left(\frac{rt}{q} + \frac{s}{n}\right), (-1)^uz_{000} + t\frac{n}{q}a\right). \quad (3.9)$$

3.1.1 Symmetry-adapted relaxation procedure

The described rolled-up configuration of SWCNTs is not necessarily the equilibrium one, as one expects that for small diameter tubes the curvature causes additional

¹Let $\mathbf{H} = \{h_1 = e, h_2, \dots\}$ be a subgroup of the group \mathbf{G} . Set $a\mathbf{H} = \{a, ah_2, \dots\}$, $a \in \mathbf{G}$, is called left coset of subgroup \mathbf{H} determined by its representative a . By analogy, set $\mathbf{H}a$ is called right coset. Transversal of a subgroup \mathbf{H} in \mathbf{G} is a subset of \mathbf{G} which contains exactly one element in every coset of \mathbf{H} [32].

tension with respect to the layer. In order to "relax" the induced tension and find the stable configuration, symmetry preserving optimization of the structure needs to be performed [65].

Since, according to the topological theorem of Abud and Sartori [66], the extremes of the invariant functions should be searched on the manifolds with maximal symmetry, we need to examine which SWCNT parameters can be modified without changing the symmetry of a system. SWCNT structure can be fully determined by six parameters: three coordinates of the initial atom r_{000} , φ_{000} , z_{000} and three group parameters: $Q = q/r$, f and n . Parameter n is discrete and its change would lead to symmetry breaking. All other parameters are continuous and their modification preserves the system's symmetry. This leads us to the conclusion that five parameters $(Q, f, r_{000}, \varphi_{000}, z_{000})$ are allowed to be varied in the chiral case, while in the achiral tubes four parameter $(f, r_{000}, \varphi_{000}, z_{000})$ can be changed (recall that $Q = 2n$ for achiral tubes).

Change of φ_{000} and z_{000} solely can be seen as relative shift of two sublattices [31], while changes of parameters Q , f and r_{000} leads to homogeneous deformation of the cylinder

- change of the parameter Q to Q' leads to the tube's torsion

$$\frac{2\pi}{Q'} = \frac{2\pi}{Q} + \tau f, \quad (3.10)$$

where τ represents torsion per unit length f .

- change of the parameter f to f' is equivalent to the axial strain ϵ_z

$$f' = f(1 + \epsilon_z). \quad (3.11)$$

- by changing the parameter r_{000} we introduce radial breathing which changes the diameter of the tube

$$D' = D(1 + \epsilon_c), \quad (3.12)$$

where ϵ_c is the circumferential strain.

If we wish to investigate the impact of some deformations, then its corresponding parameter should be fixed to the desired value, while the remaining parameters can be determined by finding the stable configuration with the above mentioned relaxation procedure. More details can be found in [30, 31, 65, 67].

3.2 SOC induced effects in SWCNTs

Before we analyze the influence of SOC in SWCNTs using the previously derived DLGs (Chapter 1), a brief overview of the previously reported theoretical and experimental results is given.

An overview

In graphene, the presence of inversion symmetry forbids spin splitting of the bands. Although spin splitting is forbidden, theoretical and numerical studies predict SOC induced band gap of around $24\mu\text{eV}$ [68–70], requiring very low temperatures ($\approx 0.2\text{K}$) to experimentally probe the predicted results.

The influence of SOC on the effective mass Hamiltonian of SWCNTs [43] was the first paper analyzing the effects in the vicinity of high symmetry points of graphene (\mathbf{K} , \mathbf{K}') based on the zone folding and $\mathbf{k} \cdot \mathbf{p}$ theory. After that, using the empirical tight-binding Hamiltonian, Chico et al. [20] had shown that spin splitting is possible in chiral SWCNTs, whereas in achiral ones the same is not allowed. Later theoretical study [71] confirmed the presence of spin splitting and gap opening in nanotubes. SOC effects were then probed in an experimental setup [23], where single electron was confined in a quantum dot and magnetic field parallel to the tube axis was applied. The results suggested that electron-hole asymmetry is present, by showing that SOC induced spin splitting is not the same in conductance and valence bands. More concretely, the measured value of spin-splitting in the maximum of the highest valence band was $(0.37 \pm 0.02) \text{ meV}$, while in the lowest conductance band minima the corresponding splitting was found to be $(0.21 \pm 0.02) \text{ meV}$. After that, in a series of theoretical papers [21, 22, 72–74] a description of the SOC effects on electronic structure was given, using tight-binding, non-orthogonal tight-binding and first-principles calculation. Here we recapitulate these conclusions, mainly focusing on the

Table 3.1: Parameters in equation (3.14), given in nm units.

	$a_{-,1}^{(p)}$	$a_{-,2}^{(p)}$	$a_{+,1}^{(p)}$	$a_{+,2}^{(p)}$
Metallic ($p = 0$)	-0.095	-0.090	0.096	-0.090
Type-I ($p = 1$)	-0.087	-0.085	0.105	-0.094
Type-II ($p = -1$)	0.087	-0.086	-0.105	-0.093

ones presented in [22] (consistent with other theoretical conclusions). In armchair SWCNTs, SOC induced energy gap dependence on diameter D is the following

$$E_{gap}^a = a^{(a)} \frac{\lambda_{so}}{D}, \quad (3.13)$$

where $a^{(a)} = 0.098\text{nm}$. Furthermore, band (spin) splitting of top valence and bottom conductance bands of zig-zag (chiral) nanotubes is dependent on the diameter D and the chiral angle θ_c in a following way:

$$E_{b,split}^{(p)} = \lambda_{so} \frac{a_{b,1}^{(p)} + a_{b,2}^{(p)} \cos 3\theta_c}{D}, \quad (3.14)$$

Here, integer p distinguishes metallic ($p = 0$) from type-I ($p = 1$) or type-II ($p = -1$) semiconducting nanotubes, while $b = \pm$ refers to the conductance and valence band, respectively. Parameters $a_{b,1}^{(p)}$ and $a_{b,2}^{(p)}$ are given in Table 3.1.

Table 3.2: Conductance band splitting of metallic nanotubes $p = 0$ with diameter close to 3nm.

(n_1, n_2)	d [nm]	Spin splitting [meV]	(n_1, n_2)	d [nm]	Spin splitting [meV]
(38, 2)	3.06	0.03	(31, 13)	3.07	0.15
(37, 4)	3.07	0.04	(30, 12)	2.93	0.15
(37, 1)	2.94	0.03	(29, 14)	2.97	0.18
(36, 6)	3.08	0.05	(28, 16)	3.02	0.22
(36, 3)	2.94	0.03	(27, 18)	3.07	0.26
(35, 5)	2.96	0.05	(26, 17)	2.94	0.26
(34, 7)	2.97	0.07	(25, 19)	3.00	0.30
(33, 9)	3.00	0.09	(24, 21)	3.05	0.34
(32, 11)	3.03	0.12	(23, 20)	2.92	0.35

Theoretical results were put on the test after another experimental work [24] in which spin splitting in metallic SWCNTs ($p = 0$) was measured. More concretely, 3.4 meV spin splitting value in conductance band minimum of tubes with diameter 3nm is observed. In order to compare theoretical predictions with the measured value, it is appealing to use equation (3.14). In Table 3.2 we present the values of spin splittings for minimum of the lowest conducting band of SWCNT with diameter $(3 \pm 0.1)\text{nm}$. The biggest value of spin splitting is 0.35meV, being one order of magnitude smaller than the experimentally observed value.

Also, quite recent density-functional based study [75] of spin splitting in nearly metallic chiral SWCNTs wasn't able to explain discrepancy between theoretical and

experimental results. Moreover, for tube (10,7) they reported a larger magnitude of spin splitting of conductance band compared to valence band. This is opposite to the previously reported results [22].

3.2.1 Symmetry based analysis of SOC effects

Derived DLGs and their IRs allow direct diagonalization of the Hamiltonian using the POLSym code [29]. The diagonalization procedure in the POLSym code is based on the modified group projector technique [25], enabling us to calculate only interaction between \mathbf{r}_{000} and its neighbors, within the range of interaction. Spin independent Hamiltonian is calculated through the matrix elements of H_0 in the sp3 basis [76] using the full range of interaction potentials. As mentioned in Chapter 2, we will use on-site approximation of the SOC, $H_{\text{so}} = \lambda_{\text{so}} \mathbf{l} \cdot \mathbf{s}$, where spin-orbit constant λ_{so} is taken to be 12 meV [39], though some other values [40, 41] can be found in the literature.

As shown in Section 2.3, vertical mirror symmetry bans spin splitting in achiral tubes. Bands of these tubes are assigned by IRs of dimension two or four (one-dimensional IRs correspond to special points $k = 0, \pi$). Orbital band of H_0 corresponding to the four-dimensional representation ${}_k G_{m_o}(\mathbf{L}_{\mathcal{Z},\mathcal{A}})$ with $m_o = 1, 2, \dots, n-1$ will be splitted due to SOC, as

$${}_k G_{m_o}(\tilde{\mathbf{L}}_{\mathcal{Z},\mathcal{A}}) \otimes u(\tilde{\mathbf{L}}_{\mathcal{Z},\mathcal{A}}) = {}_k G_{m_o - \frac{1}{2}}(\tilde{\mathbf{L}}_{\mathcal{Z},\mathcal{A}}) \oplus {}_k G_{m_o + \frac{1}{2}}(\tilde{\mathbf{L}}_{\mathcal{Z},\mathcal{A}}). \quad (3.15)$$

On the other hand, if the orbital bands are labeled by the two-dimensional representations ${}_k E_0^{A/B}(\mathbf{L}_{\mathcal{Z},\mathcal{A}})$ and ${}_k E_{n/2}^{A/B}(\mathbf{L}_{\mathcal{Z},\mathcal{A}})$, band splitting is not allowed

$$\begin{aligned} {}_k E_0^{A/B}(\tilde{\mathbf{L}}_{\mathcal{Z},\mathcal{A}}) \otimes u(\tilde{\mathbf{L}}_{\mathcal{Z},\mathcal{A}}) &= {}_k G_{\frac{1}{2}}(\tilde{\mathbf{L}}_{\mathcal{Z},\mathcal{A}}), \\ {}_k E_n^{A/B}(\tilde{\mathbf{L}}_{\mathcal{Z},\mathcal{A}}) \otimes u(\tilde{\mathbf{L}}_{\mathcal{Z},\mathcal{A}}) &= {}_k G_{n - \frac{1}{2}}(\tilde{\mathbf{L}}_{\mathcal{Z},\mathcal{A}}). \end{aligned} \quad (3.16)$$

Equation (3.16) fully explains the behaviour of armchair SWCNT band above and below the Fermi level, and the emergence of band gap in armchair tubes. Initially, when solving eigenproblem of the orbital Hamiltonian H_o , two-dimensional bands, one assigned by ${}_k E_n^A(\mathbf{L}_{\mathcal{A}})$ and the other by ${}_k E_n^B(\mathbf{L}_{\mathcal{A}})$ [77] cross at the Fermi level (Fig. 3.4 (left panel)). When the spin degree is taken into account, but without including SOC term to the Hamiltonian, dynamics of the system is described by the Hamiltonian $H_o \otimes \mathbb{1}_2$. In this case, DLGs should be used instead of single groups.

Consequently the bands do not change but, according to equation (3.16), instead of IRs ${}_kE_n^A(\tilde{\mathbf{L}}_{\mathcal{A}})$ and ${}_kE_n^B(\tilde{\mathbf{L}}_{\mathcal{A}})$ each of them is now assigned by four-dimensional representation ${}_kG_{n-\frac{1}{2}}(\tilde{\mathbf{L}}_{\mathcal{A}})$. Noncrossing rule [18] forbids crossing of bands with identical QNs, meaning that these two orbital bands have to be rearranged into two new bands that touch at the Fermi level (Fig. 3.4 (right panel)). In the end, full Hamiltonian $H_0 \otimes \mathbb{1}_2 + H_{\text{so}}$ leads to the opening of a band gap (Fig. 3.4, inset in the right panel).

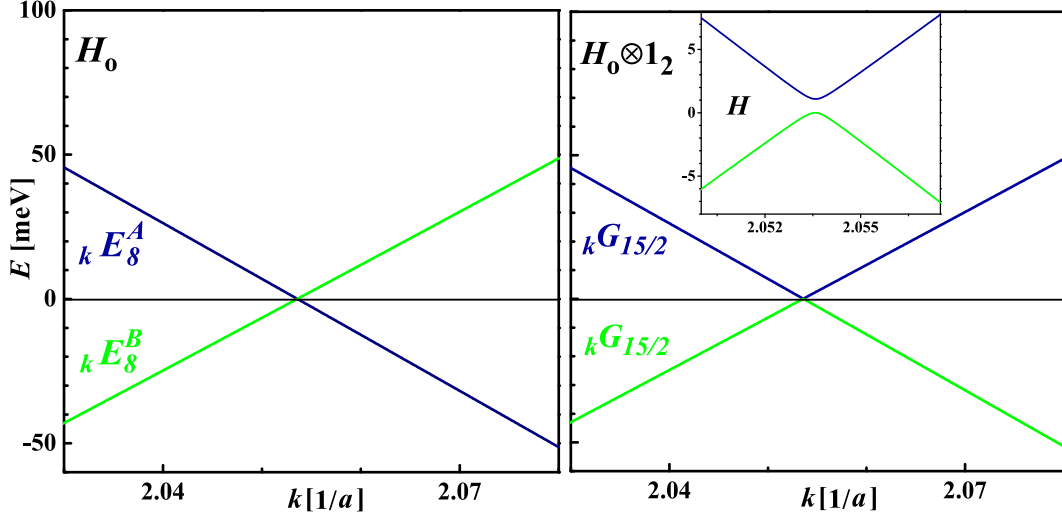


Figure 3.4: Band splitting in armchair SWCNT: (left panel) Two bands of H_0 for tube (8,8), assigned by two-dimensional line group IRs ${}_kE_8^A$ and ${}_kE_8^B$ cross at the Fermi level; (right panel) bands of $H_0 \otimes \mathbb{1}_2$, labeled in terms of DLG IR ${}_kG_{\frac{15}{2}}(\tilde{\mathbf{L}}_{\mathcal{A}})$, touch at the Fermi level. Inset: presence of SOC induces a band gap. Figure is taken from [36].

In the case of zig-zag SWCNTs, lowest conductance and highest valence band split when SOC is included. This happens due to the fact that both orbital bands are assigned by four-dimensional representation ${}_kG_{m_0}(\mathbf{L}_{\mathcal{Z}})$ and due to equation (3.15) band splitting occurs, illustrated in Fig. 3.5.

Finally, in chiral SWCNTs all orbital bands transform according to one-dimensional IRs ${}_kA_m(\mathbf{L}_{\mathcal{C}})$ in linear QNs or ${}_{\tilde{k}}A_{\tilde{m}}(\mathbf{L}_{\mathcal{C}})$ in helical QNs. SOC induces splitting of all bands

$$\begin{aligned} {}_kA_m(\tilde{\mathbf{L}}_{\mathcal{C}}) \otimes u(\tilde{\mathbf{L}}_{\mathcal{C}}) &= {}_kA_{m+\frac{1}{2}}(\tilde{\mathbf{L}}_{\mathcal{C}}) \oplus {}_kA_{m-\frac{1}{2}}(\tilde{\mathbf{L}}_{\mathcal{C}}), \\ {}_{\tilde{k}}A_{\tilde{m}}(\tilde{\mathbf{L}}_{\mathcal{C}}) \otimes u(\tilde{\mathbf{L}}_{\mathcal{C}}) &= {}_{\tilde{k}+\frac{\pi}{Qf}}A_{\tilde{m}+\frac{1}{2}}(\tilde{\mathbf{L}}_{\mathcal{C}}) \oplus {}_{\tilde{k}-\frac{\pi}{Qf}}A_{\tilde{m}-\frac{1}{2}}(\tilde{\mathbf{L}}_{\mathcal{C}}), \end{aligned} \quad (3.17)$$

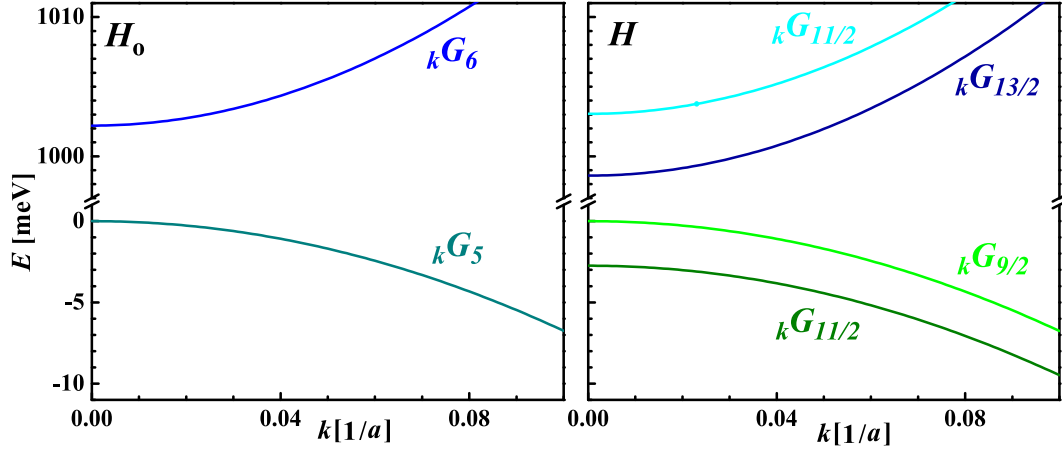


Figure 3.5: Lowest conductance and highest valence band of zig-zag SWCNT (8, 0). (left panel) Two bands of H_0 are assigned by four-dimensional representations ${}_kG_5(\mathbf{L}_Z)$ and ${}_kG_6(\mathbf{L}_Z)$. (right panel) When SOC is included, both bands split into bands of H . Their degeneracy remains the same, but the two branches are assigned by IRs with different angular momentums 11/2 and 13/2 for the bottom conductance bands, as well as 9/2 and 11/2 for the top valence bands. Figure is taken from [36].

which is followed by the removal of spin degeneracy. In other words, each split branch has opposite spin polarization for fixed k -point. In most cases, sign of spin polarization along the band is fixed. However, as thoroughly explained in Section 2.3, in some situations sign of the spin polarization of the band can vary, owing to the non-crossing rule of two bands with identical QNs (having opposite polarization). The rearrangement of the bands is such that, after the crossing point, the abrupt switch of spin polarization occurs. We identify such situations whenever two orbital bands with angular momentum differing by ± 1 intersect; then two of their branches with identical angular momentum, cross as well.

In Fig. 3.6 we illustrate this situation on the example of tube (9, 3). In the top panel, conductance band and few relevant orbital bands of the orbital Hamiltonian H_0 are plotted in helical QNs. Their angular QNs are $\tilde{m}_0^c = -1$, $\tilde{m}_0 = 0$ and $\tilde{m}_0 = 1$. When the Hamiltonian $H_0 \otimes \mathbb{1}_2$ is considered, their branches are assigned by one of the following values of angular QNs: $\tilde{m} = \pm 1/2, \pm 3/2$. The middle graph in Fig. 3.6, show helical branches of the orbital bands with angular QNs $\tilde{m} = -1/2$ and $\tilde{m} = 3/2$, in order to illustrate cases when bands with identical

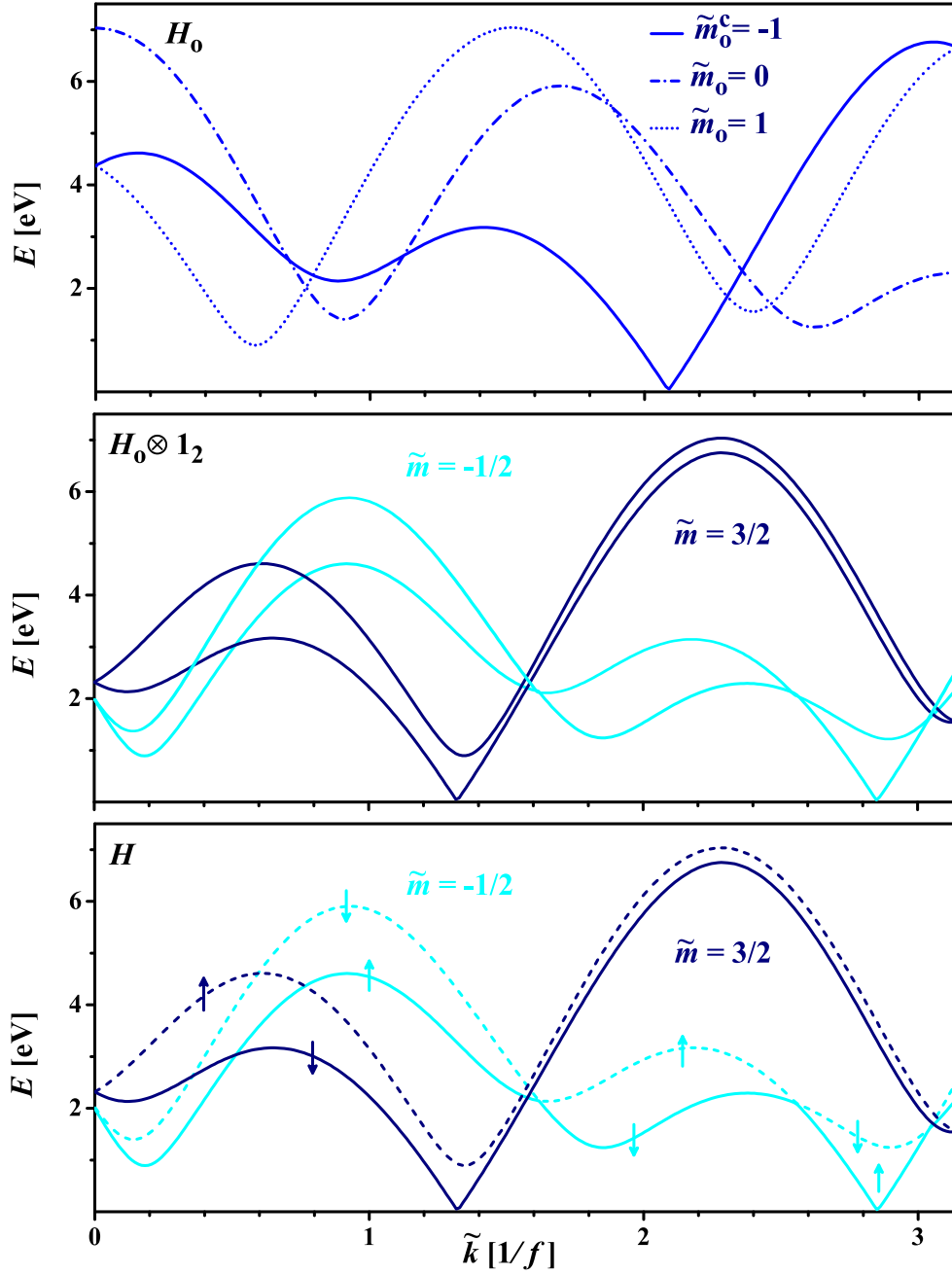


Figure 3.6: Conductance bands of SWCNT (9, 3): (top panel) conductance bands of the orbital Hamiltonian H_o with angular QNs $\tilde{m}_o = 0$, $\tilde{m}_o = 1$ and $\tilde{m}_o^c = -1$; (middle panel) branches with angular QNs $\tilde{m} = -1/2$ and $\tilde{m} = 3/2$ in the case of Hamiltonian $H_o \otimes 1_2$; (bottom panel) rearranged bands as the result of the non-crossing rule, after the application of SOC. Arrows indicate the change of polarization along them. Figure is taken from [36].

QNs have/don't have an intersection (this is situation before the non crossing rule is applied). First, we will focus on branches with $\tilde{m} = -1/2$ which intersect. Bottom graph in Fig. 3.6 shows the rearranged bands with angular QN $\tilde{m} = -1/2$ as a result of the non-crossing rule, leading to the change of polarization along them. Also, at the intersection points, adding the SOC term to the Hamiltonian opens a gap. On the other hand, bands with $\tilde{m} = 3/2$ have a constant sign of polarization, as expected.

It is to be mentioned that the above analysis is valid for optical isomers, i.e. their band structure is equivalent. The only difference between two isomers is in the value of spin polarization of the corresponding bands, having opposite values in the same point of Brillouin zone.

3.2.2 Effects of strain on the magnitude of SOC induced splitting

When examining diameter and chiral angle dependance of the magnitude of band and spin splitting, we also found the same behaviour as Izumida et al. [22]. On the other hand, our method of calculation enabled us to reveal one subtlety, which can lead us towards understanding the discrepancy between theory and experiment, as well as opposite numerical results reported for the ratio of valence and conductance band splitting in chiral tubes.

Namely, we have shown that the ratio is highly dependent on the relaxation (i.e. small variations of tubes configuration). This is illustrated in Fig. 3.7, where SOC induced splitting is presented for the rolled-up fully relaxed configuration of the tube (9, 3). The bands are plotted in helical QNs since the natural torsion [30, 31, 65, 67] is taken into account; this also makes easier to present the results of the spin splitting as in helical QNs the two branches are shifted in opposite directions along \tilde{k} for \tilde{k}_u . Results for the rolled-up configuration show smaller valence spin splitting compared to the conductance band. However, the relaxation procedure switches the relative ratio of these splittings.

Dependence of spin splitting on tube's configuration in metallic SWCNTs motivated us to investigate the influence of strain. Moreover, in experiments, SWCNTs configurations can be influenced by the small axial strain ε_z . As an illustration, in Fig. 3.8 spin splitting for $\varepsilon_z = 2\%$ stretched and $\varepsilon_z = -2\%$ compressed tube (9, 3) is presented. The plot show that stretching induces different magnitude of spin split-

ting in valence and conductance bands, whereas compressing has small effect on spin splitting. To conclude, this result offers possible explanation of an experimental results, i.e. slight change of tube's configuration due to imposed strain by contact formation can induce observable effect on measurement. Presented symmetry based analysis of SOC in SWCNTs has been published in Milivojević et al [36].

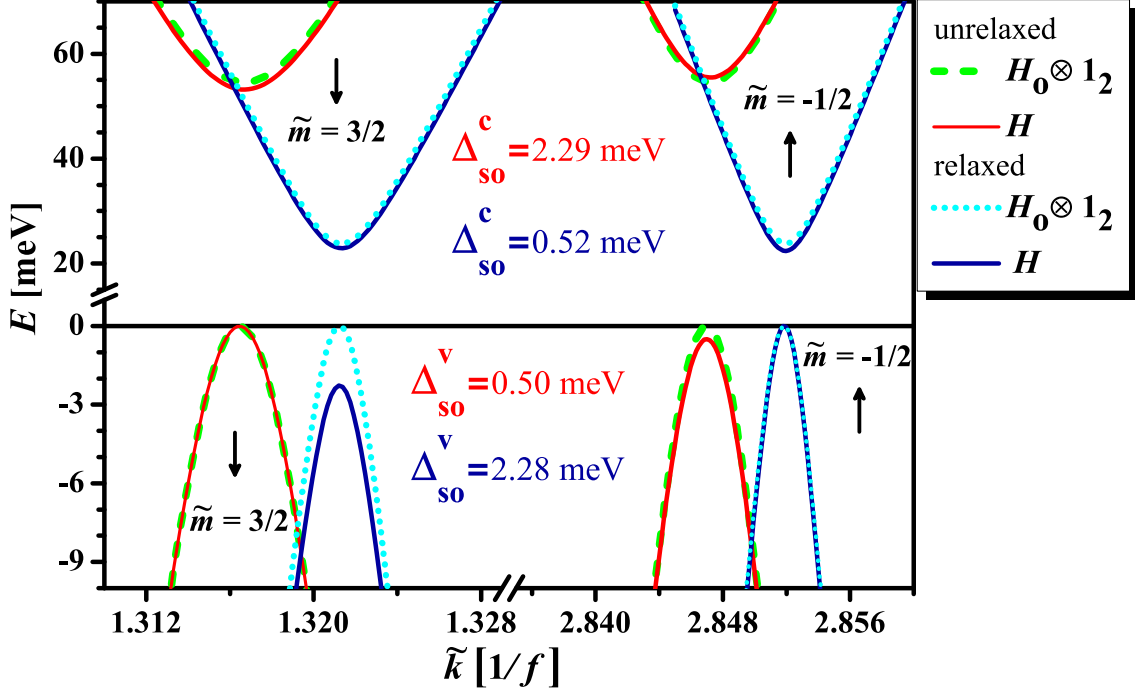


Figure 3.7: Lowest conductance and highest valence bands of tube (9, 3), expressed in helical QNs. Dynamics is governed by the Hamiltonians $H_0 \otimes \mathbb{1}_2$ and H , arrows indicate electron spin polarization, while $\Delta_{so} = |E_{\uparrow} - E_{\downarrow}|$ denotes the absolute value of the spin splitting of valence and conductance bands. Figure is taken from [36].

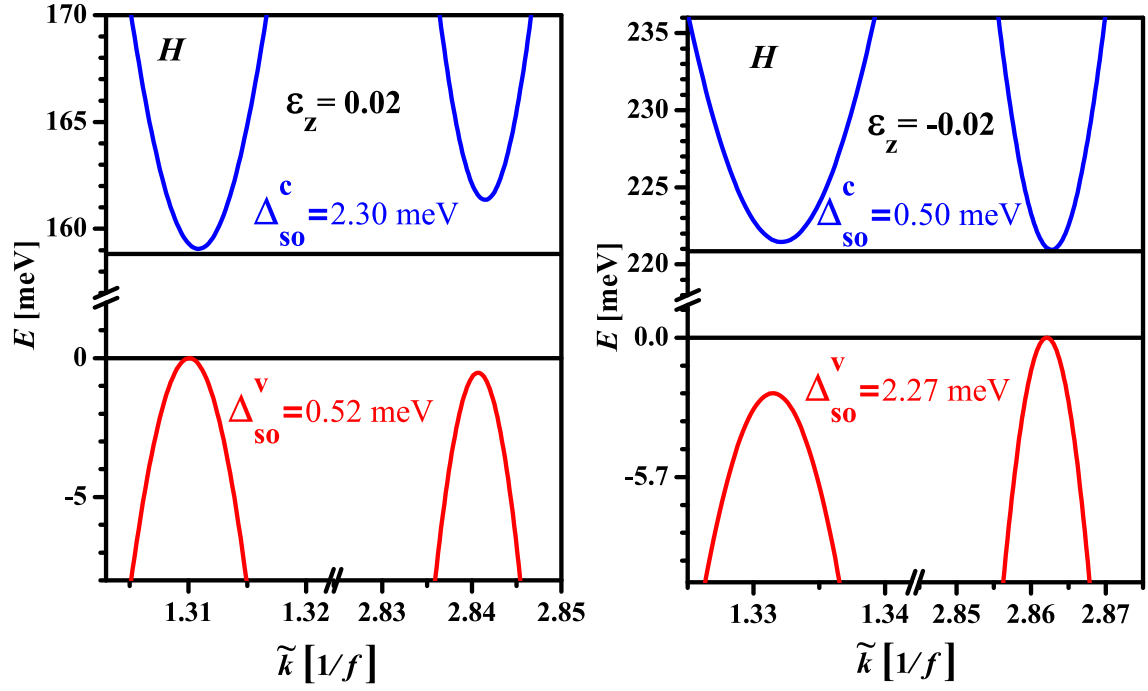


Figure 3.8: Influence of strain on lowest conductance and highest valence bands of tube (9,3). In the left panel stretching of the tube is 2%, while in the right panel compression $\varepsilon_z = -2\%$ is applied. Figure is taken from [36].

Chapter 4

Spin-orbit interaction in MoS₂ nanotubes

Monolayer MoS₂ is a direct band gap semiconductor [78–80] with pronounced spin splitting in the top valence band [81–85], due to the relatively high atomic number of Mo ($Z_{Mo} = 42$) and the fact that d orbitals of Mo carry the SOC. More concretely, DFT calculations [81, 84, 86] give spin-splitting in the top valence band of 147-148 meV, while the experiments find it to be in the range of 138-160 meV [87–92]. As for the minimum of the conductance band, theoretical results predict values from 1 meV to 3 meV [82, 84, 93].

On the other hand, when rolling-up a MoS₂ layer into a nanotube, as for SWCNTs, chiral, zig-zag and armchair tubes can be formed [94, 95], where the same description by the pair of numbers (n_1, n_2) is maintained. However, line groups describing the corresponding nanotubes are different than in the SWCNT case [96].

Electrical properties of MoS₂ nanotubes are also known [97–100]. Zig-zag MoS₂ tube is a direct gap semiconductor, where the maximum of the top valence and the minima of the bottom conductance band is placed at $k = 0$. Differently, armchair tube is an indirect gap semiconductor, with the maximum of valence bands at $k = 0$ and the minima of conductance bands at $ka \approx 2\pi/3$. It is worth noticing that local valence band maximum appears at the same point as the conductance band maximum, so its value can be measured by optical spectroscopy. Chiral MoS₂ nanotubes are not as studied as their carbon equivalents. The main reason probably lies in the fact that, up to our knowledge, there are no experimental reports on isolated single-wall chiral tubes. Nevertheless, chiral walls in multi-wall tubes are detected by diffractions [101].

As far as we are aware, SOC effects on the band structure of transition-metal dichalcogenide nanotubes have not been studied. In the case of SWCNTs, large SOC induced splitting as compared to the spin-orbit effects in graphene is commonly explained as a consequence of their curvature and cylindrical topology, motivating us to test this hypothesis in the case of a system whose layered counterpart has already large spin splitting values.

First, we construct double group of the corresponding diperiodic group of the monolayer, along with its IRs. Next, we perform symmetry based DFTB study of SOC effects. In this way we can establish a basis for comparison of curvature effects in nanotubes, being of central interest in this Chapter.

Some general results regarding the SOC effects in MoS₂ nanotubes will be analyzed using the results obtained for DLGs, given in Chapter 1. Finally, in order to examine the magnitude of SOC induced band/spin splitting, we will perform DFTB calculation, focusing on the local minima/maximum of the valence/conductance bands for all three types of nanotubes.

4.1 MoS₂ monolayer

Molybdenum disulfide monolayer [102] is made from three equal trigonal lattice planes (two sulfur and one molybdenum), with basis vectors \mathbf{a}_1 and \mathbf{a}_2 of the same length $a_0 = 3.16\text{\AA}$ [103]. Distance between sulfur planes is $\delta = 3.17\text{\AA}$ [104], with atoms in one plane straight below the other. Molybdenum plane is in the middle between sulfur planes, with their atoms in the center of sulfur triangles (see Fig. 4.1). Elementary cell consists of two S atoms, one from each plane, and one Mo atom.

Monolayer is invariant under translations of the form $n_1\mathbf{a}_1 + n_2\mathbf{a}_2$, where n_1 and n_2 are integer numbers, rotations around the axis perpendicular to the system for an angle $\pm 2\pi/3$ (\mathbf{C}_3 symmetry), horizontal and vertical mirror planes and their combinations. Thus, symmetry group of the MoS₂ layer is the symmorphic diperiodic group $\mathbf{G}_{\text{ml}} = \text{Dg78} = \mathbf{T} \wedge \mathbf{D}_{3h}$ [12, 105].

IRs of Dg78 group, necessary for performing symmetry based calculations, have already been constructed [12]. The procedure goes as follows: first, IRs of first diperiodic group $\text{Dg1} = \mathbf{T}$, being the pure translational group are found. Group $\text{Dg65} = \mathbf{C}_3\mathbf{T}$ is the semidirect product of subgroups Dg1 and \mathbf{C}_3 . In this case, induction procedure from the Abelian subgroup is necessary (see Appendix B.2) in

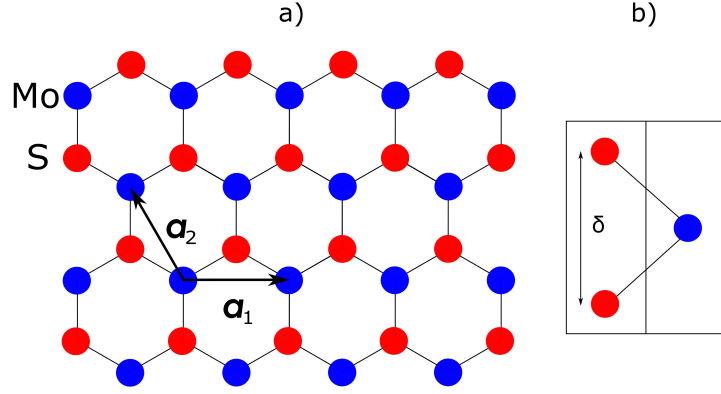


Figure 4.1: Structure of the MoS₂ monolayer: a) top and b) side view. Molybdenum atoms are labeled as blue, while sulfur atoms are red circles. Basis vectors of lattice plane are \mathbf{a}_1 and \mathbf{a}_2 , building an angle $2\pi/3$ between them. Distance between sulfur planes is δ .

order to find the corresponding IRs. After that, using the standard induction from invariant subgroup of index 2 (Appendix B.1), with an additional element σ_h , IRs of Dg74= $\mathbf{C}_{3h}\mathbf{T}$ are constructed. In the last step, IRs of Dg74 are needed to perform the induction from the invariant subgroup of index 2, with U being the additional element, yielding IRs of the desired group Dg78.

Irreducible domain of the Brillouin zone for the MoS₂ layer is given in Fig. 4.2: there are two special points $\Gamma = (0, 0)$ and $K = (\frac{2\pi}{3}, \frac{2\pi}{3})$, special lines $\Delta = (k, 0)$ and $\Phi = (0, k)$ ($k \in (0, \pi)$), while G represents generic points. The general label of the IR ${}^{\Pi_U}D_m^{\Pi_h}$ carries information about the symmetry-based QNs: subscript $\mathbf{k} = (k_1, k_2)$ is the wave vector from the irreducible domain, m is the angular momentum taking integer values, while parities Π_h and Π_U are equal to ± 1 . For an IR ${}^{k_2}_{k_1}G^{\Pi_h}$, corresponding to generic points G , parity Π_U and m are not defined, while values of k_1 and k_2 are from the interval $(0, \pi]$. In all other cases, instead of D , label of the special line/point is used.

4.1.1 Double group of Dg78

In order to find IRs of the double covering group of Dg78, i.e. $\widetilde{\text{Dg78}} = \widetilde{D}_{3h}\widetilde{\mathbf{T}}$, we use a different approach compared to that used for Dg78. Starting from the cyclic subgroup \mathbf{C}_3 , IRs of the double group $\widetilde{\mathbf{C}}_3$ are constructed. Next, as $\widetilde{\mathbf{C}}_{3h} = \widetilde{\mathbf{C}}_3 + \widetilde{\sigma}_v\widetilde{\mathbf{C}}_3$, corresponding IRs are found from the invariant subgroup of index 2, i.e. $\widetilde{\mathbf{C}}_3$. The

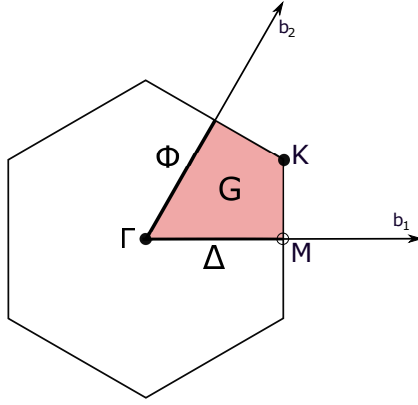


Figure 4.2: Irreducible domain of the Brillouin zone for diperiodic group $\mathbf{D}_{3h}\mathbf{T}$. Special points in the Brillouin zone, $\Gamma = (0,0)$ and $K = (\frac{2\pi}{3}, \frac{2\pi}{3})$, are marked with black circles. Special lines are $\Delta = (k, 0)$ and $\Phi = (0, k)$ ($k \in (0, \pi)$), while G represents generic points. Generic point $M = (\pi, 0)$ is marked with empty black circle.

same procedure can be applied to find IRs of $\widetilde{\mathbf{D}}_{3h}$ [16, 17]. Now, as $\widetilde{\text{Dg78}}$ is the semidirect product of $\widetilde{\mathbf{T}}$ and $\widetilde{\mathbf{D}}_{3h}$, induction procedure (Appendix B.2) from the Abelian subgroup is used to obtain IRs of the monolayers double group.

IRs of the double diperiodic group $\widetilde{\text{Dg78}}$ are listed in the Table 4.1. When compared to IRs of the single group, angular momentum m can take integer and half integer values, while the rest of the parities can now have four values $\Pi_h = \pm i, \pm 1$ and $\Pi_U = \pm i, \pm 1$. Additional parity for \tilde{e}' is defined, $\Pi_{\tilde{e}'} = \pm 1$, distinguishing integer from half integer representations, as $\Pi_{\tilde{e}'} = (-1)^{2m} = \Pi_h^2 = \Pi_U^2$. For half integer m parities can take the values $\Pi_h = \pm i$, $\Pi_U = \pm i$ and $\Pi_{\tilde{e}'} = (-1)^{2m} = -1$, while for integer m they can be $\Pi_h = \pm 1$, $\Pi_U = \pm 1$ and $\Pi_{\tilde{e}'} = (-1)^{2m} = 1$. The later are the extension of the single IRs of Dg78 to $\widetilde{\text{Dg78}}$.

It should be mentioned that IR ${}_{k_1}^{k_2}G^{\Pi_h}$ is not labeled with QN m . However, recall that $\tilde{\sigma}_h^2 = \tilde{e}'$, yielding $\Pi_{\tilde{e}'} = \Pi_h^2$. This IR is for generic points, i.e. monolayer bands are assigned by these IRs (aside from the special points and lines). Parities $\Pi_h = \pm 1$ and $\Pi_{\tilde{e}'} = 1$ correspond to the extension of IRs ${}_{k_1}^{k_2}G^{\Pi_h}$ of the single group to double group (integer representations). When the spin related properties are addressed, QNs $\Pi_h = \pm i$ and $\Pi_{\tilde{e}'} = -1$ (half integer representations) labeled IRs are assigned to the bands.

In the Table 4.1, unit matrix of dimension d is written as 1_d . Additionally, we

have used the following matrices

$$\begin{aligned} E_3 &= \text{diag}(e^{ik_1}, e^{-i(k_1+k_2)}, e^{ik_2}), D_3 = \text{diag}(e^{i(k_1+k_2)}, e^{-ik_2}, e^{-ik_1}), \\ N_3 &= \text{diag}(e^{ik_2}, e^{ik_1}, e^{-i(k_1+k_2)}), M(m) = \text{diag}(e^{im\frac{2\pi}{3}}, e^{-im\frac{2\pi}{3}}), \end{aligned} \quad (4.1)$$

$$\begin{aligned} K_{\Delta_1} &= \text{diag}(e^{ik}, e^{-ik}, 1), K_{\Delta_2} = \text{diag}(1, e^{ik}, e^{-ik}), \\ K_{\Phi_1} &= \text{diag}(1, e^{-ik}, e^{ik}), K_{\Phi_2} = \text{diag}(e^{ik}, 1, e^{-ik}), \end{aligned} \quad (4.2)$$

$$A = \begin{bmatrix} 0 & 0 & \Pi_{\tilde{e}'} \\ 1 & 0 & 0 \\ 0 & 1 & 0 \end{bmatrix}, B = \begin{bmatrix} 1 & 0 & 0 \\ 0 & 0 & \Pi_{\tilde{e}'} \\ 0 & \Pi_{\tilde{e}'} & 0 \end{bmatrix}, C = \Pi_{\tilde{e}'} \begin{bmatrix} 0 & 0 & 1 \\ 0 & 1 & 0 \\ 1 & 0 & 0 \end{bmatrix}. \quad (4.3)$$

4.1.2 SOC effects for the monolayer

Having all the IRs found, symmetry based analysis of the SOC effects on orbital bands can be performed. First task is to find the Clebsch-Gordan series for the product $D^{(\mu)}(\tilde{\mathbf{G}}_{\text{ml}}) \otimes u(\tilde{\mathbf{G}}_{\text{ml}})$. For the IRs $\Pi_U \Gamma_0^{\Pi_h}(\tilde{\mathbf{G}}_{\text{ml}})$, $\Pi_U \Delta_0^{\Pi_h}(\tilde{\mathbf{G}}_{\text{ml}})$ and $\Pi_U \Phi_0^{\Pi_h}(\tilde{\mathbf{G}}_{\text{ml}})$, products are the following

$$\Pi_U \Gamma_0^{\Pi_h}(\tilde{\mathbf{G}}_{\text{ml}}) \otimes u(\tilde{\mathbf{G}}_{\text{ml}}) = \Gamma_{\frac{1}{2}}^{\text{i}\Pi_h}(\tilde{\mathbf{G}}_{\text{ml}}), \quad (4.4)$$

$$\Pi_U \Delta_0^{\Pi_h}(\tilde{\mathbf{G}}_{\text{ml}}) \otimes u(\tilde{\mathbf{G}}_{\text{ml}}) = {}_k\Delta(\tilde{\mathbf{G}}_{\text{ml}}), \quad (4.5)$$

$$\Pi_U \Phi_0^{\Pi_h}(\tilde{\mathbf{G}}_{\text{ml}}) \otimes u(\tilde{\mathbf{G}}_{\text{ml}}) = {}_k\Phi_{\frac{1}{2}}(\tilde{\mathbf{G}}_{\text{ml}}), \quad (4.6)$$

Thus, in these cases there is no band splitting, and consequently there is no possibility to lift the spin degeneracy by SOC.

On the other hand, for the IRs $\Gamma_1^{\Pi_h}(\tilde{\mathbf{G}}_{\text{ml}})$, $K_m^{\Pi_h}(\tilde{\mathbf{G}}_{\text{ml}})$ and ${}^{k_2}_{k_1}G^{\Pi_h}(\tilde{\mathbf{G}}_{\text{ml}})$ band splitting is allowed, as

$$\Gamma_1^{\Pi_h}(\tilde{\mathbf{G}}_{\text{ml}}) \otimes u(\tilde{\mathbf{G}}_{\text{ml}}) = \Gamma_{\frac{1}{2}}^{-\text{i}\Pi_h}(\tilde{\mathbf{G}}_{\text{ml}}) \oplus \Gamma_{\frac{3}{2}}(\tilde{\mathbf{G}}_{\text{ml}}), \quad (4.7)$$

$$K_m^{\Pi_h}(\tilde{\mathbf{G}}_{\text{ml}}) \otimes u(\tilde{\mathbf{G}}_{\text{ml}}) = K_{m+\frac{1}{2}}^{\text{i}\Pi_h}(\tilde{\mathbf{G}}_{\text{ml}}) \oplus K_{m-\frac{1}{2}}^{-\text{i}\Pi_h}(\tilde{\mathbf{G}}_{\text{ml}}), \quad (4.8)$$

$${}^{k_2}_{k_1}G^{\Pi_h}(\tilde{\mathbf{G}}_{\text{ml}}) \otimes u(\tilde{\mathbf{G}}_{\text{ml}}) = {}^{k_2}_{k_1}G^{\text{i}\Pi_h}(\tilde{\mathbf{G}}_{\text{ml}}) \oplus {}^{k_2}_{k_1}G^{-\text{i}\Pi_h}(\tilde{\mathbf{G}}_{\text{ml}}). \quad (4.9)$$

First, although the above result for $\Gamma_1^{\Pi_h}(\tilde{\mathbf{G}}_{\text{ml}})$ suggests that spin splitting may occur, this is not the case. The IR $\Gamma_1^{\Pi_h}(\tilde{\mathbf{G}}_{\text{ml}})$ is two-dimensional and its SAB contains

Table 4.1: IRs of the diperiodic double group $\widetilde{Dg78} = \widetilde{\mathbf{D}}_{3h}\widetilde{\mathbf{T}}$. Symbol of IRs can be found in the column 1. In the column 2, range of corresponding QNs (k, m) is given. In cases when IR is not labeled by m , parity of $\Pi_{\tilde{e}'}$ is provided, helping us to distinguish between integer and half integer representations. In columns 3-7, matrices of the generators are presented. Element \tilde{e}' , represented by the matrix $\Pi_{\tilde{e}'}\mathbb{1}_d$, where d is the IRs dimension, is not tabulated since its representation is a priori known.

IR	(k, m)	\tilde{C}_3	$\tilde{\sigma}_h$	\tilde{U}	$(\widetilde{\mathbb{1} 10})$	$(\widetilde{\mathbb{1} 01})$
$\Pi_U \Gamma_m^{\Pi_h}$	$k = 0$ $m = 0$	1	Π_h	Π_U	1	1
$\Gamma_m^{\Pi_h}$	$k = 0$ $m = \frac{1}{2}, 1$	$M(m)$	$\Pi_h \begin{bmatrix} 1 & 0 \\ 0 & \Pi_{\tilde{e}'} \end{bmatrix}$	$\begin{bmatrix} 0 & \Pi_{\tilde{e}'} \\ 1 & 0 \end{bmatrix}$	$\mathbb{1}_2$	$\mathbb{1}_2$
Γ_m	$k = 0$ $m = \frac{3}{2}$	$-\mathbb{1}_2$	$\begin{bmatrix} -i & 0 \\ 0 & i \end{bmatrix}$	$\begin{bmatrix} 0 & -1 \\ 1 & 0 \end{bmatrix}$	$\mathbb{1}_2$	$\mathbb{1}_2$
${}_k K_m^{\Pi_h}$	$k = \frac{2\pi}{3}$ $m \in (-\frac{3}{2}, \frac{3}{2}]$	$M(m)$	$\Pi_h \begin{bmatrix} 1 & 0 \\ 0 & \Pi_{\tilde{e}'} \end{bmatrix}$	$\begin{bmatrix} 0 & \Pi_{\tilde{e}'} \\ 1 & 0 \end{bmatrix}$	$\begin{bmatrix} e^{ik} & 0 \\ 0 & e^{-ik} \end{bmatrix}$	$\begin{bmatrix} e^{ik} & 0 \\ 0 & e^{-ik} \end{bmatrix}$
$\Pi_U \Delta_k^{\Pi_h}$	$k \in (0, \pi]$ $\Pi_{\tilde{e}'} = 1$	A	$\Pi_h \mathbb{1}_3$	$\Pi_U B$	K_{Δ_1}	K_{Δ_2}
${}_k \Delta$	$k \in (0, \pi]$ $\Pi_{\tilde{e}'} = -1$	$A \otimes \mathbb{1}_2$	$\mathbb{1}_3 \otimes \begin{bmatrix} 0 & -1 \\ 1 & 0 \end{bmatrix}$	$B \otimes \begin{bmatrix} i & 0 \\ 0 & -i \end{bmatrix}$	$K_{\Delta_1} \otimes \mathbb{1}_2$	$K_{\Delta_2} \otimes \mathbb{1}_2$
$\Pi_U \Phi_k^{\Pi_h}$	$k \in (0, \pi]$ $\Pi_{\tilde{e}'} = 1$	A	$\Pi_h \mathbb{1}_3$	$\Pi_U C$	K_{Φ_1}	K_{Φ_2}
${}_k \Phi$	$k \in (0, \pi]$ $\Pi_{\tilde{e}'} = -1$	$A \otimes \mathbb{1}_2$	$\mathbb{1}_3 \otimes \begin{bmatrix} 0 & -1 \\ 1 & 0 \end{bmatrix}$	$C \otimes \begin{bmatrix} i & 0 \\ 0 & -i \end{bmatrix}$	$K_{\Phi_1} \otimes \mathbb{1}_2$	$K_{\Phi_2} \otimes \mathbb{1}_2$
${}_{k_1}^{k_2} G^{\Pi_h}$	$k_{1,2} \in (0, \pi]$	$\begin{bmatrix} A & 0 \\ 0 & A^{-1} \end{bmatrix}$	$\Pi_h \begin{bmatrix} \mathbb{1}_3 & 0 \\ 0 & \Pi_{\tilde{e}'} \mathbb{1}_3 \end{bmatrix}$	$\begin{bmatrix} 0 & \Pi_{\tilde{e}'} \mathbb{1}_3 \\ \mathbb{1}_3 & 0 \end{bmatrix}$	$\begin{bmatrix} E_3 & 0 \\ 0 & D_3 \end{bmatrix}$	$\begin{bmatrix} N_3 & 0 \\ 0 & N_3^* \end{bmatrix}$

vectors $|0m\Pi_h\rangle$ and $|0 - m\Pi_h\rangle$ with opposite sign of angular momentum. However, since \tilde{U} maps one vector onto another (up to a phase), spin splitting is forbidden. The same is valid for two half integer IRs which appear in the decomposition (4.7). In this case, their SABs $\{|0, \frac{1}{2}, \Pi_h\rangle, |0, -\frac{1}{2}, \Pi_h\rangle\}$ and $\{|0, \frac{3}{2}, \Pi_h\rangle, |0, -\frac{3}{2}, \Pi_h\rangle\}$ have vectors that can be mapped via \tilde{U} one onto the other.

Band splitting is allowed at the K point, as follows from (4.7). Furthermore, $\tilde{\sigma}_h$ does not affect orbital and spin state (up to a phase)

$$D(\tilde{\sigma}_h) |\mathbf{k}m\Pi_h\rangle |s_z\rangle = s_z i \Pi_h |\mathbf{k}m\Pi_h\rangle |s_z\rangle, \quad (4.10)$$

yielding that the two branches have opposite spin polarization. Thus, spin splitting is present at the K point. Elements $\tilde{\sigma}_v$ and \tilde{U} , as well as time reversal symmetry, maps (up to the phase) $|\mathbf{k}m\Pi_h\rangle$ onto $|\mathbf{k} - m\Pi_h\rangle$ while changing the spin orientation.

Finally, in the case of an IR ${}_{k_1}^{k_2}G^{\Pi_h}(\tilde{\mathbf{G}}_{ml})$, it can be shown that spin splitting is allowed. Since QN m is not present in this case, orbital eigenvector from the SAB is labeled as $|\mathbf{k}\Pi_h\rangle$. When the spin degree of freedom is included, the eigenstate has the following form

$$|\psi\rangle \doteq |\mathbf{k}, \pm i\rangle = |\mathbf{k}\Pi_h\rangle (a|\uparrow\rangle + b|\downarrow\rangle), \quad (4.11)$$

where $|\uparrow\rangle, |\downarrow\rangle$ are spin projections along the direction perpendicular to the layer. Group element $\tilde{\sigma}_h$ transforms the vector $|\psi\rangle$ to

$$D(\tilde{\sigma}_h) |\psi\rangle = \Pi_h |\mathbf{k}\Pi_h\rangle (ia|\uparrow\rangle - ib|\downarrow\rangle). \quad (4.12)$$

On the other hand, as vector $|\psi\rangle$ is from the SAB of the IR, it follows that

$$D(\tilde{\sigma}_h) |\psi\rangle = \pm i |\psi\rangle = |\mathbf{k}\Pi_h\rangle (\pm ia|\uparrow\rangle \mp ib|\downarrow\rangle), \quad (4.13)$$

giving the restrictions on a and b

$$\pm ia = \Pi_h ia \quad \text{and} \quad \mp ib = -\Pi_h ib. \quad (4.14)$$

There are two possible solutions: $a = 1, b = 0$ and $a = 0, b = 1$, meaning that $|\psi\rangle$ must be spin-up or spin-down polarized. Thus, orbital band with defined parity Π_h splits into two branches that differ in QN $\Pi_h = i, -i$ with opposite sign of spin polarization. Furthermore, for fixed \mathbf{k} , note that the action on $|\psi\rangle$ by the group element that change spin direction, such as $\tilde{\sigma}_v$ and \tilde{U} , gives eigenvector at different position in the Brillouin zone with opposite polarization. The same conclusions

can be drawn for time reversal symmetry and, as mentioned above, is also valid for the K point. Thus, electrons located at valence/conductance band at the K and K' points have opposite spin directions, yielding spin-valley locking in these materials [106–108].

Spin splitting in valence and conductance bands

Next, we perform numerical calculations of the electronic bands of the total Hamiltonian $H = H_o + H_{so}$ using the POLSym code. MoS₂ layer is a system made from two orbits: one formed by one Mo and the other by one S atom (as group element σ_h transforms one S plane into the other). From each atom, only the valence shell orbitals are considered. In particular, for S one 3s and three 3p, while for Mo 5s, 5p and 4d atomic orbitals are used. SOC effects are included within the on-site atomic approximation, with spin-orbit constants $\lambda_S = 50\text{meV}$ for 3p orbitals of sulfur and $\lambda_{Mo} = 87\text{meV}$ for 4d orbitals of molybdenum [84]. The same orbitals and spin-orbit constants will be used later in the study of SOC effects in MoS₂ nanotubes.

As zone folding allows us to relate their valence and conductance bands (within a crude approximation) to the valence and conductance bands of nanotubes, we analyze SOC effects on the layer's valence and conductance bands. In Fig. 4.3 a), we plot the highest valence and the lowest conductance electron band along the $\Gamma - K - M - \Gamma$ line. Corresponding symmetry labels on the whole line are also given. In Fig. 4.3 b) effect of SOC on these bands can be seen.

Borders of the $\Gamma - K$ line represent special points, while points between them belong to the generic G domain. According to (4.4) and (4.7), spin splitting is absent at the Γ point, while the maximal 147 meV value of valence band splitting is located at the K point. This results are in line with both theoretical [81, 82, 84, 86] and experimental values [87–92].

On the other hand, maximum spin splitting of the conductance band is located in the middle of the $\Gamma - K$ line, i.e. around the $Q = (\pi/3, \pi/3)$ point. Along the $K - M$ line, which belongs to the G domain, spin splitting is also allowed, according to (4.9). For the valence band, spin splitting value decreases to zero, while for the conductance band there is a rise of spin splitting, followed by a decline to zero. Finally, band splitting is zero along the $M - \Gamma$ line, as symmetry analysis shows for all points that belong to the Δ domain.

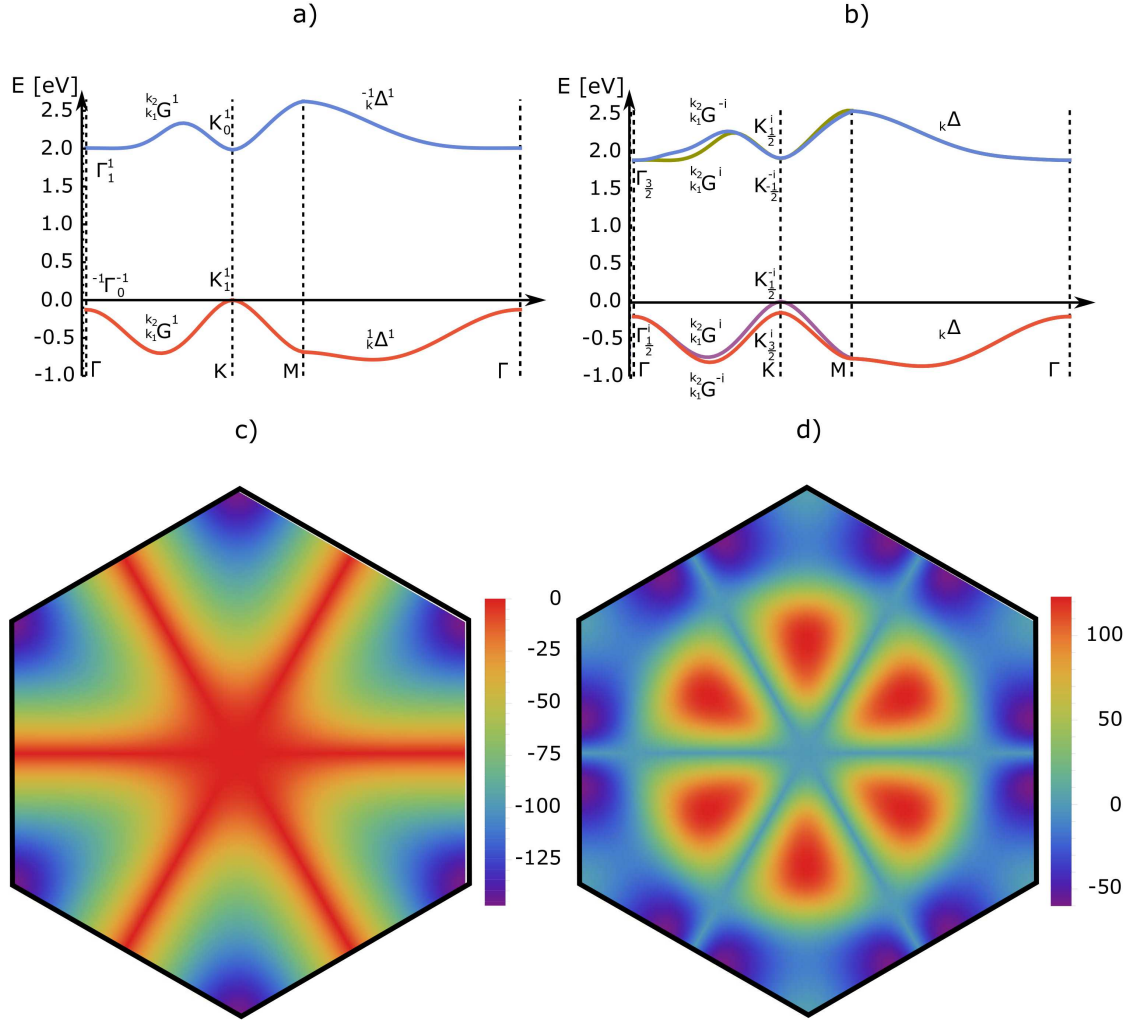


Figure 4.3: MoS₂ monolayer bands. a) The top valence and the bottom conduction electronic bands along the $\Gamma - K - M - \Gamma$ direction. Symmetry label of each point along this direction is given. b) Spin splitting of these bands along the same direction. Each point is now labeled by double group IRs. c) Density plot of the top valence and the d) bottom conduction band splitting, induced by SOC.

In the G domain, we have defined spin splitting as

$$\Delta_{v/c}^{so}(\mathbf{k}) = \mathcal{E}_{v/c}^{\uparrow} - \mathcal{E}_{v/c}^{\downarrow}. \quad (4.15)$$

Density plots of spin splitting values of the top valence and the lowest conductance band in the whole Brillouin zone are shown in Fig. 4.3 c) and d), respectively. Evidently, splitting of the valence bands is such that at the K point branch with higher energy is \downarrow polarized, i.e. the sign of $\Delta_V^{so}(K)$ is negative. Conductance band has the opposite behaviour: the branch with lower energy is \downarrow polarized, meaning that $\Delta_c^{so}(K)$ is positive. Beside already mentioned zero splitting along the Δ line, plots also show zero splitting along the Φ line, according to (4.6). Also, maximal value of valence/conductance band splitting is placed along the $\Gamma - K$ line.

In the end, in Fig. 4.4 and Fig. 4.5, orbital contribution (OC) in the top valence and the lowest conductance band is given. Note that Mo p_0 and $d_{\pm 1}$ orbitals have exact zero OC since considered bands have QN $\Pi_h = 1$ (i.e. their eigenstates have to be invariant under σ_h ; thus, Mo orbitals of odd parity are excluded).

Generally, plots show dominant contribution of Mo $d_{\pm 2}$ and d_0 orbitals in these bands. Since the term $L_z s_z$ of the SOC Hamiltonian is the dominant and $L_z d_l = l d_l$, it is reasonable to claim that d_0 contribute to zero spin splitting value, while $d_{\pm 2}$ gives nonzero spin splitting. Thus, dominant OC of d_2 orbital in the valence band at the K point suggests position of the maximal spin splitting. In the conductance band, maximal value of spin splitting is near the Q point, due to the dominant OC of d_{-2} orbital. Also, at the K point, d_0 is dominant, suggesting weak spin splitting.

In Fig. 4.6 OC of valence Mo $d_{-2} + d_2$ and d_0 orbitals, as well as $p_{-1} + p_1$ and p_0 S orbitals is given, since they are relevant for the SOC effects. Our results qualitatively agree with [81], except in one minor difference. Their calculations suggest very weak contribution of $d_{xz} + d_{yz}$ ¹ orbitals. As clarified above, symmetry bans their contribution.

4.2 MoS₂ nanotubes

As for the graphene, the molybdenum monolayer can be cut and then rolled-up in such a way that vector $\mathbf{c} = n_1 \mathbf{a}_1 + n_2 \mathbf{a}_2$ becomes a diameter of the MoS₂ (n_1, n_2)

¹By definition, $d_{x^2-y^2}$, d_{xy} , d_{z^2} , d_{xz} and d_{yz} orbitals are equal to $1/\sqrt{2}(d_{-2}+d_2)$, $i/\sqrt{2}(d_{-2}-d_2)$, d_0 , $1/\sqrt{2}(d_{-1}-d_1)$ and $i/\sqrt{2}(d_{-1}+d_1)$, respectively.

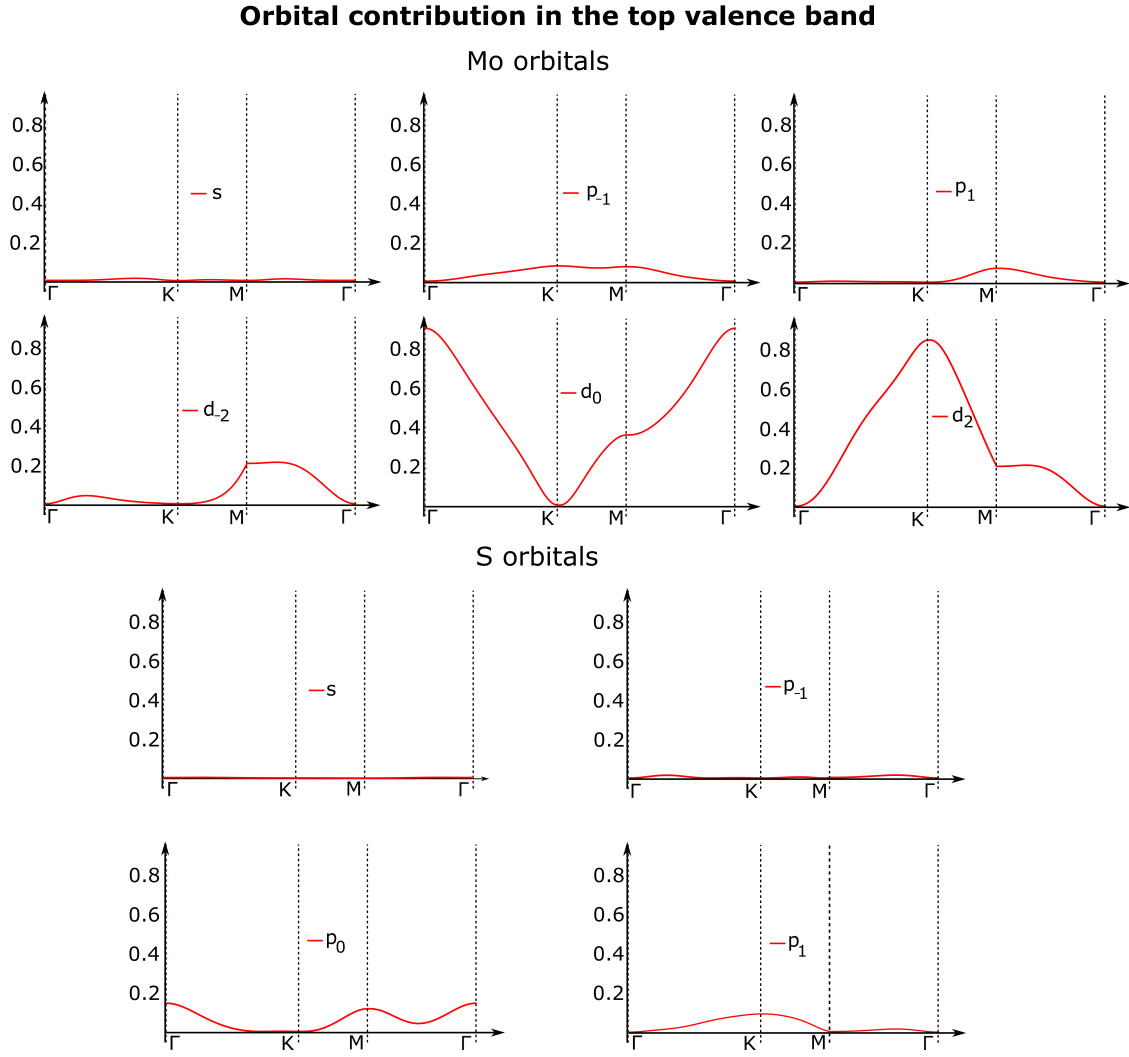


Figure 4.4: OC in the top valence band along the $\Gamma - K - M - \Gamma$ direction.

nanotube (see Fig. 4.7). Due to the monolayer symmetry, it suffices to consider the tubes with chiral angle $\theta_c = \arctan(\sqrt{3}n_2/(2n_1 + n_2))$ (i.e. the angle between vectors \mathbf{a}_1 and \mathbf{c}) within the range of $[0, \pi/3)$.

Their symmetry, depending on the chiral vector (as in SWCNTs) was derived by Milošević et al. [96]. Rolled up structure has the translational symmetry along the tube axis, but it also possesses screw axis symmetry, with parameters q, r, f defined by the chiral vector coordinates, in the same manner as in SWCNTs (3.5). Tube can have rotational symmetry around the tube axis \mathbf{C}_n , with $n = \text{GCD}(n_1, n_2)$, but it lacks rotational symmetry around the horizontal axis U . As for mirror symmetries,

Orbital contribution in the bottom conductance band

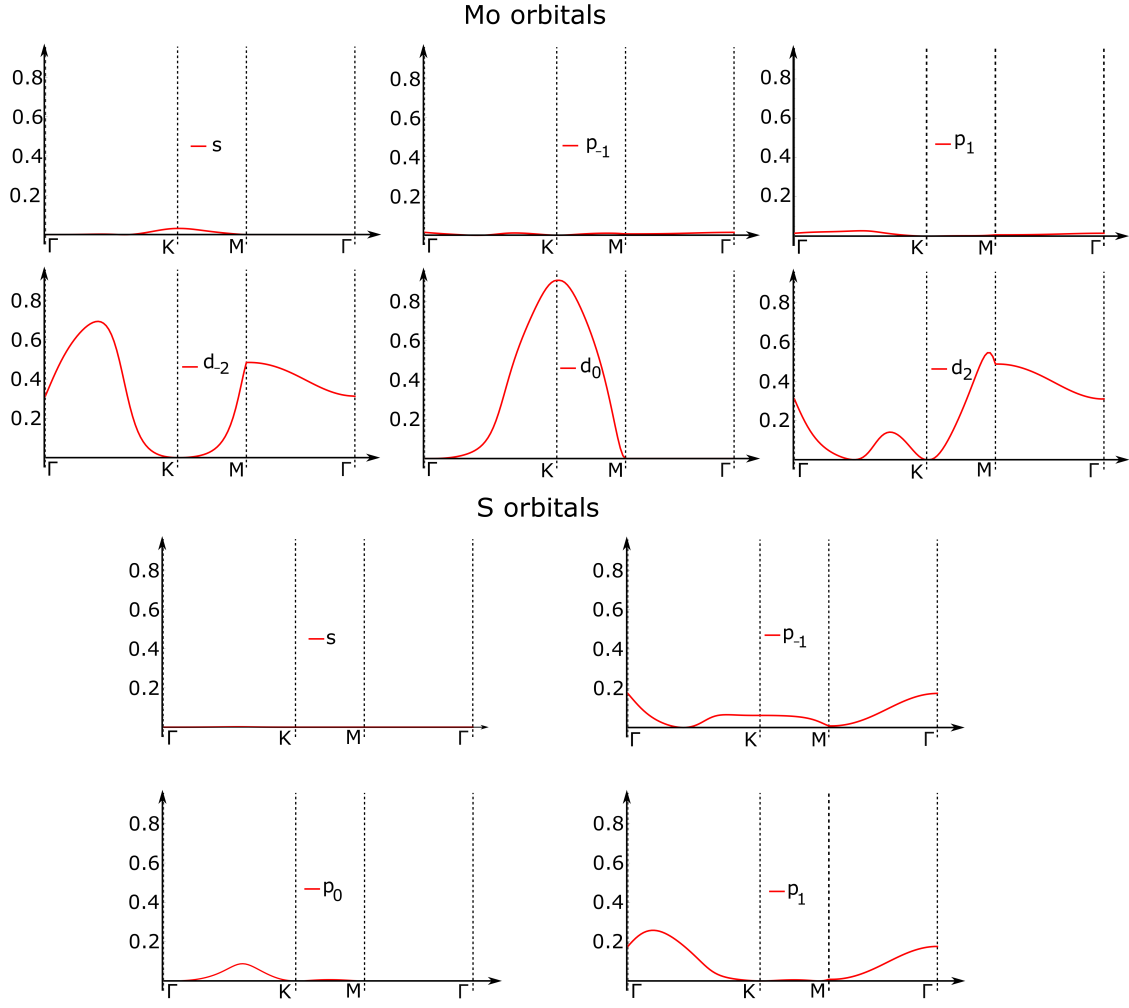


Figure 4.5: OC in the bottom conductance band along the $\Gamma - K - M - \Gamma$ direction.

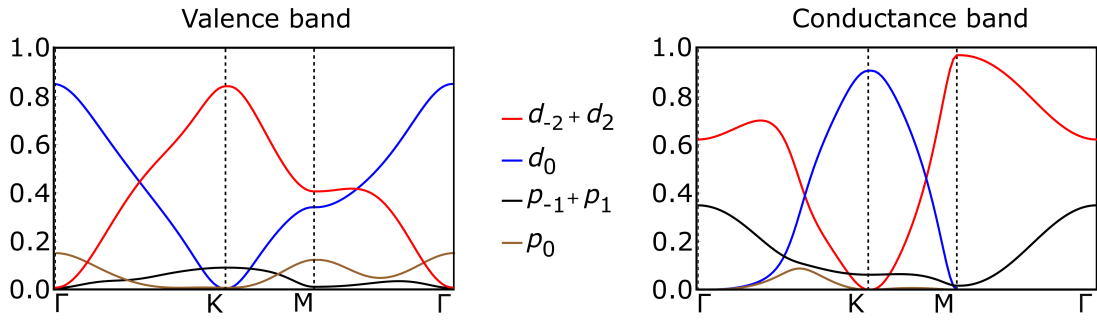


Figure 4.6: OC of valence Mo $d_{-2} + d_2$ and d_0 orbitals, as well as $p_{-1} + p_1$ and p_0 S orbitals in the top valence (left panel) and the bottom conductance (right panel) band.

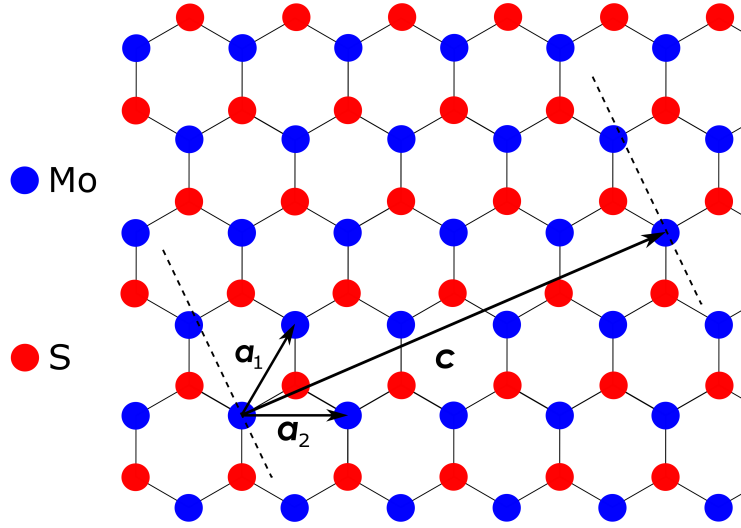


Figure 4.7: Nanotube (n_1, n_2) is obtained by rolling-up the molybdenum plane around the vector $\mathbf{c} = n_1 \mathbf{a}_1 + n_2 \mathbf{a}_2$, where \mathbf{a}_1 and \mathbf{a}_2 are basis vectors of the lattice plane.

the armchair tubes (n, n) have σ_h while zig-zag ones $(n, 0)$ have σ_v . Therefore, general classification of tubes into chiral \mathcal{C} and achiral ones (armchair \mathcal{A} and zig-zag \mathcal{Z}) remains valid in this case. Again, tubes (n_2, n_1) with nonnegative integers $n_1 \leq n_2$, i.e. with $\theta_c \in (\pi/6, \pi/3)$, are optical isomers of tubes (n_1, n_2) having $\theta_c \in (0, \pi/6)$.

To conclude, group of the geometrical symmetries of chiral, i.e. (n_1, n_2) with unequal nonzero integers n_1 and n_2 , MoS₂ nanotubes belong to the first family line groups [96]

$$\mathbf{L}_{\mathcal{C}} = \mathbf{T}_q^r(a) \mathbf{C}_n, \quad (4.16)$$

while for armchair and zig-zag ones they are from the fourth and the eighth family line groups, respectively [96]

$$\mathbf{L}_{\mathcal{A}} = \mathbf{T}_{2n}^1(a_0) \mathbf{C}_{nh}, \quad (4.17)$$

$$\mathbf{L}_{\mathcal{Z}} = \mathbf{T}_{2n}^1(\sqrt{3}a_0) \mathbf{C}_{nv}. \quad (4.18)$$

As compared to SWCNTs, the main difference between them and MoS₂ tubes lies in the fact that MoS₂ tubes actually have three walls or cylinders: inner and outer ones are formed by sulfur atoms, while the one in the middle is formed from

molybdenum atoms. As rolling of the monolayer destroys the symmetry which maps one sulfur plane into another, tube is three orbital system: one $\mathbf{r}_{00}^i = (\rho_i, \varphi_i, z_i)$ for each cylinder (inner sulfur S_{in} , molybdenum Mo and outer sulfur S_{out} , respectively)

$$\mathbf{r}_{00}^{S_{\text{in}}} = (\frac{D - \delta}{2}, 0, 0), \mathbf{r}_{00}^{Mo} = (\frac{D}{2}, \varphi_0, z_0), \mathbf{r}_{00}^{S_{\text{out}}} = (\frac{D + \delta}{2}, 0, 0), \quad (4.19)$$

where molybdenum cylindrical coordinates are

$$D = \frac{\sqrt{n_1^2 + n_1 n_2 + n_2^2} a_0}{\pi}, \quad (4.20)$$

$$\varphi_0 = \pi \frac{n_1 + n_2}{n_1^2 + n_1 n_2 + n_2^2}, \quad (4.21)$$

$$z_0 = \frac{a_0}{2\sqrt{3}} \frac{n_1 - n_2}{\sqrt{n_1^2 + n_1 n_2 + n_2^2}}. \quad (4.22)$$

For chiral tubes, position of each atom \mathbf{r}_{ts}^i of all orbits is obtained by the action of the group element $\ell_{ts} = (C_q^r | qa/n)^t C_n^s$ on the orbit representatives \mathbf{r}_{00}^i . In this case, each orbit representative has trivial stabilizer. In the \mathcal{Z} case, coordinates of the orbit representatives are given in (4.19), where $D = na_0/\pi$, $\varphi_0 = \pi/n$ and $z_0 = \sqrt{3}a_0/6$. In order to generate the system in this case, it is enough to take the elements of the first family line group with $r = 1$ and $q = 2n$, since σ_v represents stabilizer element. Finally, in the \mathcal{A} case, equation (4.19) yields one should take $D = \sqrt{3}a_0/\pi$, $\varphi_0 = 2\pi/3n$ and $z_0 = 0$. Stabilizer is again nontrivial as it contains horizontal mirror plane σ_h , i.e. again the first family subgroup $\mathbf{T}_{2n}^1(a_0)$ of the tube's symmetry group is sufficient to generate the whole system. To conclude, for MoS_2 nanotube (n_1, n_2) positions of atoms are given by

$$\mathbf{r}_{ts}^i = (C_q^r | \frac{q}{n}a)^t C_n^s \mathbf{r}_{00}^i = (\rho_i, \varphi_i + 2\pi(\frac{rt}{q} + \frac{s}{n}), z_i + \frac{q}{n}ta), \quad (4.23)$$

where q, r, n, a are the parameters of its first family group and subgroup for the chiral and achiral case, respectively.

Finally, we note that rolled-up configuration does not describe equilibrium position, especially for tubes with smaller diameter [100]. For all studied tubes, symmetry preserving relaxation procedure described in Chapter 3.1.1 had to be performed before numerical analysis of SOC effects on the electronic bands. The procedure itself is more time consuming, compared to SWCNTs, as the system consists of three orbits. In the chiral MoS_2 nanotube case, torsion τ and axial strain ϵ_z can

be applied. Also the following cylindrical coordinates of three orbit representatives can be varied: $\Delta D_{S_{in}}$, $\Delta \varphi_{S_{in}}$, $\Delta z_{S_{in}}$, ΔD_{Mo} , $\Delta D_{S_{out}}$, $\Delta \varphi_{S_{out}}$ and $\Delta z_{S_{out}}$. In the achiral case, torsion τ is not allowed, since τ changes the symmetry of the system. Additionally, \mathcal{A} nanotubes do not allow changing of z coordinate of sulfurs, while \mathcal{Z} nanotubes forbid change of φ coordinate of sulfur orbit representatives.

4.2.1 Armchair tubes

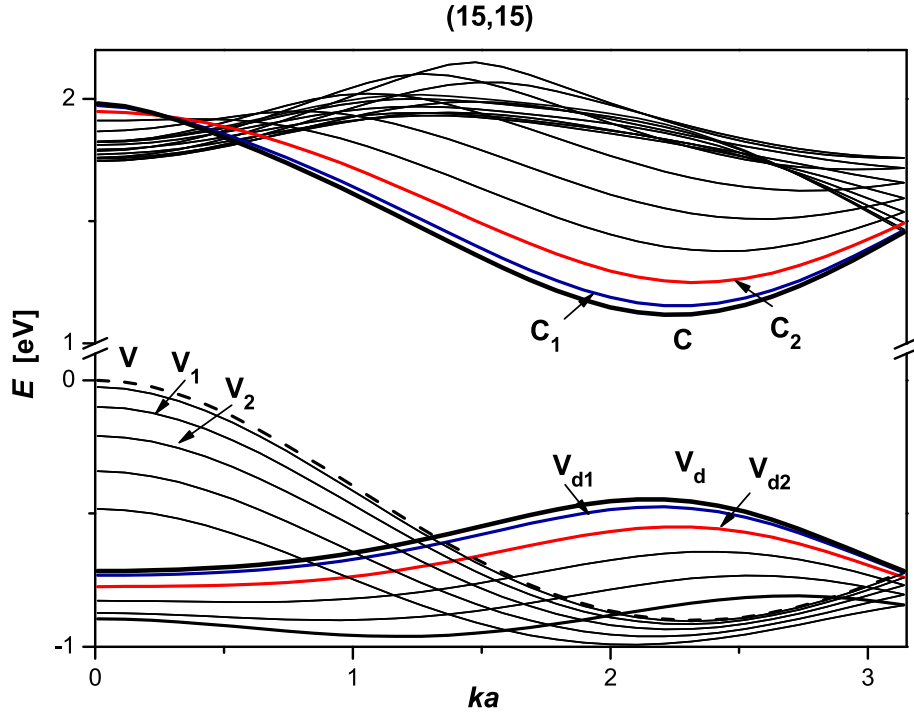


Figure 4.8: Electronic orbital bands of the armchair (15,15) tube.

All armchair tubes are small indirect gap semiconductors [98–100], with valence band maximum placed at $ka = 0$ and conduction band minimum at $ka \approx 2\pi/3$. In addition to the indirect gap, direct band gaps are present at $ka = 0$ and $ka \approx 2\pi/3$. Indirect band gap varies from 1.10 eV for tubes with 2 nm diameter to the saturation value 1.15 eV for >9 nm diameter tubes, while direct gap at $ka = 0$ is in the range from 1.125 eV for 2 nm to ~ 1.30 eV for >15 nm diameter tubes. On the other side, direct gap at $ka = 2\pi/3$ is almost independent on tube's diameter (~ 1.27 eV). As an illustration, in Fig. 4.8 band structure of the armchair (15,15) nanotube is presented. We will particularly focus on top three valence (v , v_1 and v_2), bottom

three conductance (c , c_1 and c_2) and three valence bands with local maximum at $ka \approx 2\pi/3$ indirect band gap (v_d , v_{d_1} and v_{d_2}).

Appearance of band splitting can be determined by studying the Clebsch-Gordan series of a tensor product of orbital group IRs and spin representation. Group of geometrical symmetries $\mathbf{L}_{\mathcal{A}}$ have one- and two-dimensional IRs. One-dimensional IRs are present in $k = 0$ point and labeled as ${}_0A_m^{\Pi_h}$, with $m \in (-n, n]$ and $\Pi_h = \pm 1, \pm i$. For integer m , ± 1 parity values are used, while half integer m yields $\pm i$ values of parity. Time-reversal symmetry θ connects $|0m\Pi_h\rangle$ to $|0-m-\Pi_h\rangle$, changing angular momentum and parity of the SAB vector. Thus, it is enough to consider IRs with positive angular momenta m and $\Pi_h = \pm 1, \pm i$. In the special $m = 0/n$ case, it is enough to consider $\Pi_h = 1, i$.

All other points of the irreducible Brillouin zone are labeled by two-dimensional IRs ${}_kE_m$. More concretely, allowed QNs are: $k \in (0, \pi/a]$, $m \in (-n, n]$ and $k = \pi/a$, $m \in [0, n)$. SAB is spanned by two vectors $|km\rangle$ and $|-km\rangle$. Time reversal symmetry transform these vectors to $|-k-m\rangle$ and $|k-m\rangle$, respectively, which belong to the IR ${}_kE_{-m}$. Thus, we have established connection between IRs with positive and negative angular momentum m , yielding the usage of IRs with $m \geq 0$ solely.

By knowing the IRs, we can investigate the possibility of SOC to induce band splitting.² To this end, we calculate Clebsch-Gordan series of the tensor product of one/two-dimensional IRs and spin representation

$${}_0A_{m_0}^{\pm}(\tilde{\mathbf{L}}_{\mathcal{A}}) \otimes u(\tilde{\mathbf{L}}_{\mathcal{A}}) = {}_0A_{m_0+\frac{1}{2}}^{\pm i}(\tilde{\mathbf{L}}_{\mathcal{A}}) \oplus {}_0A_{m_0-\frac{1}{2}}^{\mp i}(\tilde{\mathbf{L}}_{\mathcal{A}}), \quad (4.24)$$

$${}_kE_{m_o}(\tilde{\mathbf{L}}_{\mathcal{A}}) \otimes u(\tilde{\mathbf{L}}_{\mathcal{A}}) = {}_kE_{m_o+\frac{1}{2}}(\tilde{\mathbf{L}}_{\mathcal{A}}) \oplus {}_kE_{m_o-\frac{1}{2}}(\tilde{\mathbf{L}}_{\mathcal{A}}). \quad (4.25)$$

Equations (4.24) and (4.25) suggest that band splitting is possible, except in some special cases: Clebsch-Gordan series for IRs ${}_0A_0^{\pm}(\tilde{\mathbf{L}}_{\mathcal{A}})$ and ${}_0A_n^{\pm}(\tilde{\mathbf{L}}_{\mathcal{A}})$ gives direct products of IRs

$$\begin{aligned} &{}_0A_{1/2}^{\pm i}(\tilde{\mathbf{L}}_{\mathcal{A}}) \oplus {}_0A_{-1/2}^{\mp i}(\tilde{\mathbf{L}}_{\mathcal{A}}), \\ &{}_0A_{-n+1/2}^{\pm i}(\tilde{\mathbf{L}}_{\mathcal{A}}) \oplus {}_0A_{n-1/2}^{\mp i}(\tilde{\mathbf{L}}_{\mathcal{A}}), \end{aligned} \quad (4.26)$$

connected by time reversal symmetry, meaning that band splitting does not occur. The same happens for two-dimensional IRs ${}_kE_0(\tilde{\mathbf{L}}_{\mathcal{A}})$ and ${}_kE_n(\tilde{\mathbf{L}}_{\mathcal{A}})$, since their

²Spin splitting is not allowed, since symmetry of \mathcal{A} nanotube is described by the fourth family line groups (4.17) (see also Chapter 2.3).

Clebsch-Gordan series are the following

$$\begin{aligned} &{}_kE_{\frac{1}{2}}(\tilde{\mathbf{L}}_{\mathcal{A}}) \oplus {}_kE_{-\frac{1}{2}}(\tilde{\mathbf{L}}_{\mathcal{A}}), \\ &{}_kE_{-n+\frac{1}{2}}(\tilde{\mathbf{L}}_{\mathcal{A}}) \oplus {}_kE_{n-\frac{1}{2}}(\tilde{\mathbf{L}}_{\mathcal{A}}). \end{aligned} \quad (4.27)$$

Finally, band splitting is not present for an IR $\frac{\pi}{a}E_0(\tilde{\mathbf{L}}_{\mathcal{A}})$, since $\frac{\pi}{a}E_0(\tilde{\mathbf{L}}_{\mathcal{A}}) \otimes u(\tilde{\mathbf{L}}_{\mathcal{A}}) = 2\frac{\pi}{a}E_{\frac{1}{2}}(\tilde{\mathbf{L}}_{\mathcal{A}})$.

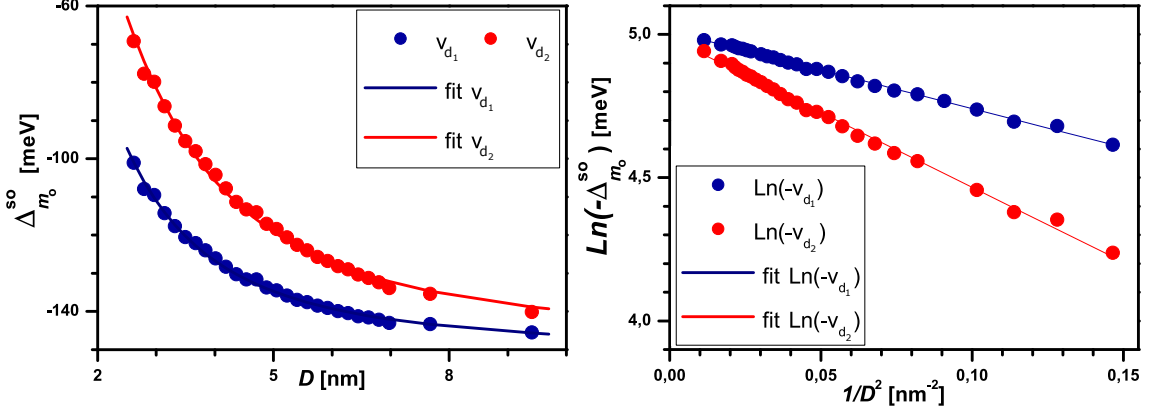


Figure 4.9: (left panel) Bands splitting dependance at $ka \approx 2\pi/3$ on the diameter D for \mathcal{A} bands v_{d_1} and v_{d_2} . (right panel) Logarithmic dependance of v_{d_1} and v_{d_2} band splittings on $1/D^2$.

We now turn to the numerical study of the band splitting values and investigate splitting of the bands v_d , v_{d_1} and v_{d_2} at the position of v_d band maximum. Symmetry labels of these bands are ${}_kE_n(\tilde{\mathbf{L}}_{\mathcal{A}})$, ${}_kE_{n-1}(\tilde{\mathbf{L}}_{\mathcal{A}})$ and ${}_kE_{n-2}(\tilde{\mathbf{L}}_{\mathcal{A}})$, respectively, meaning that v_d band does not split, while other two bands can be splitted due to SOC.

In Fig. 4.9 (left panel), dependance of $\Delta_{m_o}^{so}(k)$ on the diameter D (corresponding to the middle Mo wall) for v_{d_1} and v_{d_2} bands of the \mathcal{A} tube (n, n) ($n = 15, \dots, 40, 44, 54$) is studied. Negative values of band splittings mean that the energy of the branch with $m_o + 1/2$ is higher (but negative) than of the $m_o - 1/2$. It is clear from the graphs that curvature has negative impact on band splitting, since for both v_{d_1} and v_{d_2} bands absolute value of splitting increases with diameter. This behaviour is opposite to that observed in SWCNTs. In order to test the diameter limit, we fitted the v_{d_1} and v_{d_2} data. The best results are obtained for the exponential function of the form

$$y = a e^{\frac{b}{D^2} + \frac{c}{D^4}}, \quad (4.28)$$

which gave the following fitting parameters

$$\begin{aligned} a_{v_{d_1}} &= -151.117 \text{ meV}, b_{v_{d_1}} = -2.98031 \text{ nm}^2, c_{v_{d_1}} = 1.92611 \text{ nm}^4 \\ a_{v_{d_2}} &= -150.728 \text{ meV}, b_{v_{d_2}} = -6.30389 \text{ nm}^2, c_{v_{d_2}} = 7.50631 \text{ nm}^4. \end{aligned} \quad (4.29)$$

Thus, for tubes with large diameter value, v_{d_1} and v_{d_2} band splittings are approaching the layer K point spin splitting value. This is expected, since $\mathcal{A} ka = 2\pi/3$ point corresponds to the layer K point. Similar parameter values are obtained using the logarithmic fit (see Fig. 4.9 (right panel)), showing us dominant linear dependence of $\ln(-\Delta_{m_o}^{so})$ on $1/D^2$.

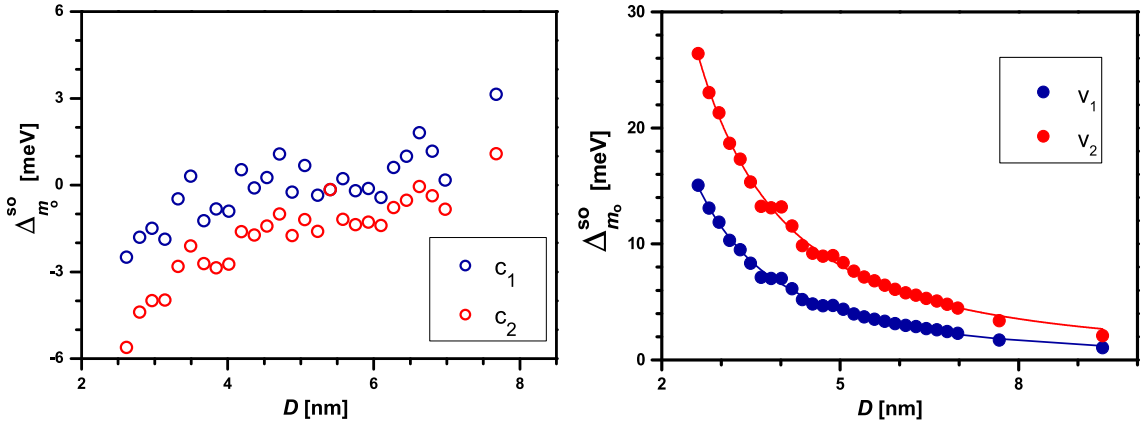


Figure 4.10: Diameter dependance of the magnitude of band splitting in the \mathcal{A} case for: (left panel) c_1 and c_2 bands; (right panel) v_1 and v_2 bands.

The same symmetry based analysis can be performed for the three lowest conductance bands c , c_1 and c_2 , as they are also assigned by IRs ${}_k E_n$, ${}_k E_{n-1}$ and ${}_k E_{n-2}$ of $\tilde{\mathcal{L}}_{\mathcal{A}}$, respectively. Thus, c band does not split, while two orbital bands c_1 and c_2 can have nonzero band splitting. In Fig. 4.10 (left panel), dependance of c_1 and c_2 band splitting $\Delta_{m_o}^{so}(k)$ versus tube diameter D in the vicinity of $ka = 2\pi/3$ is plotted. Our results show that c_1 and c_2 band splittings are much less influenced by the curvature topology of nanotubes than top valence bands. For the majority of tubes their values are of the same order of magnitude as the conductance band splitting of the monolayer, i.e. 3 meV, but it can be even smaller. Diameter dependance is not so sharply pronounced as in the valence bands due to the fact that orbital conductance bands are much denser, leading to the greater influence of neighbouring bands on the magnitude of band splitting.

Finally, we focus on the $k = 0$ point, where the global maximum of valence bands is placed. Highest orbital bands v , v_1 and v_2 in this point are labeled with IRs A_0^+ , A_1^+ and A_2^+ , respectively. Using the equations (4.24) and (4.27), we again conclude that valence band v does not split, while bands v_1 and v_2 are split into two branches. Diameter dependance of v_1 and v_2 band splittings is presented in Fig. (4.10) (right panel), showing us decreasing band splitting value with diameter increase. It is to be noted that due to zero splitting at the Γ point of MoS₂ layer's top valence band, we should expect for tubes that splitting at $k = 0$ tends to zero with further increase of the diameter D . Therefore, diameter dependance of the band splitting is fitted using the function

$$y = a(1 - \exp(-\frac{b}{D^2})), \quad (4.30)$$

giving us fitting parameters

$$\begin{aligned} a_{v_1} &= 132.687 \text{ meV}, b_{v_1} = 0.813153 \text{ nm}^2, \\ a_{v_2} &= 78.1499 \text{ meV}, b_{v_2} = 2.75225 \text{ nm}^2. \end{aligned} \quad (4.31)$$

4.2.2 Zig-zag tubes

Zig-zag nanotubes are direct band gap semiconductors [98–100], with minimum of conductance and maximum of valence bands placed at $k = 0$. Similarly as for indirect band gap of \mathcal{A} tubes, direct band gap varies from 1.10 eV for 2 nm diameter tubes to 1.15 eV for tubes with >9 nm diameter. In Fig. 4.11 band structure of zig-zag (15,0) nanotube is given. We will focus on top three valence (v , v_1 and v_2) and bottom three conductance (c , c_1 and c_2) bands.

Group of geometrical symmetries \mathbf{L}_Z belongs to the eighth family line groups, having one- and two-dimensional IRs. One-dimensional IRs $k_0 A/B_m^{\Pi_h}$ are present in the whole Brillouin zone, $k \in (-\pi/a, \pi/a]$, while m can take values 0 and n . Time-reversal symmetry θ connects $|km\Pi_v\rangle$ to $|-km\Pi_v\rangle$, thus giving symmetric bands $\mathcal{E}_m(k) = \mathcal{E}_m(-k)$. The same happens for two-dimensional IRs ${}_k E_m$, where $k \in (-\pi/a, \pi/a]$ and $m \in (0, n)$, meaning that it is enough to analyze only half of the Brillouin zone, i.e. $k \in (0, \pi/a]$.

Once the spin degree of freedom is included, the Clebsch-Gordan series of the product of orbital band IRs and spin representation $u(\tilde{\mathbf{L}}_Z)$ indicates the possibility

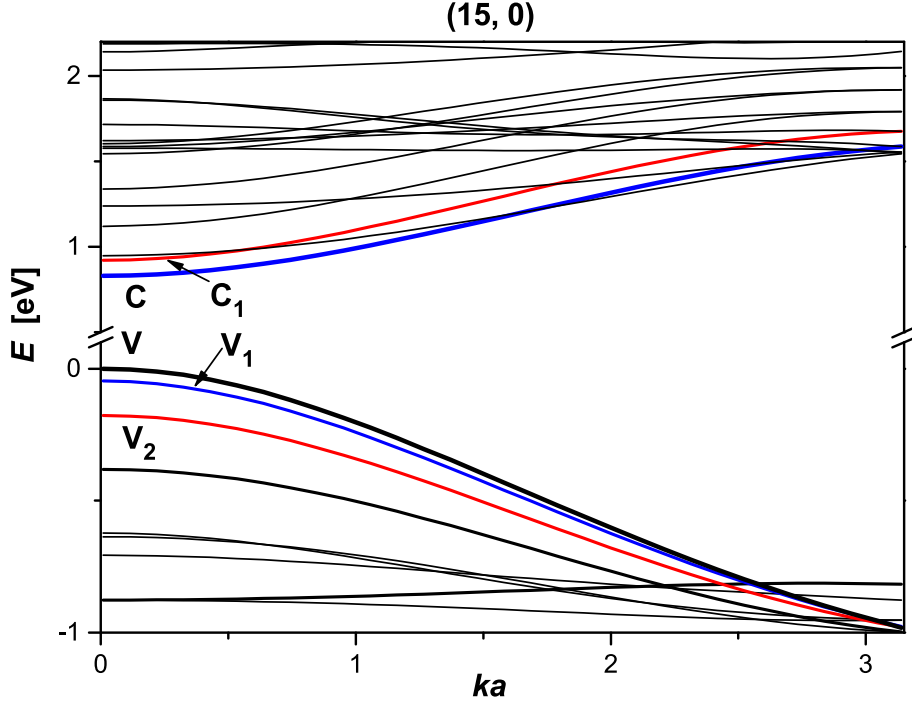


Figure 4.11: Electronic orbital bands of the zig-zag tube (15, 0).

of band splittings, along with the assignation of the branches

$$\begin{aligned}
{}_k A/B_0(\tilde{\mathbf{L}}_{\mathcal{Z}}) \otimes u(\tilde{\mathbf{L}}_{\mathcal{Z}}) &= {}_k E_{\frac{1}{2}}(\tilde{\mathbf{L}}_{\mathcal{Z}}), \\
{}_k A/B_n(\tilde{\mathbf{L}}_{\mathcal{Z}}) \otimes u(\tilde{\mathbf{L}}_{\mathcal{Z}}) &= {}_k E_{n-\frac{1}{2}}(\tilde{\mathbf{L}}_{\mathcal{Z}}), \\
{}_k E_{m_o}(\tilde{\mathbf{L}}_{\mathcal{Z}}) \otimes u(\tilde{\mathbf{L}}_{\mathcal{Z}}) &= {}_k E_{m_o+\frac{1}{2}}(\tilde{\mathbf{L}}_{\mathcal{Z}}) \oplus {}_k E_{m_o-\frac{1}{2}}(\tilde{\mathbf{L}}_{\mathcal{Z}}).
\end{aligned} \tag{4.32}$$

In the orbital picture, v band is assigned by one-dimensional IR ${}_k A_0$. When SOC is included, from (4.32) it follows that to this band corresponds DLG IR ${}_k E_{\frac{1}{2}}(\tilde{\mathbf{L}}_{\mathcal{Z}})$. Thus, no band splitting arises. On the other hand, both orbital bands v_1 and v_2 , assigned by ${}_k E_1(\tilde{\mathbf{L}}_{\mathcal{Z}})$ and ${}_k E_2(\tilde{\mathbf{L}}_{\mathcal{Z}})$, respectively, split due to SOC³.

In Fig. 4.12, diameter dependance of v_1 and v_2 band splitting $\Delta_{m_o}^{\text{so}} = \Delta_{m_o}^{\text{so}}(0)$ is plotted for $n = 15, \dots, 40, 44, 54$ tubes. The fits are done using the function of the form (4.30), due to the expected zero limit of band splitting for large diameter

³Since symmetry of the \mathcal{Z} nanotube is described by the fourth family line groups (4.18), spin splitting is forbidden (see Chapter 2.3).

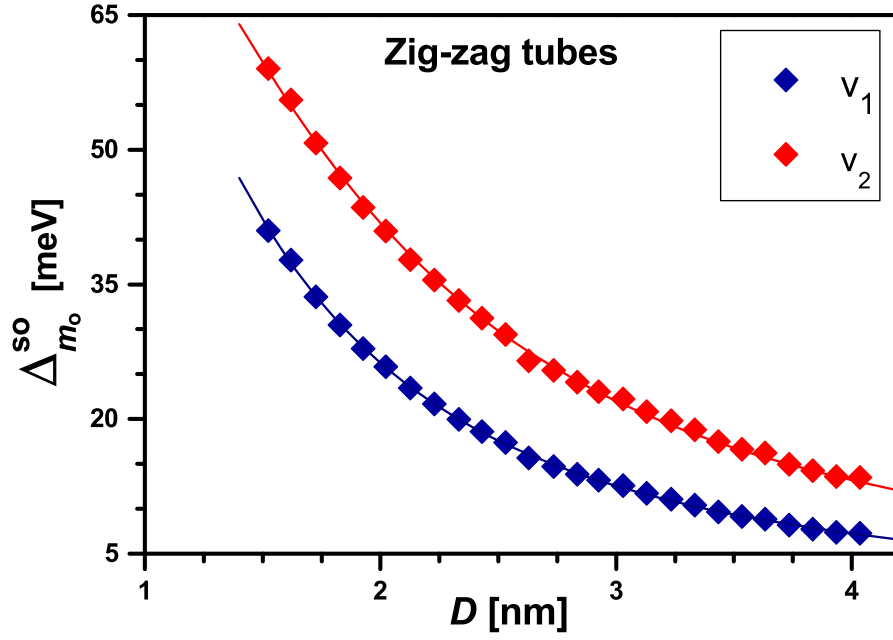


Figure 4.12: Dependence of valence v_1 and v_2 band splittings with respect to the diameter D in the zig-zag case.

tubes. Fitting parameters obtained for the two valence bands are

$$\begin{aligned} a_{v_1} &= 109.069 \text{ meV}, b_{v_1} = 1.09957 \text{ nm}^2, \\ a_{v_2} &= 86.3436 \text{ meV}, b_{v_2} = 2.64822 \text{ nm}^2. \end{aligned} \quad (4.33)$$

Finally, we study band splitting of the conductance bands c , c_1 and c_2 at $k = 0$. For tubes with $n = 0 \pmod{3}$ orbital band c has angular momentum $m_o = 2n/3$. If we recall that the monolayer has a conductance band minimum at the K point, similarly as in SWCNTs, zone folding can be used to explain this result. Relaxation obviously did not significantly change the conductance band spectra near $k = 0$, as c can be associated with the line, i.e. the cutting of the layer conductance band biorthogonal to \mathbf{c} and passing through the K point. Tubes with $n = 1 \pmod{3}$ and $n = 2 \pmod{3}$ may have $m_o = [2n/3] + 1$ or $m_o = [2n/3] + 2$ as angular momentum of the band c (there is some irregularity with the increase of diameter). Orbital bands c_1 and c_2 have angular momenta differing from m_o of c band by ± 1 . Thus, according to the equation (4.32), SOC induces splitting in all mentioned cases. We have grouped the results in three parts, according to the value p (here $p = n \pmod{3}$). The results are shown in Fig. 4.13. For tubes with smaller diameters,

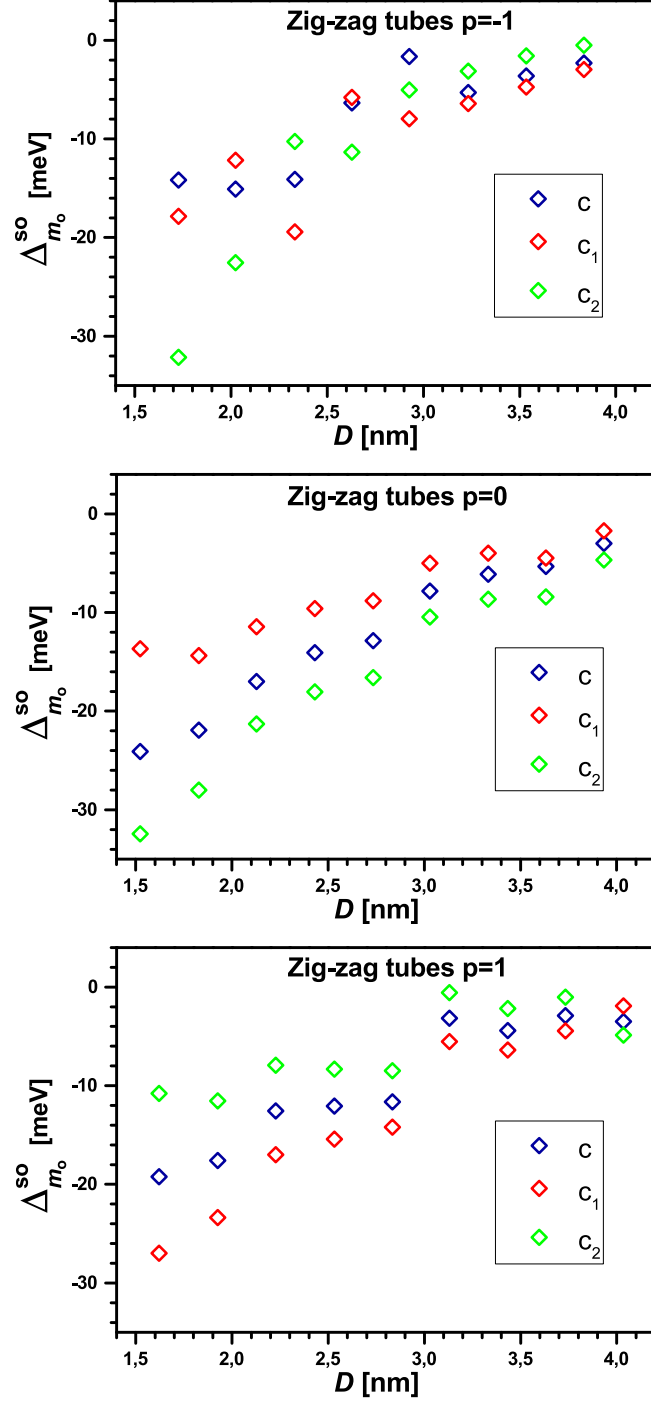


Figure 4.13: Dependence of zig-zag c , c_1 and c_2 conductance band splittings with respect to the tube's diameter D : tubes are sorted into three groups by $p = n \pmod{3}$; each graph is for the marked value of $p = -1, 0, 1$.

SOC has significant (up to an order of magnitude) increase of the absolute value of band splitting. The results also show good agreement with monolayer as D increases: for tubes with $p = 0$ the splitting tends to 3 meV, while for $p = \pm 1$ it falls to 1 meV.

4.2.3 Chiral tubes

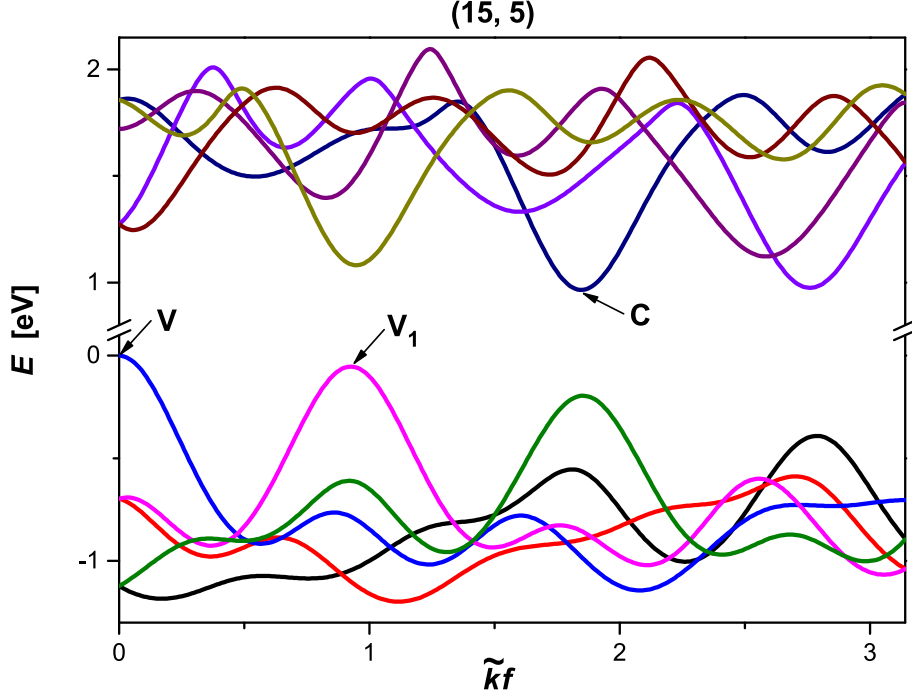


Figure 4.14: Electronic orbital bands of the chiral (15, 5) nanotube.

Among chiral nanotubes, most of them are direct band gap semiconductors, although small number of indirect band gap semiconductors is present. In Fig. 4.14 band structure of the chiral (15, 5) nanotube is given. We will focus on three bands v , v_1 and c , presented in Fig. 4.14, corresponding to top two valence bands and bottom conductance band, respectively. Chiral MoS_2 tubes are described by the first family line groups (4.16), having one-dimensional IRs $\tilde{k}A_{\tilde{m}}$ ($\tilde{k} \in (-\pi/f, \pi/f]$ and $\tilde{m} \in (-n/2, n/2]$) in helical QNs and kA_m ($k \in (-\pi/a, \pi/a]$ and $m \in (-q/2, q/2]$) in linear QNs. Orbital bands are assigned by the integer $\tilde{m}_o(m_o)$ value of helical/linear

momenta. Inclusion of SOC can induce spin splitting of the bands ⁴

$$\tilde{k}A_{\tilde{m}_o}(\tilde{\mathbf{L}}_C) \otimes u(\tilde{\mathbf{L}}_C) = \tilde{k} + \frac{\pi}{Q_f} A_{\tilde{m}_o + \frac{1}{2}}(\tilde{\mathbf{L}}_C) \oplus \tilde{k} - \frac{\pi}{Q_f} A_{\tilde{m}_o - \frac{1}{2}}(\tilde{\mathbf{L}}_C), \quad (4.34)$$

$$_k A_{m_o}(\tilde{\mathbf{L}}_C) \otimes u(\tilde{\mathbf{L}}_C) = {}_k A_{m_o + \frac{1}{2}}(\tilde{\mathbf{L}}_C) \oplus {}_k A_{m_o - \frac{1}{2}}(\tilde{\mathbf{L}}_C). \quad (4.35)$$

In this case, time reversal symmetry connects vectors of the form $|\bar{k}\bar{m}\rangle$ and $|- \bar{k} - \bar{m}\rangle$, belonging to IRs with opposite angular QNs. Due to the time reversal symmetry, it is enough to consider half of the irreducible Brillouin zone, since for each energy band point with negative QN $-\bar{k}$ and arbitrary QN \bar{m} there is a band point \bar{k} labeled by $-\bar{m}$, having the same energy.

In helical QNs, for each \mathcal{C} MoS₂ nanotube, maximum of orbital band v is placed at $\tilde{k} = 0$. Furthermore, its angular momentum QN is $\tilde{m}_0 = 0$. According to (4.34), IR $\tilde{k}A_0(\tilde{\mathbf{L}}_C)$ at $\tilde{k} = 0$ breaks into two due to SOC

$$\tilde{k}A_0(\tilde{\mathbf{L}}_C) \otimes u(\tilde{\mathbf{L}}_C) = \tilde{k} + \frac{\pi}{Q_f} A_{\frac{1}{2}}(\tilde{\mathbf{L}}_C) \oplus \tilde{k} - \frac{\pi}{Q_f} A_{-\frac{1}{2}}(\tilde{\mathbf{L}}_C). \quad (4.36)$$

However, since time reversal symmetry operator θ connects these two IRs for $\tilde{k} = 0$

$$\frac{\pi}{Q_f} A_{\frac{1}{2}}(\tilde{\mathbf{L}}_C) \rightarrow -\frac{\pi}{Q_f} A_{-\frac{1}{2}}(\tilde{\mathbf{L}}_C), \quad (4.37)$$

we conclude that splitting at this point is zero.

On the other hand, maximum of valence band v_1 is placed at $\pm \tilde{k}_{v_1} \neq 0$ ($\tilde{k}_{v_1} > 0$), and can be described by two IRs: $\tilde{k}_{v_1} A_1(\tilde{\mathbf{L}}_C)$ and its time reversal pair $-\tilde{k}_{v_1} A_{-1}(\tilde{\mathbf{L}}_C)$. In this case, using the equation (4.34) and time reversal symmetry, we conclude that splitting is allowed. Diameter dependance of v_1 band splitting can be fitted with formula (4.30). Fitting parameters in this case are

$$a_{v_1} = 116.191 \text{ meV}, b_{v_1} = 0.971421 \text{ nm}^2. \quad (4.38)$$

In Fig. 4.15 comparison between the fitting function for parameters (4.38) and calculated band splitting is given, showing an excellent agreement between them. It is interesting to mention that in \mathcal{C} SWCNTs dependance of valence/conductance band splitting was dependent on the diameter D ($1/D$ dependance), as well as on the chiral angle θ_c . (see (3.14)). In this case, pure diameter dependance of the valence band splitting is observed, showing insensitivity on chirality.

⁴Band splitting with removed spin degeneracy is allowed in systems described by the first family line group (see Chapter 2.3).

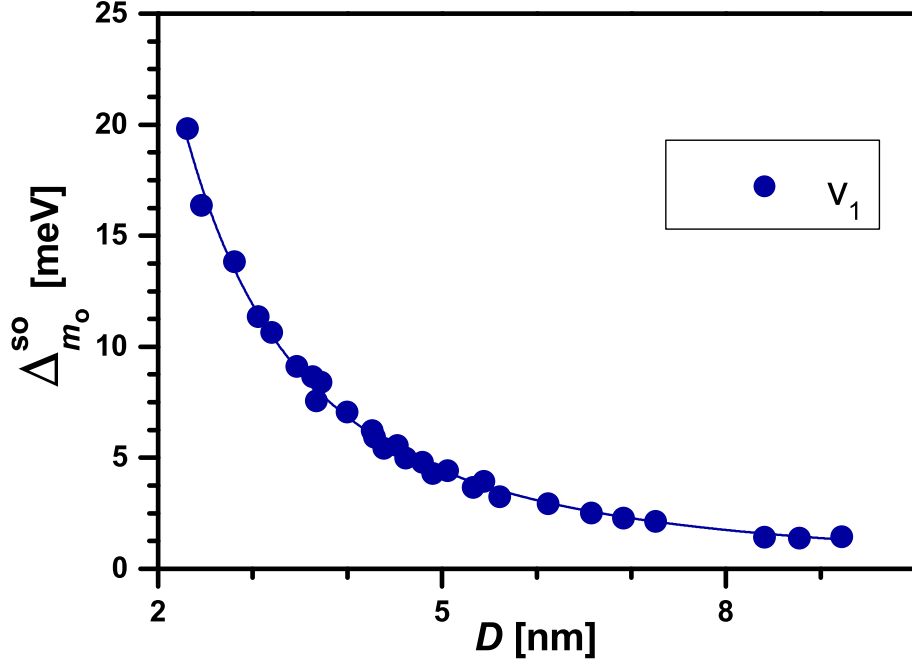


Figure 4.15: \mathcal{C} tubes: band splitting dependance of valence v_1 band maximum on the diameter D .

Finally, we study the conductance c band and its spin splitting. Minimum of c band is placed at $\tilde{k}_c \neq 0$ ($\tilde{k}_c > 0$), described by IRs $\tilde{k}_c A_{(n-2+n \bmod 2)/2}(\tilde{\mathbf{L}}_c)$ and $-\tilde{k}_c A_{(-n+2-n \bmod 2)/2}(\tilde{\mathbf{L}}_c)$. Presence of SOC induces splitting of the bands. In Fig. 4.16, dependance of splitting for conductance band c minimum with respect to the tube's diameter D is presented. In the left panel tubes $(4n, 3n)$ are studied, having fixed chiral angle $\theta_c \approx 0.44$, while in the right panel $(2n, n)$ tubes with chiral angle $\theta_c \approx 0.33$ are given. Figures show irregular dependance on D for fixed θ_c , regardless of the θ_c value. Thus, we are unable to make any general prediction, except to claim that values of splitting are relatively small.

4.3 Curvature effects on orbital contribution

Results presented in the previous Section suggest that curvature has notable effect on the magnitude of band splitting of valence bands, motivating us to analyze effects of curvature on OC in these bands.

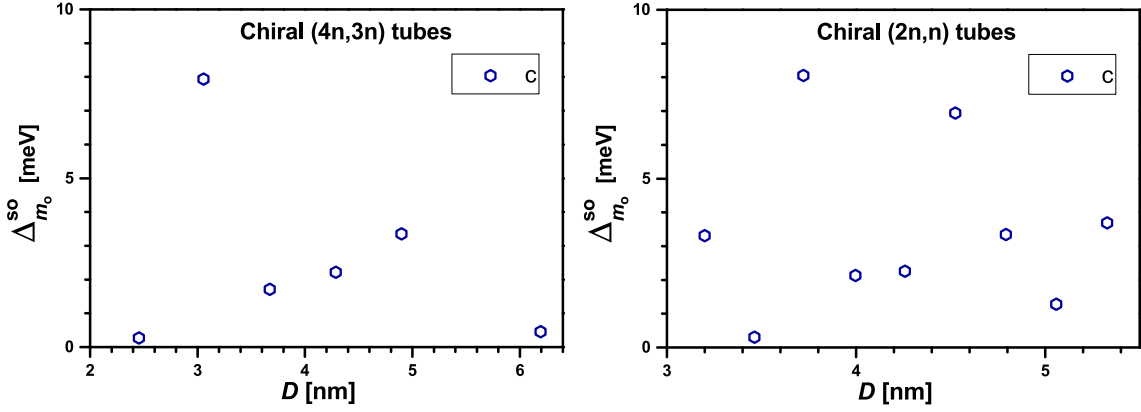


Figure 4.16: Dependence of splitting of the conductance band c minimum with respect to the tube's diameter D . In the left panel C tubes $(4n, 3n)$ are presented, while right panel shows splitting of $(2n, n)$ C MoS₂ tubes.

4.3.1 Armchair tubes

First, we analyze curvature effects on OC in valence v , v_1 and v_2 bands. To this end, in Fig. 4.17 and Fig. 4.18 OC for \mathcal{A} (15, 15) and (40, 40) tubes are given. In armchair tubes the valence v band does not split. This fact is manifested by equal weight of d_{m_l} and d_{-m_l} Mo orbitals ($m_l = 1, 2$), as well as p_1 and p_{-1} orbitals of both sulfur atoms. Metal $d_{\pm 2}$ orbitals are dominant along the whole Brillouin zone, with nontrivial contribution of orbitals $d_{\pm 1}$ and d_0 : for tube (15, 15) only slight variation of OC with the change of k is observable, while with the increase of diameter OC clearly changes. Also, for (15, 15) tube outer S orbitals have bigger OC than the inner sulfur. Their difference decreases for tubes with greater diameter, having equal OC in the layer limit. In the case of v_1 and v_2 bands, unequal contributions of Mo and S orbitals with opposite atomic quantum number m_l is present. This is clearly depicted in Fig. 4.17 and Fig. 4.18, additionally implying that curvature decreases OC difference of orbitals with opposite m_l , reaching the OC in the v band of MoS₂ monolayer. In the $k = 0$ point, dependance of v_1 and v_2 band splitting was studied in Chapter 4.2.1 (see also Fig. (4.10) (right panel)). From OC analysis it is evident that nonzero values of band splitting are present due to unequal contribution of orbitals with opposite m_l , while the dominant influence is of Mo d_2 and d_{-2} orbitals.

Next, we focus on the direct valence v_d , v_{d_1} and v_{d_2} bands. For these bands, OC of (15, 15) and (40, 40) tubes is given in Fig. 4.19 and Fig. 4.20. Band v_d does not split, which is again manifested by the equal OC of atomic orbitals with opposite

m_l . Around $ka \approx 2\pi/3$, where band splitting values were analyzed (see Fig. 4.9), dominant orbital is d_0 . Orbitals $d_{\pm 1}$ ($d_{\pm 2}$) have roughly twice (four times) smaller contribution than d_0 . Bands v_{d_1} and v_{d_2} have slightly unequal contribution of atomic orbitals with $\pm m_l$, although their difference decreases with diameter rise. For small diameter tubes outer S orbitals have bigger OC than inner; this difference decreases with diameter increase. At $ka \approx 2\pi/3$, all three S orbitals have nonzero contribution, although it is much smaller when compared to metal d orbitals.

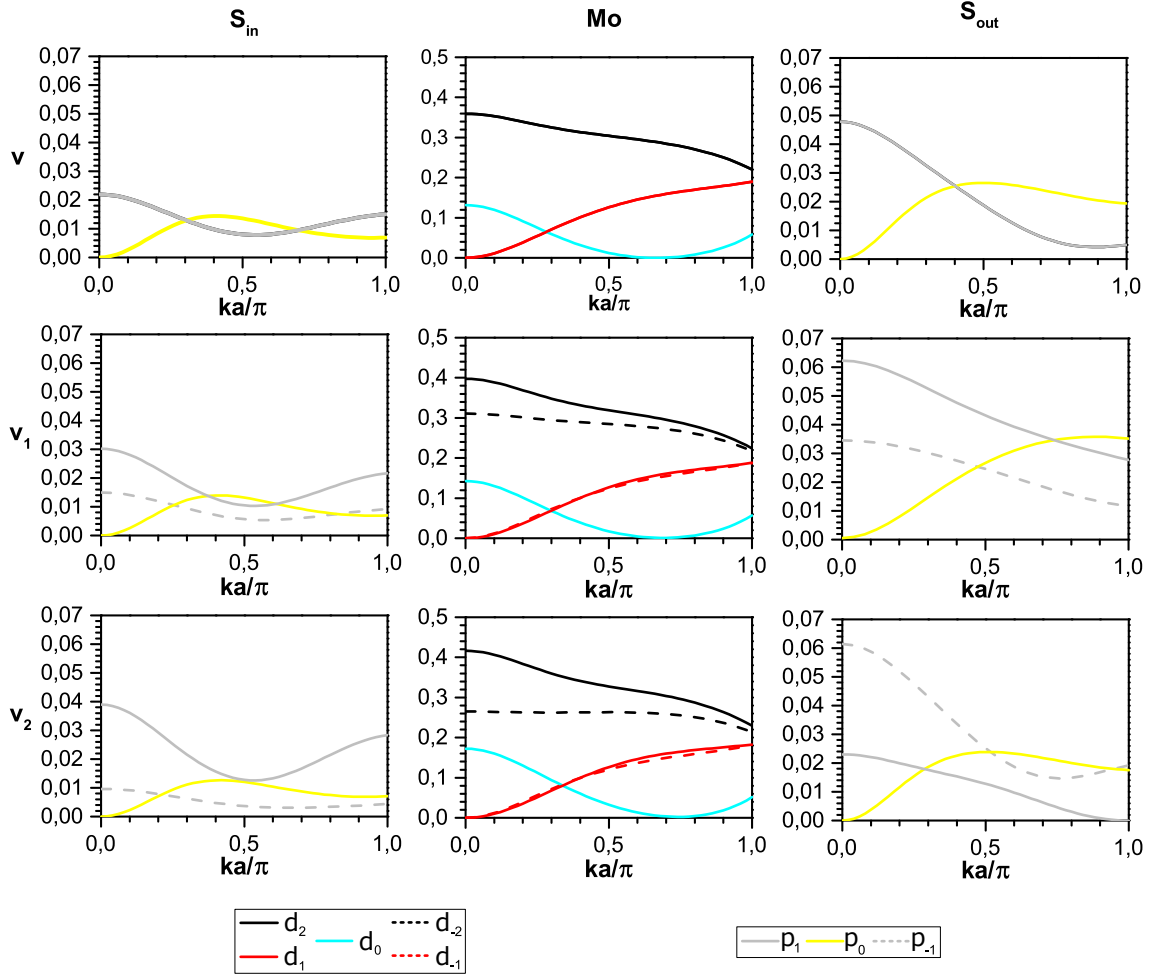


Figure 4.17: OC in valence v (first row), v_1 (second row) and v_2 (third row) bands of (15, 15) nanotube for the orbit representatives Mo , S_{in} and S_{out} . Only contributions of atomic orbitals relevant for the SOC effect are plotted.

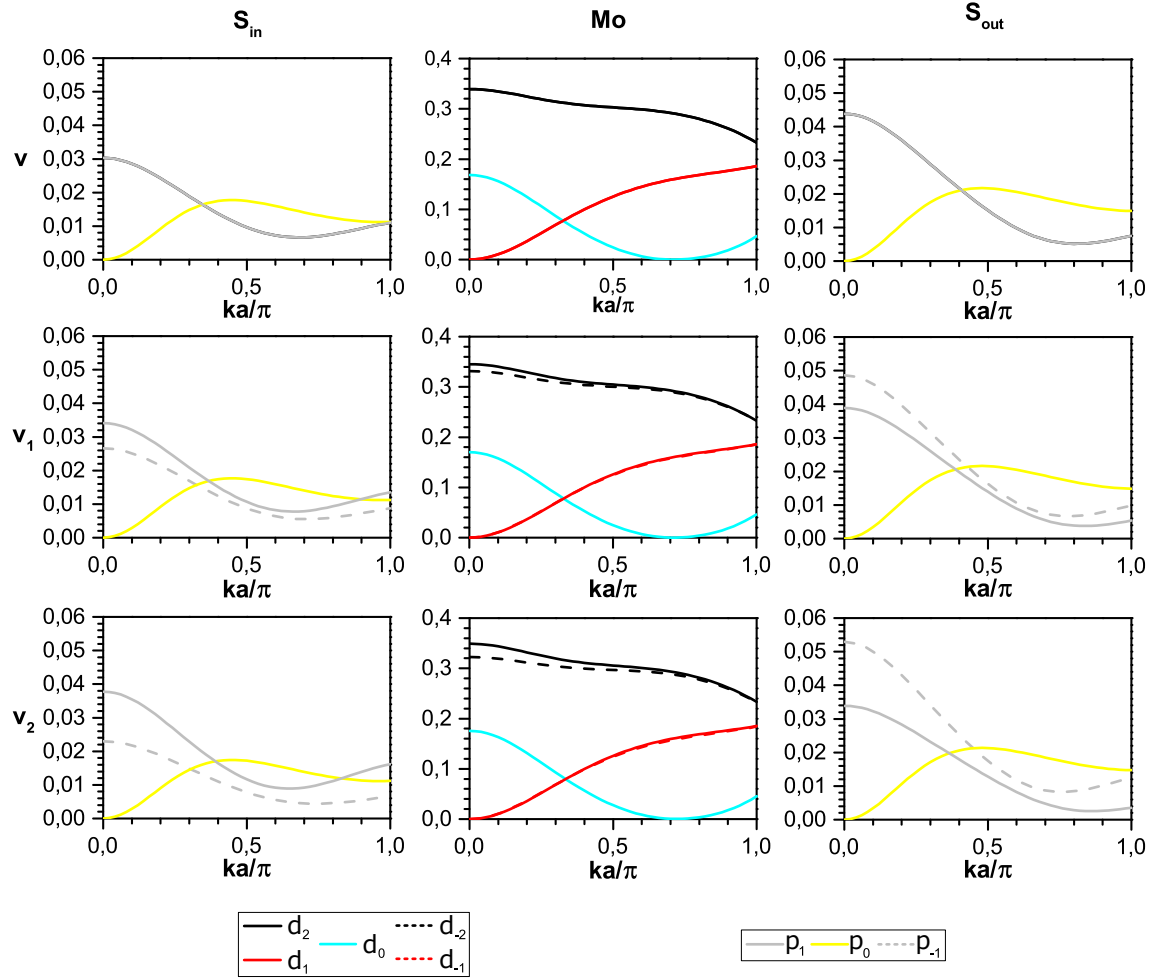


Figure 4.18: OC in valence v (first row), v_1 (second row) and v_2 (third row) bands of (40, 40) nanotube for the orbit representatives Mo , S_{in} and S_{out} . Only contributions of atomic orbitals relevant for the SOC effect are plotted.

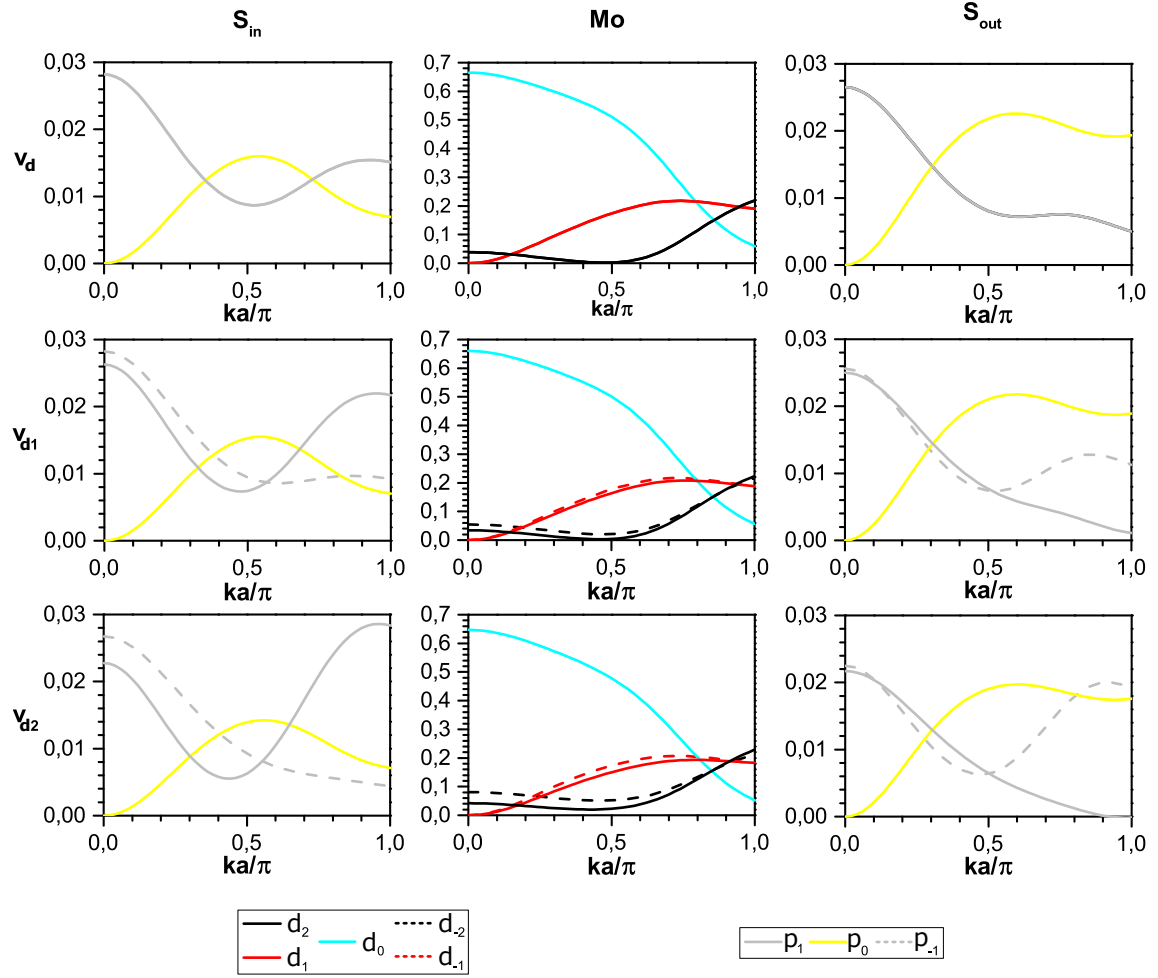


Figure 4.19: OC in direct valence v_d (first row), v_{d1} (second row) and v_{d2} (third row) bands of (15, 15) nanotube for the orbit representatives Mo , S_{in} and S_{out} . Only contributions of atomic orbitals relevant for the SOC effect are plotted.

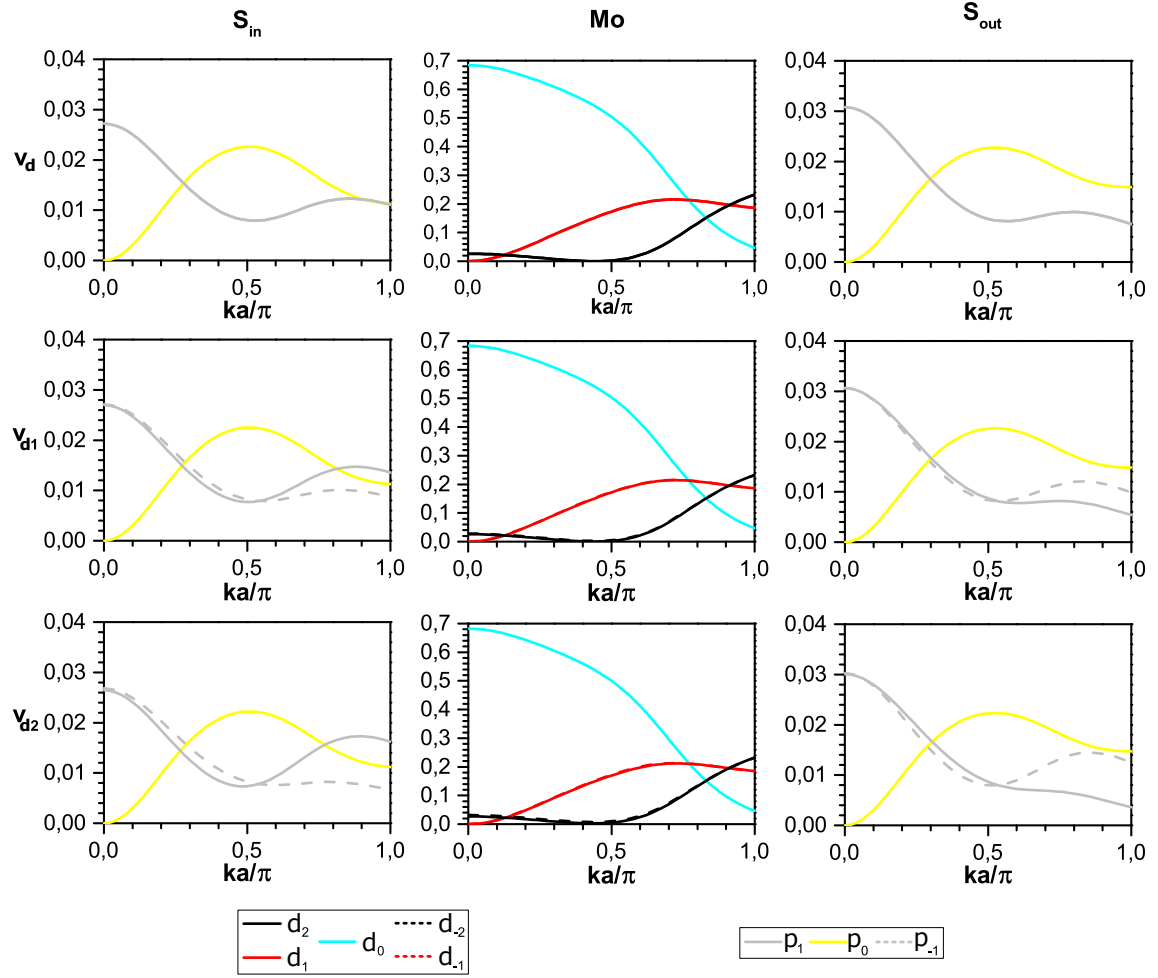


Figure 4.20: OC in direct valence v_d (first row), v_{d_1} (second row) and v_{d_2} (third row) bands of (40, 40) nanotube for the orbit representatives Mo, S_{in} and S_{out} . Only contributions of atomic orbitals relevant for the SOC effect are plotted.

4.3.2 Zig-zag tubes

Next, we analyse the valence bands v , v_1 and v_2 OC. In Fig. 4.21 and Fig. 4.22 OC for \mathcal{Z} (15,0) and (50,0) tubes are shown. Similarly as for armchair tubes, absence of band splitting of the v band is manifested in equal OC of atomic orbitals with opposite m_l . For (15,0) tube: dominant contribution is of $d_{\pm 2}$ orbitals ($\approx 30\%$), while OC of d_0 orbital varies from $\approx 20\%$ to $\approx 25\%$, depending on the point in the Brillouin zone. Orbitals $d_{\pm 1}$ have negligible influence $< 3\%$, less or comparable with OC of S orbitals. In the case of (50,0) tube, OC of $d_{\pm 2}$ orbitals shows slight increase, OC of d_0 orbital slightly decreases, while contribution of $d_{\pm 1}$ orbitals is almost zero. With diameter increase OC of inner sulfur orbitals approaches the OC of outer ones, as it was observed in armchair tubes.

Similarly as in valence bands of \mathcal{A} tubes, nonzero values of v_1 and v_2 bands are consequence of nonequal OC of orbitals with opposite m_l . This difference is most pronounced in $k = 0$. Diameter increase leads to decrease of $\pm m_l$ difference, approaching the limit of zero band splitting in the layer case. It is to be mentioned that OCs in both \mathcal{A} and \mathcal{Z} valence bands are similar in the large diameter limit: $d_{\pm 2}$ metal orbitals contribute with $\approx 70\%$, d_0 with $\approx 15\%$, while inner and outer sulfur $p_{\pm 1}$ atomic orbitals contribute with $\approx 15\%$.

4.3.3 Chiral tubes

Finally, we analyze valence bands of \mathcal{C} tubes. As v band has $m_o = 0$, the two branches $m = \pm 1/2$ touch at $k = 0$, i.e. though the band splits due to SOC, at this point spin degeneracy is not removed. The second band v_1 (having $m_o = -1$) splits at this point, but each branch crosses with the corresponding branch of the orbital band with $m_o = 1$ and again eigenvalues of H at $k = 0$ are spin degenerate. As explained, this is the direct consequence of time reversal symmetry.

In Fig. 4.23 (left panel) electronic bands of the tube (20,5) near the Fermi level are plotted for both H_o and H . Valence orbital band v (magenta) and the next nearest band v_1 have orbital QNs $m_o = 0$ and $m_o = -1$, respectively. Both of them split due to SOC. However, at $k = 0$ the two branches of v (which have $m = \pm 1/2$) touch, thus at this point the splitting is zero and spin degeneracy remains. As for v_1 , it has nonzero splitting at $k = 0$, though each of its branches (having $m = -1/2$ and $m = -3/2$) touch with the corresponding branch of the orbital band with $m_o = 1$,

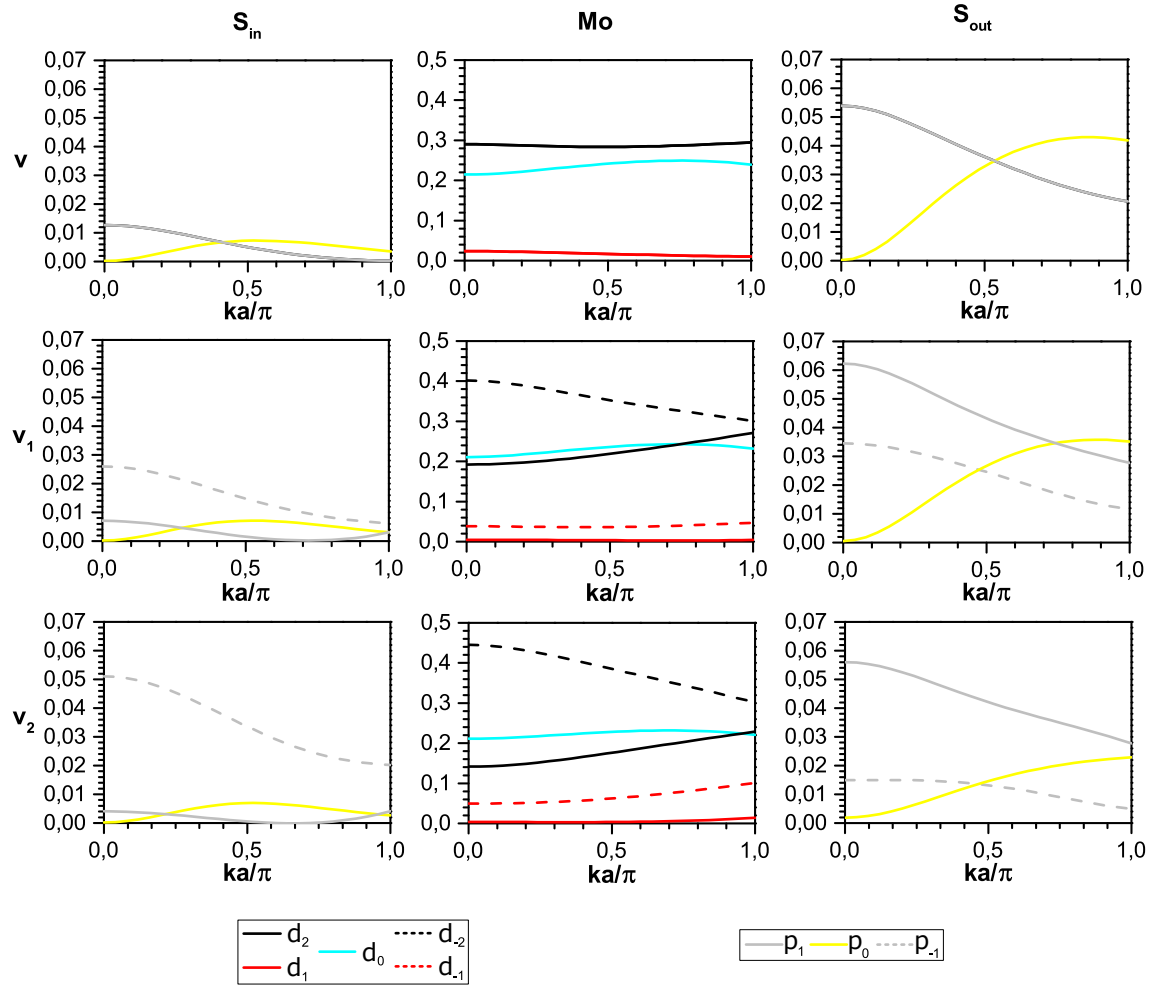


Figure 4.21: OC in valence v (first row), v_1 (second row) and v_2 (third row) bands of (15,0) nanotube for the orbit representatives Mo , S_{in} and S_{out} . Only contributions of atomic orbitals relevant for SOC effects are plotted.

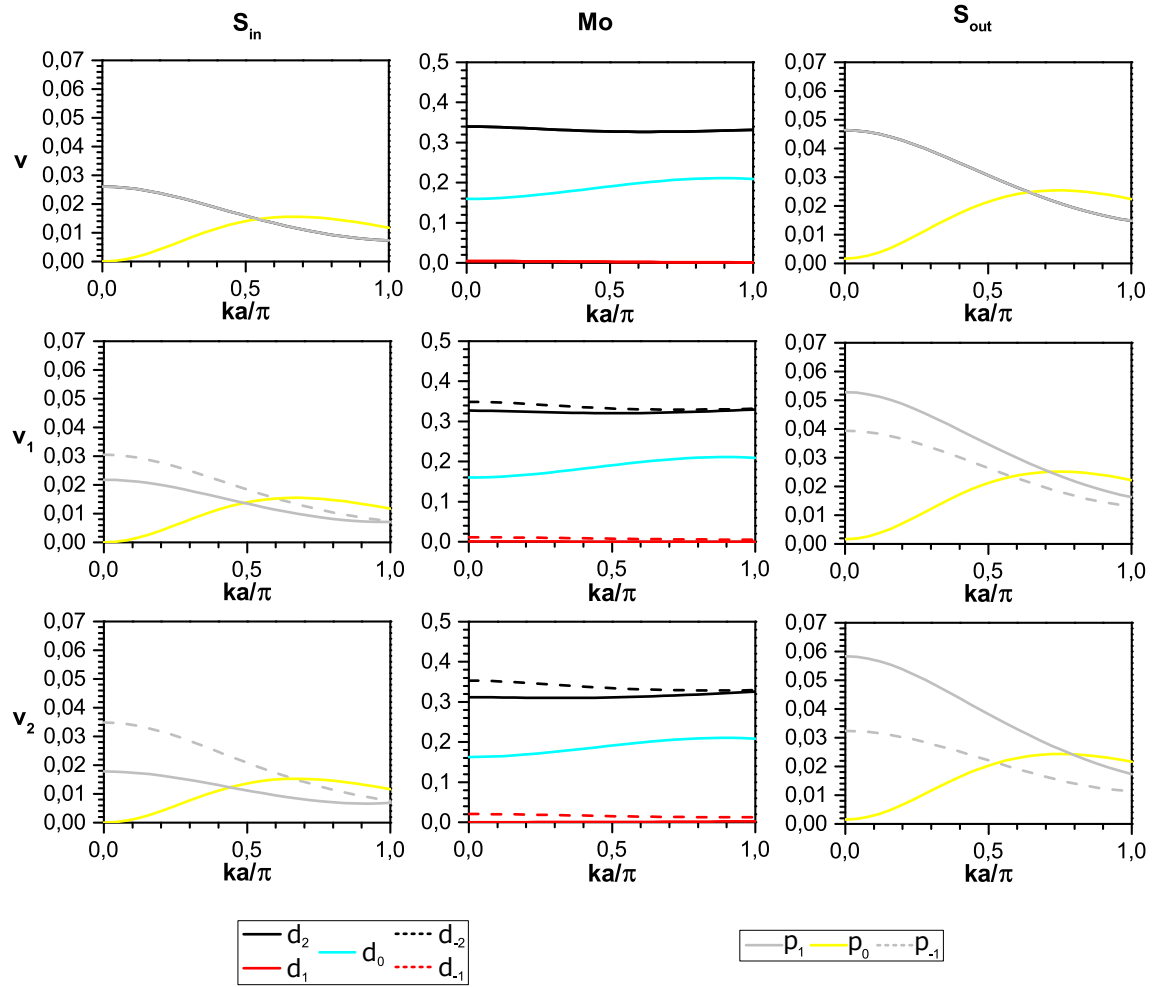


Figure 4.22: OC in valence v (first row), v_1 (second row) and v_2 (third row) bands of (50,0) nanotube for the orbit representatives Mo , S_{in} and S_{out} . Only contributions of atomic orbitals relevant for the SOC effect are plotted.

i.e. at $k = 0$ spin degeneracy is not removed (see right panel of Fig. 4.23).

In Fig. 4.24 OCs in these two valence bands are given. For the v band, in $k = 0$ OC of orbitals with opposite m_l is equal. However, in other points of the Brillouin zone, nonequal contributions of orbitals with $\pm m_l$ gives rise to nonzero band splitting. The biggest (5%) difference is between $d_{\pm 1}$ orbitals at $k = \pi/a$. In case of the v_1 band, band splitting is allowed at $k = 0$. Large difference between d_2 and d_{-2} contribution at $k = 0$ is the most responsible for the observed large splitting. Additionally, weak contribution of $d_{\pm 1}$ metal orbitals is present due to their $\approx 2\%$ difference. Also, contribution of $p_{\pm 1}$ orbitals of the $S_{\text{in}}/S_{\text{out}}$ atom differs by 1.5%/3%. Generally, unequal contribution of $\pm m_l$ orbitals contributes to band splitting along the Brillouin zone.

Finally, for large diameter tubes, OC in valence bands at $k = 0$ corresponds to OCs of \mathcal{A} and \mathcal{Z} tubes, additionally resembling the zero splitting of MoS_2 monolayer at the Γ point.

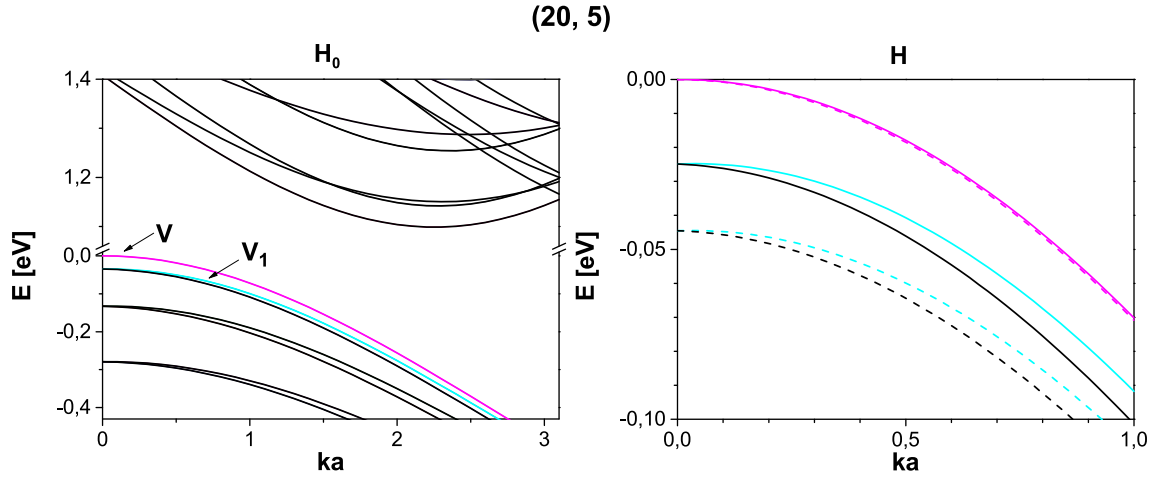


Figure 4.23: (left panel) Electronic bands in linear QNs around the Fermi level of the \mathcal{C} (20, 5) nanotube. Valence v band (magenta) is labeled with QN $m_o = 0$, while v_1 band (cyan) has QN $m_o = -1$. (right panel) Influence of SOC on orbital valence v and v_1 bands. Orbital v band splits into two branches, labeled with QNs $m = 1/2$ (magenta) and $m = -1/2$ (magenta dashed). The same happens with v_1 band, which is splitted into two branches with QNs $m = -1/2$ (cyan) and $m = -3/2$ (cyan dashed). Although the band v_1 splits, spin degeneracy at $k = 0$ is not removed, due to the fact that both branches, due to time reversal symmetry, coincide with branches which originate from QN $m_o = 1$ labeled orbital band.

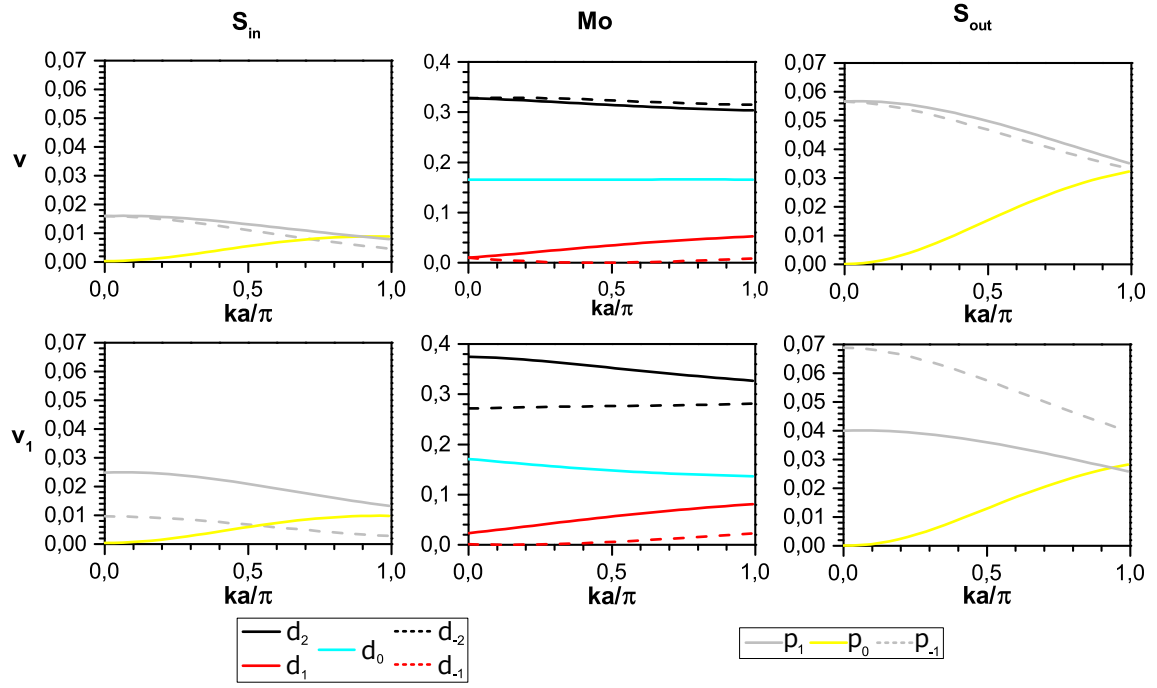


Figure 4.24: OC in valence v (first row) and v_1 (second row) bands of $(20,5)$ nanotube for the orbit representatives Mo , S_{in} and S_{out} . Only contributions of atomic orbitals relevant for the SOC effect are plotted.

Conclusions

In this dissertation SOC effects in low dimensional systems are studied with the help of group theoretical analysis. When spin degree of freedom is taken into account, double covering of system's geometrical symmetry group has to be used, making the construction of these double groups a necessary first step. Geometrical symmetries of Q1D systems belong to one of 13 infinite families of line groups L . Thus, the initial task was to determine the structure of DLGs and to construct their IRs, necessary in the symmetry based study of electron dynamics. Application of DLGs introduces some differences in the assignation of energy bands (in comparison with pure orbital bands) by conserved QNs: half integer QNs of linear/helical angular momentum (orbital bands are labeled by integer values of angular momentum solely) and imaginary parity values ($\pm i$), instead of ± 1 parity labels of orbital bands.

First question that can be solved on the purely group theoretical background is whether SOC may remove spin degeneracy of the orbital bands. This is done by analyzing the Clebsch-Gordan series of tensor product of orbital IRs and spin representation. If the resulting tensor product gives only one double group IR of doubled dimension (as compared to the dimension of an orbital IR), band splitting is forbidden. On the other hand, appearance of two double group IRs of the same dimension indicates band splitting unless the two IRs are *-conjugated by time reversal symmetry. If the band splitting is present, the final goal is to check whether band splitting is followed by the removal of spin degeneracy, i.e. if spin splitting appears. It has been shown that if vertical mirror or glide planes are geometrical symmetries of the system, there is no spin splitting. This happens for systems whose symmetry is described by DLG of the families 6-13. However, if the total Hamiltonian commutes with time reversal symmetry θ , combination of horizontal mirror plane or roto-reflections with θ forbids spin polarization of the bands. Thus, if the system possesses time reversal symmetry, only groups from the first or fifth

family allow spin degeneracy of the bands to be lifted.

As for Q2D systems, their geometrical symmetries are from one of the eighty diperiodic groups. The construction of their double groups can be performed in a similar fashion as for the line groups. Here, results relevant for transition-metal dichalcogenide monolayers are given, as in Chapter 4 SOC effects in MoS₂ monolayer and nanotubes are studied.

Finally, the derived double groups and their IRs allow calculations of electronic bands, with or without SOC term included in the total Hamiltonian; numerical part is performed with help of the POLSym code, based on modified group projector technique [25]. For concrete low dimensional systems studied in this thesis, spin independent Hamiltonian matrix elements were calculated within density functional tight binding method, while SOC is included within the atomic approximation.

SOC effects in SWCNTs, which are the most studied Q1D systems, have already been experimentally and theoretically studied. Besides obtaining the correct full symmetry based explanation for reported numerical results of band and spin splittings, the thesis addresses to discrepancy between these and experimentally measured values of spin splitting. DLG analysis of SWCNT bands justifies that diverse SOC effects on electronic band structure are direct consequence of their symmetry. Moreover, spin splitting, occurring only in chiral SWCNTs, results in spin polarization along the tube's axis. The obtained assignation of bands by conserved QNs makes obvious that spin splitting does not impose the overall spin polarization of the bands. Namely, intersection of an orbital band of H_o assigned by linear/helical angular momentum m_o and the one assigned by $m_o \pm 1$, results in rearrangement of the bands (after including the spin degree of freedom) in order to avoid the crossing of bands with identical QNs. This prevents the expected overall spin polarization of some branches of these two orbital bands.

Finally, the discrepancy between experimental and reported numerical results is addressed. The later predict one order of magnitude smaller value of conductance spin splitting than experimentally observed. Electronic properties of SWCNTs are known to be highly sensitive to applied strain, because influence of strain induced deformations has to be included in order to explain the experimental results for the electronic band gap. This sensitivity of electronic structure on tube's configuration motivated us to investigate the influence of small axial strain on the magnitude of spin splitting of valence and conductance bands. Our results show that even small

stretching can significantly increase spin splitting, thus suggesting that the presence of strain in the experimental setup can be responsible for the observed difference between two approaches.

Up to our knowledge, effects of SOC in MoS₂ nanotubes have not been analysed. On the other hand, MoS₂ layers are one of the best studied systems within the transition-metal dichalcogenide family. Symmetry group of chiral, armchair and zig-zag MoS₂ nanotubes are from the first, fourth, and eighth family DLGs, respectively [96]. Thus, according to the above results for spin splitting in Q1D systems, splitting may occur only in chiral tubes. Due to the mirror plane and time reversal symmetry, only band splitting is possible for armchair and zig-zag tubes: symmetry analysis singles out the orbital bands that does not split at all. Enhanced SOC effects in SWCNTs, as compared to graphene, are commonly explained as a consequence of their curvature and cylindrical topology. In order compare the results with the MoS₂ monolayer, using the constructed double group of the corresponding diperiodic MoS₂ monolayer group, and its IRs, symmetry based numerical analysis of SOC effects on band structure was performed.

It has been concluded that in armchair MoS₂ tubes curvature effects have negative impact on the band splitting at the point of a direct band gap ($ka \approx 2\pi/3$), while in the $k = 0$ point curvature has the opposite influence. This behaviour can be explained by the fact that $ka = 2\pi/3$ point corresponds to the layer's K point, where ~ 150 meV spin splitting value is present, while $k = 0$ point is, by the zone folding, related to the layer's Γ point with zero spin splitting. On the other hand, conductance band splitting at $ka \approx 2\pi/3$ point is weakly influenced by the curvature, with band splitting values of the same order of magnitude as in the monolayer case (few meV). In zig-zag nanotubes, curvature has positive effect on both conductance and valence band splitting. Spin splitting in conductance bands of chiral tubes is weakly influenced by the curvature, while in valence bands this effect is more pronounced.

Finally, it is to be mentioned that symmetry of armchair MoS₂ tubes allows breaking of horizontal mirror plane symmetry by means of electric field parallel to the tube's axis, thus inducing Rashba spin splitting of the bands. This property, although not discussed in this work, can be an interesting continuation of the presented study.

Appendix A

Irreducible representations of direct product of groups

If the group $\mathbf{G} = \mathbf{H} \otimes \mathbf{K}$ is a direct product of two groups \mathbf{H} and \mathbf{K} , whose sets of nonequivalent IRs are known

$$\{\Delta^{(\mu)}(\mathbf{H})|\mu = 1, \dots, p_H\}, \{d^{(\alpha)}(\mathbf{K})|\alpha = 1, \dots, p_K\}, \quad (\text{A.1})$$

complete set of nonequivalent IRs of the group \mathbf{G} is

$$\{\Delta^{(\mu\alpha)}(\mathbf{G}) := \Delta^{(\mu)}(\mathbf{H}) \otimes d^{(\alpha)}(\mathbf{K})|\mu = 1, \dots, p_H, \alpha = 1, \dots, p_K\}. \quad (\text{A.2})$$

Appendix B

Induction procedure

Induction is a method for finding group representations by using the representations of subgroups of the corresponding group [32].

Induced representation $D(\mathbf{G}) = \Delta(\mathbf{H}) \uparrow \mathbf{G}$ of the group \mathbf{G} from the representation $\Delta(\mathbf{H})$ of the subgroup \mathbf{H} with transversal $Z = \{z_1 = e, z_2, \dots, z_{|Z|}\}$ ($|Z| = |\mathbf{G}|/|\mathbf{H}|$) is joining the element $g \in \mathbf{G}$ with the representation

$$D(g) = \sum_{p=1}^{|Z|} E_p^{gp} \otimes \Delta(h(g, z_p)) = \sum_{p,q=1}^{|Z|} \sum_{h \in \mathbf{H}} \delta(z_p^{-1}gz_q, h) E_q^p \otimes \Delta(h), \quad (\text{B.1})$$

where E_p^q is $|Z|$ -dimensional matrix of the absolute basis, while $\delta(a, b)$ is Kronecker delta function.

A set of matrices $D(\mathbf{G}) = \Delta(\mathbf{H}) \uparrow \mathbf{G}$ is $|D| = |Z||\Delta|$ dimensional representation of the group \mathbf{G} . Their matrices consist of $|\Delta|$ -dimensional blocks. There is only one nonzero block in each row and each column of every matrix. Induced representation is independent on the choice of transversal, meaning that for another transversal one obtains equivalent representation.

On a set of classes of equivalent representations of the invariant subgroup \mathbf{H} , \mathbf{G} -conjugation defines group action: group element $g \in \mathbf{G}$ maps representation $\Delta(\mathbf{H})$ into g -conjugated representation

$$(g\Delta)(\mathbf{H}) = \Delta_g(\mathbf{H}) = \{\Delta_g(h) := \Delta(g^{-1}hg) | h \in \mathbf{H}\}. \quad (\text{B.2})$$

Subgroup \mathbf{H} is the invariant subgroup of each representations stabilizer. Representation $\Delta_g(\mathbf{H})$ is irreducible if and only if $\Delta(\mathbf{H})$ is irreducible, i.e. \mathbf{G} -conjugation defines an action into the set of subgroup's IRs.

Action in the set of nonequivalent IRs of the subgroup \mathbf{H} partitions this set into orbits $\mathbf{G}\mu$ with stabilisators \mathbf{G}_μ

$$\mathbf{G}\mu = O^{(\mu)} = \{\Delta^\nu | \exists g \in \mathbf{G}, \nu \sim g\mu\}, \text{ where } \Delta^{(g\mu)}(\mathbf{H}) := \Delta_g^{(\mu)}(\mathbf{H}), \quad (\text{B.3})$$

$$\mathbf{G}_\mu = L^{(\mu)} = \{g \in \mathbf{G} | g\mu \sim \mu\}. \quad (\text{B.4})$$

B.1 Induction from the invariant subgroup of index 2

In physically relevant situations it is often needed to construct IRs of the group \mathbf{G} by knowing the IRs of its halving subgroup \mathbf{H} : $\mathbf{G} = \mathbf{H} + g\mathbf{H}$. Small representations in this case can be only \mathbf{H} (corresponding orbits have two elements) or \mathbf{G} (orbit with one element).

If $\Delta^{(\mu)}(\mathbf{H})$ is IR of the subgroup \mathbf{H} , with small group \mathbf{H} and orbit $\{\Delta^{(\mu)}(\mathbf{H}), \Delta_s^{(\mu)}(\mathbf{H})\}$, induction procedure gives us IR of the group \mathbf{G} , i.e. representation $D^{(\mu)}(\mathbf{G}) = \Delta^{(\mu)}(\mathbf{H}) \uparrow \mathbf{G}$ with matrices ($h \in \mathbf{H}$)

$$D^{(\mu)}(h) = \begin{pmatrix} \Delta^{(\mu)}(h) & 0 \\ 0 & \Delta_s^{(\mu)}(h) \end{pmatrix}, D^{(\mu)}(sh) = \begin{pmatrix} 0 & \Delta^{(\mu)}(s^2)\Delta_s^{(\mu)}(h) \\ \Delta^{(\mu)}(h) & 0 \end{pmatrix}. \quad (\text{B.5})$$

In the second case, $L^{(\mu)} = \mathbf{G}$, $O^{(\mu)} = \{\Delta^{(\mu)}(\mathbf{H})\}$, operator Z that connects equivalent representations $\Delta^{(\mu)}(\mathbf{H})$ is defined and $\Delta_s^{(\mu)}(\mathbf{H})$

$$\forall h \in \mathbf{H}, \Delta_s^{(\mu)}(h) = Z^{-1}\Delta^{(\mu)}(h)Z. \quad (\text{B.6})$$

Operator Z satisfies the relation $Z^2 = \Delta^{(\mu)}(s^2)$, and the corresponding matrices of IRs are

$$D^{(\mu,\pm)}(h) = \Delta^{(\mu)}(h), D^{(\mu,\pm)}(sh) = \pm Z\Delta^{(\mu)}(h). \quad (\text{B.7})$$

B.2 Group is semidirect product of its subgroups

\mathbf{G} is semidirect product of its subgroups \mathbf{H} and \mathbf{K} [12, 33]. Furthermore, it is assumed that \mathbf{H} is Abelian subgroup, with one-dimensional IRs $\{\Delta^{(\mu)}(\mathbf{H})\}$.

Subgroup \mathbf{K}_μ of \mathbf{K} for each μ , is made of elements $\ell \in \mathbf{K}$ that satisfy

$$\Delta^{(\mu)}(\ell^{-1}h\ell) = Z^{-1}\Delta^{(\mu)}(h)Z, \quad (\text{B.8})$$

for all $h \in \mathbf{H}$ and fixed nonsingular Z .

Then, for each $\delta^{(\nu)}(\mathbf{K}_\mu)$ of the subgroup \mathbf{K}_μ , IR

$$\Gamma^{(\mu,\nu)}(hk_\mu) = \Delta^{(\mu)}(h) \otimes \delta^{(\nu)}(k_\mu), \quad (\text{B.9})$$

of the little group gives one induced IR of \mathbf{G}

$$\Gamma^{(\mu,\nu)}(\mathbf{G}) = \Gamma^{(\mu,\nu)}(\mathbf{H}\mathbf{K}_\mu) \uparrow \mathbf{G}. \quad (\text{B.10})$$

Appendix C

Tables of the IRs of DLGs

For each DLG family IRs are presented within a separate table with symbols of IRs (column 1), range of momenta QNs (column 2), and matrices corresponding to the generators listed in the first row. General symbol of an IR is $\bar{k}D_m^\Pi$, where D is A , E and G for 1-, 2- and 4-dimensional IRs; exceptionally, for 1-dimensional IRs of the groups with vertical mirror or glide plane, parity $\Pi_v = \pm 1, \pm i$ is traditionally signified by letters $D = A/B$. For the families with pure translational factor $\mathbf{T}_Q = \mathbf{T}$ linear QNs are listed; as the first and fifth family contain incommensurate groups, linear IRs are followed by the helical ones. Unit matrix of dimension d is $\mathbb{1}_d$, while:

$$\begin{aligned} K_2(k) &= \text{diag}(e^{ik}, e^{-ik}), & M_2(m) &= \text{diag}(e^{im\frac{2\pi}{n}}, e^{-im\frac{2\pi}{n}}), \\ K_4(k) &= K_2(k) \otimes \mathbb{1}_2, & A_4(k, m) &= K_2(k) \otimes M_2(m), \\ M_4(m) &= \mathbb{1}_2 \otimes M_2(m), & N &= \text{diag}(e^{im\frac{2\pi}{n}}, e^{-im\frac{2\pi}{n}}, e^{-im\frac{2\pi}{n}}, e^{im\frac{2\pi}{n}}). \end{aligned}$$

Table C.1: Irreducible representations of double line groups $\tilde{\mathbf{L}}^{(1)} = \tilde{\mathbf{T}}_Q(f)\tilde{\mathbf{C}}_n$. For rational $Q = q/r$ ($q > r$ coprimes) groups are commensurate with translational period $a = fq/n$, and both linear and helical QNs apply; otherwise only the helical QNs exist.

IR	(k, m)	$\widetilde{(C_Q f)}$	\tilde{C}_n
${}_k A_m$	$k \in (-\frac{\pi}{a}, \frac{\pi}{a}]$ $m \in (-\frac{q}{2}, \frac{q}{2}]$	$e^{ikf} e^{im\frac{2\pi}{Q}}$	$e^{im\frac{2\pi}{n}}$
$_{\tilde{k}} A_{\tilde{m}}$	$\tilde{k} \in (-\frac{\pi}{f}, \frac{\pi}{f}]$ $\tilde{m} \in (-\frac{n}{2}, \frac{n}{2}]$	$e^{i\tilde{k}f}$	$e^{i\tilde{m}\frac{2\pi}{n}}$

Table C.2: Irreducible representations of double line groups $\tilde{\mathbf{L}}^{(2)} = \tilde{\mathbf{L}}2\bar{n}, \tilde{\mathbf{L}}\bar{n} = \tilde{\mathbf{T}}(a)\tilde{\mathbf{S}}_{2n}$.

IR	(k, m)	$\widetilde{(\mathbf{1}_3 a)}$	\tilde{S}_{2n}
${}_k A_m^{\Pi_h}$	$k = 0, \frac{\pi}{a}$ $m \in (-\frac{n}{2}, \frac{n}{2}]$	e^{ika}	$e^{im\frac{\pi}{n}} \Pi_h$
${}_k E_m$	$k \in (0, \frac{\pi}{a})$ $m \in (-\frac{n}{2}, \frac{n}{2}]$	$K_2(ka)$	$\begin{bmatrix} 0 & \Pi_{\tilde{e}'} e^{im\frac{2\pi}{n}} \\ 1 & 0 \end{bmatrix}$

Table C.3: Irreducible representations of double line groups $\tilde{\mathbf{L}}^{(3)} = \tilde{\mathbf{L}}n/m, \tilde{\mathbf{L}}2\bar{n} = \tilde{\mathbf{T}}(a)\tilde{\mathbf{C}}_{nh}$.

IR	(k, m)	$\widetilde{(\mathbf{1}_3 a)}$	\tilde{C}_n	$\tilde{\sigma}_h$
${}_k A_m^{\Pi_h}$	$k = 0, \frac{\pi}{a}$ $m \in (-\frac{n}{2}, \frac{n}{2}]$	e^{ika}	$e^{im\frac{2\pi}{n}}$	Π_h
${}_k E_m$	$k \in (0, \frac{\pi}{a})$ $m \in (-\frac{n}{2}, \frac{n}{2}]$	$K_2(ka)$	$e^{im\frac{2\pi}{n}} \mathbf{1}_2$	$\begin{bmatrix} 0 & \Pi_{\tilde{e}'} \\ 1 & 0 \end{bmatrix}$

Table C.4: Irreducible representations of double line groups $\tilde{\mathbf{L}}^{(4)} = \tilde{\mathbf{L}}2n_n/m = \tilde{\mathbf{T}}_{2n}^1(\frac{a}{2})\tilde{\mathbf{C}}_{nh}$. Here $\tilde{k}_{\tilde{M}}(\tilde{m}) = \frac{2\pi\tilde{m}}{na} + \tilde{M}\frac{2\pi}{a}$, $\tilde{M} = 0, 1$.

IR	(k, m)	$(\widetilde{C_{2n} \frac{a}{2}})$	\tilde{C}_n	$\tilde{\sigma}_h$
${}_0A_m^{\Pi_h}$	$k = 0$ $m \in (-n, n]$	$e^{im\frac{\pi}{n}}$	$e^{im\frac{2\pi}{n}}$	Π_h
${}_kE_m$	$k \in (0, \frac{\pi}{a}]$, $m \in (-n, n]$ $k = \frac{\pi}{a}$, $m \in [0, n)$	$e^{im\frac{\pi}{n}}K_2(\frac{ka}{2})$	$e^{im\frac{2\pi}{n}}\mathbb{1}_2$	$\begin{bmatrix} 0 & \Pi_{\tilde{e}'} \\ 1 & 0 \end{bmatrix}$

Table C.5: Irreducible representations of double line groups $\tilde{\mathbf{L}}^{(5)} = \tilde{\mathbf{T}}_Q(f)\tilde{\mathbf{D}}_n$. Helical and linear QNs used as in Table C.1.

IR	(k, m)	$(\widetilde{C_Q^r f})$	\tilde{C}_n	\tilde{U}
${}_kA_m^{\Pi_U}$	$k = 0$, $m = 0, \frac{q}{2}$ $k = \frac{\pi}{a}$, $m = -\frac{p}{2}, \frac{q-p}{2}$	$e^{i(kf+m\frac{2\pi}{Q})}$	$e^{im\frac{2\pi}{n}}$	Π_U
${}_kE_m$	$(^a)$	$\begin{bmatrix} e^{i(kf+m\frac{2\pi}{Q})} & 0 \\ 0 & e^{-i(kf+m\frac{2\pi}{Q})} \end{bmatrix}$	$M_2(m)$	$\begin{bmatrix} 0 & \Pi_{\tilde{e}'} \\ 1 & 0 \end{bmatrix}$
${}_{\tilde{k}}A_{\tilde{m}}^{\Pi_U}$	$\tilde{k} = 0, \frac{\pi}{f}$, $\tilde{m} = 0, \frac{n}{2}$	$e^{i\tilde{k}f}$	$e^{i\tilde{m}\frac{2\pi}{n}}$	Π_U
${}_{\tilde{k}}E_{\tilde{m}}$	$\tilde{k} = 0, \frac{\pi}{f}$; $\tilde{m} \in (0, \frac{n}{2})$ $\tilde{k} \in (0, \frac{\pi}{f})$, $\tilde{m} \in (-\frac{n}{2}, \frac{n}{2}]$	$\begin{bmatrix} e^{i\tilde{k}f} & 0 \\ 0 & e^{-i\tilde{k}f} \end{bmatrix}$	$M_2(\tilde{m})$	$\begin{bmatrix} 0 & \Pi_{\tilde{e}'} \\ 1 & 0 \end{bmatrix}$

(^a) $k \in (0, \frac{\pi}{a})$, $m \in (-\frac{q}{2}, \frac{q}{2}]$; $k = 0$, $m \in (0, \frac{q}{2})$; $k = \frac{\pi}{a}$, $m \in (-\frac{p}{2}, \frac{q-p}{2})$.

Table C.6: Irreducible representations of double line groups $\tilde{\mathbf{L}}^{(6)} = \tilde{\mathbf{L}}nmm, \tilde{\mathbf{L}}nm = \tilde{\mathbf{T}}(a)\tilde{\mathbf{C}}_{nv}$.

IR	(k, m)	$(\widetilde{\mathbb{1}_3 a})$	\tilde{C}_n	$\tilde{\sigma}_v$
${}_kA/B_m$	$k \in (-\frac{\pi}{a}, \frac{\pi}{a}]$ $m = 0, \frac{n}{2}$	e^{ika}	$e^{im\frac{2\pi}{n}}$	Π_v
${}_kE_m$	$k \in (-\frac{\pi}{a}, \frac{\pi}{a}]$ $m \in (0, \frac{n}{2})$	$e^{ika}\mathbb{1}_2$	$M_2(m)$	$\begin{bmatrix} 0 & \Pi_{\tilde{e}'} \\ 1 & 0 \end{bmatrix}$

Table C.7: Irreducible representations of double line groups $\tilde{\mathbf{L}}^{(7)} = \tilde{\mathbf{L}}ncc, \tilde{\mathbf{L}}nc = \tilde{\mathbf{T}}'(\frac{a}{2})\tilde{\mathbf{C}}_n$.

IR	(k, m)	$(\widetilde{\sigma_v \frac{a}{2}})$	$\tilde{\mathbf{C}}_n$
${}_kA/B_m$	$k \in (-\frac{\pi}{a}, \frac{\pi}{a}]$ $m = 0, \frac{n}{2}$	$\Pi_v e^{ik\frac{a}{2}}$	$e^{im\frac{2\pi}{n}}$
${}_kE_m$	$k \in (-\frac{\pi}{a}, \frac{\pi}{a}]$ $m \in (0, \frac{n}{2})$	$e^{im\pi} \begin{bmatrix} 0 & e^{ik\frac{a}{2}} \\ e^{ik\frac{a}{2}} & 0 \end{bmatrix}$	$M_2(m)$

Table C.8: Irreducible representations of double line groups $\tilde{\mathbf{L}}^{(8)} = \tilde{\mathbf{L}}2n_nmc = \tilde{\mathbf{T}}_{2n}^1(\frac{a}{2})\tilde{\mathbf{C}}_{nv}$.

IR	(k, m)	$(\widetilde{C_{2n} \frac{a}{2}})$	$\tilde{\mathbf{C}}_n$	$\tilde{\sigma}_v$
${}_kA/B_m$	$k \in (-\frac{\pi}{a}, \frac{\pi}{a}]$ $m = 0, n$	$e^{i(k\frac{a}{2} + m\frac{\pi}{n})}$	1	Π_v
${}_kE_m$	$k \in (-\frac{\pi}{a}, \frac{\pi}{a}]$ $m \in (0, n)$	$e^{ik\frac{a}{2}} M_2(\frac{m}{2})$	$M_2(m)$	$\begin{bmatrix} 0 & \Pi_{\tilde{e}'} \\ 1 & 0 \end{bmatrix}$

Table C.9: Irreducible representations of double line groups $\tilde{\mathbf{L}}^{(9)} = \tilde{\mathbf{L}}2\bar{n}2m, \tilde{\mathbf{L}}\bar{n}m = \tilde{\mathbf{T}}(a)\tilde{\mathbf{D}}_{nd}$.

IR	(k, m)	$(\widetilde{\mathbf{1}_3 a})$	$\tilde{\mathbf{C}}_n$	$\tilde{\mathbf{U}}_d$	$\tilde{\sigma}_v$
${}_kA/B_0^{\Pi_U}$	$(^a)$	e^{ika}	$e^{im\frac{2\pi}{n}}$	Π_U	Π_v
${}_kE_m^{\Pi_h}$	$k = 0, \frac{\pi}{a}$ $m \in (0, \frac{n}{2})$	$e^{ika} \mathbf{1}_2$	$M_2(m)$	$\Pi_h \begin{bmatrix} 0 & \Pi_{\tilde{e}'} e^{i\frac{\pi m}{n}} \\ e^{-i\frac{\pi m}{n}} & 0 \end{bmatrix}$	$\begin{bmatrix} 0 & \Pi_{\tilde{e}'} \\ 1 & 0 \end{bmatrix}$
${}_kE_m$	$(^b)$	$e^{ika} \mathbf{1}_2$	$-\mathbf{1}_2$	$\begin{bmatrix} 0 & \Pi_{\tilde{e}'} \\ 1 & 0 \end{bmatrix}$	$e^{i\pi\frac{n}{2}} \begin{bmatrix} 1 & 0 \\ 0 & -\Pi_{\tilde{e}'} \end{bmatrix}$
${}_kE_m^{\Pi_v}$	$k \in (0, \frac{\pi}{a})$ $m = 0, \frac{n}{2}$	$K_2(ka)$	$e^{im\frac{2\pi}{n}} \mathbf{1}_2$	$\begin{bmatrix} 0 & \Pi_{\tilde{e}'} \\ 1 & 0 \end{bmatrix}$	$\Pi_v \begin{bmatrix} 1 & 0 \\ 0 & \Pi_{\tilde{e}'} e^{im\frac{2\pi}{n}} \end{bmatrix}$
${}_kG_m$	$k \in (0, \frac{\pi}{a})$ $m \in (0, \frac{n}{2})$	$K_4(ka)$	N	$\begin{bmatrix} 0 & 0 & \Pi_{\tilde{e}'} & 0 \\ 0 & 0 & 0 & \Pi_{\tilde{e}'} \\ 1 & 0 & 0 & 0 \\ 0 & 1 & 0 & 0 \end{bmatrix}$	$\begin{bmatrix} 0 & \Pi_{\tilde{e}'} & 0 & 0 \\ 1 & 0 & 0 & 0 \\ 0 & 0 & 0 & e^{im\frac{2\pi}{n}} \\ 0 & 0 & \Pi_{\tilde{e}'} e^{-im\frac{2\pi}{n}} & 0 \end{bmatrix}$

(^a) n even: $k = 0, \frac{\pi}{a}$; n odd: $k = 0, \frac{\pi}{a}$, $m = 0, \frac{n}{2}$.
(^b) only for n even: $k = 0, \frac{\pi}{a}$, $m = \frac{n}{2}$.

Table C.10: Irreducible representations of double line groups $\tilde{\mathbf{L}}^{(10)} = \tilde{\mathbf{L}}\overline{2n}2c, \tilde{\mathbf{L}}\overline{n}c = \tilde{\mathbf{T}}'(\frac{a}{2})\tilde{\mathbf{S}}_{2n}$. In this table we use $\alpha = k\frac{a}{2} + m\pi$.

IR	(k, m)	$(\widetilde{\sigma_v \frac{a}{2}})$	\tilde{S}_{2n}
${}_k A/B_m^{\Pi_U}$	$(^a)$	$\Pi_v e^{ik\frac{a}{2}}$	$\Pi_U \Pi_v e^{ik\frac{a}{2}}$
${}_k E_m$	$(^b)$	$\begin{bmatrix} e^{im\pi} e^{ik\frac{a}{2}} & 0 \\ 0 & e^{-im\pi} e^{i(m\frac{2\pi}{n} - k\frac{a}{2})} \end{bmatrix}$	$\begin{bmatrix} 0 & \Pi_{\tilde{e}'} e^{im\frac{2\pi}{n}} \\ 1 & 0 \end{bmatrix}$
${}_k E_m^{\Pi_h}$	$k = 0, \frac{\pi}{a}, \frac{n}{2}$ $m \in (0, \frac{n}{2})$	$\begin{bmatrix} 0 & e^{i\alpha} \\ e^{i\alpha} & 0 \end{bmatrix}$	$\Pi_h \begin{bmatrix} e^{im\frac{\pi}{n}} & 0 \\ 0 & \Pi_{\tilde{e}'} e^{i(ka - m\frac{\pi}{n})} \end{bmatrix}$
${}_k E_m^{\Pi_v}$	$k \in (0, \frac{\pi}{a})$ $m = 0, \frac{n}{2}$	$\Pi_v \begin{bmatrix} e^{ik\frac{a}{2}} & 0 \\ 0 & \Pi_{\tilde{e}'} e^{i(m\frac{2\pi}{n} - k\frac{a}{2})} \end{bmatrix}$	$\begin{bmatrix} 0 & \Pi_{\tilde{e}'} e^{im\frac{2\pi}{n}} \\ 1 & 0 \end{bmatrix}$
${}_k G_m$	$k \in (0, \frac{\pi}{a})$ $m \in (0, \frac{n}{2})$	$\begin{bmatrix} 0 & e^{i\alpha} & 0 & 0 \\ e^{i\alpha} & 0 & 0 & 0 \\ 0 & 0 & 0 & e^{-i(m\frac{2\pi}{n} + \alpha)} \\ 0 & 0 & e^{i(m\frac{2\pi}{n} - \alpha)} & 0 \end{bmatrix}$	$\begin{bmatrix} 0 & 0 & \Pi_{\tilde{e}'} e^{im\frac{2\pi}{n}} & 0 \\ 0 & 0 & 0 & \Pi_{\tilde{e}'} e^{-im\frac{2\pi}{n}} \\ 1 & 0 & 0 & 0 \\ 0 & 1 & 0 & 0 \end{bmatrix}$

(^a) n even: $k = 0, m = 0; k = \frac{\pi}{a}, m = \frac{n}{2}; n$ odd: $k = 0, m = 0, \frac{n}{2}$.

(^b) n even: $k = 0, m = \frac{n}{2}; k = \frac{\pi}{a}, m = 0; n$ odd: $k = \frac{\pi}{a}, m = 0, \frac{n}{2}$.

Table C.11: Irreducible representations of double line groups $\tilde{\mathbf{L}}^{(11)} = \tilde{\mathbf{L}}n/mmm, \tilde{\mathbf{L}}\overline{2n}2m = \tilde{\mathbf{T}}\tilde{\mathbf{D}}_{nh}$.

IR	(k, m)	$(\widetilde{1_3 a})$	\tilde{C}_n	$\tilde{\sigma}_v$	$\tilde{\sigma}_h$
${}_k A/B_m^{\Pi_h}$	$k = 0, \frac{\pi}{a}, \frac{n}{2}$ $m = 0, \frac{n}{2}$	e^{ika}	$e^{im\frac{2\pi}{n}}$	Π_v	Π_h
${}_k E_m^{\Pi_h}$	$k = 0, \frac{\pi}{a}, \frac{n}{2}$ $m \in (0, \frac{n}{2})$	$e^{ika} \mathbf{1}_2$	$M_2(m)$	$\begin{bmatrix} 0 & \Pi_{\tilde{e}'} \\ 1 & 0 \end{bmatrix}$	$\Pi_h \begin{bmatrix} 1 & 0 \\ 0 & \Pi_{\tilde{e}'} \end{bmatrix}$
${}_k E_m^{\Pi_v}$	$k \in (0, \frac{\pi}{a})$ $m = 0, \frac{n}{2}$	$K_2(ka)$	$e^{im\frac{2\pi}{n}} \mathbf{1}_2$	$\Pi_v \begin{bmatrix} 1 & 0 \\ 0 & \Pi_{\tilde{e}'} \end{bmatrix}$	$\begin{bmatrix} 0 & \Pi_{\tilde{e}'} \\ 1 & 0 \end{bmatrix}$
${}_k G_m$	$k \in (0, \frac{\pi}{a})$ $m \in (0, \frac{n}{2})$	$K_4(ka)$	$M(m)$	$\begin{bmatrix} 0 & \Pi_{\tilde{e}'} & 0 & 0 \\ 1 & 0 & 0 & 0 \\ 0 & 0 & 0 & 1 \\ 0 & 0 & \Pi_{\tilde{e}'} & 0 \end{bmatrix}$	$\begin{bmatrix} 0 & 0 & \Pi_{\tilde{e}'} & 0 \\ 0 & 0 & 0 & \Pi_{\tilde{e}'} \\ 1 & 0 & 0 & 0 \\ 0 & 1 & 0 & 0 \end{bmatrix}$

Table C.12: Irreducible representations of double line groups $\tilde{\mathbf{L}}^{(12)} = \tilde{\mathbf{L}}n/mcc, \tilde{\mathbf{L}}2\bar{n}2c = \tilde{\mathbf{T}}'(\frac{a}{2})\tilde{\mathbf{C}}_{nh}$.

IR	(k, m)	$(\widetilde{\sigma_v \frac{a}{2}})$	\tilde{C}_n	$\tilde{\sigma}_h$
${}_0A/B_m^{\Pi_h}$	$(^a)$	Π_v	$e^{im\frac{2\pi}{n}}$	Π_h
${}_kE_m^{\Pi_h}$	$k = 0, \frac{\pi}{a}$ $m \in (0, \frac{n}{2})$	$e^{im\pi} \begin{bmatrix} 0 & e^{i\frac{ka}{2}} \\ e^{i\frac{ka}{2}} & 0 \end{bmatrix}$	$M_2(m)$	$\Pi_h \begin{bmatrix} 1 & 0 \\ 0 & \Pi_{\tilde{e}'} e^{ika} \end{bmatrix}$
${}_kE_m^{\Pi_v}$	$k \in (0, \frac{\pi}{a})$ $m = 0, \frac{n}{2}$	$\Pi_v \begin{bmatrix} e^{i\frac{ka}{2}} & 0 \\ 0 & \Pi_{\tilde{e}'} e^{-i\frac{ka}{2}} \end{bmatrix}$	$e^{im\frac{2\pi}{n}} \mathbb{1}_2$	$\begin{bmatrix} 0 & \Pi_{\tilde{e}'} \\ 1 & 0 \end{bmatrix}$
${}_kE_m$	$(^b)$	$\begin{bmatrix} e^{i\frac{ka}{2}} & 0 \\ 0 & e^{-i\frac{ka}{2}} \end{bmatrix}$	$e^{im\frac{2\pi}{n}} \mathbb{1}_2$	$\begin{bmatrix} 0 & \Pi_{\tilde{e}'} \\ 1 & 0 \end{bmatrix}$
${}_kG_m$	$k \in (0, \frac{\pi}{a})$ $m \in (0, \frac{n}{2})$	$\begin{bmatrix} 0 & e^{i(ka+m\pi)} & 0 & 0 \\ e^{im\pi} & 0 & 0 & 0 \\ 0 & 0 & 0 & e^{-i(ka+m\pi)} \\ 0 & 0 & e^{-im\pi} & 0 \end{bmatrix}$	$M(m)$	$\begin{bmatrix} 0 & 0 & \Pi_{\tilde{e}'} & 0 \\ 0 & 0 & 0 & \Pi_{\tilde{e}'} \\ 1 & 0 & 0 & 0 \\ 0 & 1 & 0 & 0 \end{bmatrix}$

$(^a)$ n even: $k = 0, m = 0, \frac{n}{2}$; n odd: $k = 0, m = 0$.

$(^b)$ n even: $k = \frac{\pi}{a}, m = 0, \frac{n}{2}$; n odd: $k = \frac{\pi}{a}, m = 0, \frac{n}{2}; k = 0, m = \frac{n}{2}$.

Table C.13: Irreducible representations of double line groups $\tilde{\mathbf{L}}^{(13)} = \tilde{\mathbf{L}}2n_n/mmm = \tilde{\mathbf{T}}_{2n}^1(\frac{a}{2})\tilde{\mathbf{D}}_{nh}$. Here, $\tilde{K}(\tilde{k}, \tilde{m}) = \text{diag}[e^{i\frac{\tilde{k}a}{2}}, e^{i\frac{\tilde{k}a-2\tilde{m}\alpha}{2}}, e^{-i\frac{\tilde{k}a-2\tilde{m}\alpha}{2}}, e^{-i\frac{\tilde{k}a}{2}}]$, $\tilde{k}_{\tilde{M}}(\tilde{m}) = \frac{\alpha\tilde{m}+2\pi\tilde{M}}{a}$ ($\tilde{M} = 0, 1$), $\alpha = \frac{2\pi}{n}$.

IR	(k, m)	$(\widetilde{C_{2n} \frac{a}{2}})$	\tilde{C}_n	\tilde{U}	$\tilde{\sigma}_v$
${}_0A/B_m^{\Pi_h}$	$k = 0$ $m = 0, n$	$e^{im\frac{\pi}{n}}$	1	$\Pi_h \Pi_v$	Π_v
${}_0E_m^{\Pi_h}$	$k = 0$ $m \in (0, n)$	$M_2(\frac{m}{2})$	$M_2(m)$	$\Pi_h \begin{bmatrix} 0 & 1 \\ 1 & 0 \end{bmatrix}$	$\begin{bmatrix} 0 & \Pi_{\tilde{e}'} \\ 1 & 0 \end{bmatrix}$
${}_kE_m^{A/B}$	$k \in (0, \frac{\pi}{a}), m = 0, n$ $k = \frac{\pi}{a}, m = 0$	$e^{im\frac{\pi}{n}} K_2(\frac{ka}{2})$	$\mathbb{1}_2$	$\Pi_v \begin{bmatrix} 0 & 1 \\ 1 & 0 \end{bmatrix}$	$\Pi_v \begin{bmatrix} 1 & 0 \\ 0 & \Pi_{\tilde{e}'} \end{bmatrix}$
${}_{\frac{\pi}{a}}E_m^{\Pi_U}$	$k = \frac{\pi}{a}$ $m = \frac{n}{2}$	$\begin{bmatrix} -1 & 0 \\ 0 & 1 \end{bmatrix}$	$-\mathbb{1}_2$	$\Pi_U \begin{bmatrix} 1 & 0 \\ 0 & \Pi_{\tilde{e}'} \end{bmatrix}$	$\begin{bmatrix} 0 & \Pi_{\tilde{e}'} \\ 1 & 0 \end{bmatrix}$
${}_kG_m$	$k \in (0, \frac{\pi}{a}), m \in (0, n)$ $k = \frac{\pi}{a}, m \in (0, \frac{n}{2})$	$K_4(\frac{ka}{2}) M_4(\frac{m}{2})$	$M_4(m)$	$\begin{bmatrix} 0 & 0 & 0 & \Pi_{\tilde{e}'} \\ 0 & 0 & 1 & 0 \\ 0 & \Pi_{\tilde{e}'} & 0 & 0 \\ 1 & 0 & 0 & 0 \end{bmatrix}$	$\begin{bmatrix} 0 & \Pi_{\tilde{e}'} & 0 & 0 \\ 1 & 0 & 0 & 0 \\ 0 & 0 & 0 & 1 \\ 0 & 0 & \Pi_{\tilde{e}'} & 0 \end{bmatrix}$

Bibliography

- [1] S. A. Wolf, D. D. Awschalom, R. A. Buhrman, J. M. Daughton, S. von Molnar, M. L. Roukes, A. Y. Chtchelkanova and D. M. Treger, *Science* **294**, 1488 (2001). <https://science.sciencemag.org/content/294/5546/1488>.
- [2] S. Das Sarma, J. Fabian, X. Hu and I. Žutić, *Solid State Commun.* **119**, 207 (2001). <https://www.sciencedirect.com/science/article/pii/S0038109801001119>
- [3] S. Bandyopadhyay and M. Cahay, (CRC Press Taylor & Francis Group, Florida, 2008), *Introduction To Spintronics*. <https://www.crcpress.com/Introduction-to-Spintronics/Bandyopadhyay-Cahay/p/book/9781482255560>
- [4] G. Dresselhaus, *Phys. Rev.* **100**, 580 (1955); <https://journals.aps.org/pr/abstract/10.1103/PhysRev.100.580>.
- [5] F. M. Silva Júnior and C. W. A. Paschoal, *J. Appl. Phys.* **116**, 244110 (2014). <https://aip.scitation.org/doi/abs/10.1063/1.4904062>.
- [6] E. Aytan, B. Debnath, F. Kargar, Y. Barlas, M. M. Lacerda, J. X. Li, R. K. Lake, J. Shi and A. A. Balandin, *Appl. Phys. Lett.* **111**, 252402 (2017). <https://aip.scitation.org/doi/abs/10.1063/1.5009598>
- [7] M. A. Prosnikov, A. N. Smirnov, V. Yu. Davydov, R. V. Pisarev, N. A. Lyubochko and S. N. Barilo, *Phys. Rev. B* **98**, 104404 (2018). <https://journals.aps.org/prb/abstract/10.1103/PhysRevB.98.104404>
- [8] A. Milosavljević, A. Šolajić, J. Pešić, Y. Liu, Č. Petrović, N. Lazarević and Z. V. Popović, *Phys. Rev. B* **98**, 104306 (2018). <https://journals.aps.org/prb/abstract/10.1103/PhysRevB.98.104306>

- [9] E. I. Rashba, *Fiz. Tv. Tela (Leningrad)* **2**, 1224 (1960); *Sov. Phys. Solid State* **2**, 1109 (1960).
- [10] A. Manchon, H. C. Koo, J. Nitta, S. M. Frolov and R. A. Duine, *Nat. Mater.* **14**, 871882 (2015). <https://www.nature.com/articles/nmat4360>
- [11] C. J. Bradley and A. P. Cracknell, (Clarendon, Oxford, 2010), *The Mathematical Theory of Symmetry in Solids*.
<https://global.oup.com/academic/product/the-mathematical-theory-of-symmetry-in-solids-9780199582587>
- [12] I Milošević, B. Nikolić, M. Damnjanović and M. Krčmar, *J. Phys. A: Math. Gen.* **31**, 3625 (1998). <https://iopscience.iop.org/article/10.1088/0305-4470/31/15/023/meta>
- [13] M. Damnjanović and I. Milošević, (Springer-Verlag, Berlin, 2010), *Line Groups in Physics*. <https://www.springer.com/gp/book/9783642111716>
- [14] R. J. Elliott, *Phys. Rev.* **96**, 280 (1954). <https://journals.aps.org/pr/abstract/10.1103/PhysRev.96.280>
- [15] G. Dresselhaus, A. F. Kip and C. Kittel, *Phys. Rev.* **95**, 568 (1954). <https://journals.aps.org/pr/abstract/10.1103/PhysRev.95.568>
- [16] H. A. Bethe, *Ann. Phys.* vol. 395, **2**, 133-208 (1929). <https://onlinelibrary.wiley.com/doi/abs/10.1002/andp.19293950202>
- [17] W. Opechowski, *Physica* **7**, 552 (1940). <https://www.sciencedirect.com/science/article/pii/S0031891440900453>
- [18] L. D. Landau and L. M. Lifshitz, (Pergamon Press, Oxford, 1977), *Quantum Mechanics: Non-relativistic Theory*. <https://doi.org/10.1016/C2013-0-02793-4>
- [19] S. L. Altmann, (Dover, New York, 2005), *Rotations, Quaternions and Double Groups*. <https://store.doverpublications.com/0486445186.html>
- [20] L. Chico, M. P. López-Sancho and M. C. Muñoz, *Phys. Rev. Lett.* **93**, 176402 (2004). <https://journals.aps.org/prl/abstract/10.1103/PhysRevLett.93.176402>

- [21] L. Chico, M. P. López-Sancho and M. C. Muñoz, *Phys. Rev. B.* **79**, 235423 (2009). <https://journals.aps.org/prb/abstract/10.1103/PhysRevB.79.235423>
- [22] W. Izumida, K. Sato and R. Saito, *J. Phys. Soc. Jpn.* **78**, 074707 (2009). <https://journals.jps.jp/doi/abs/10.1143/JPSJ.78.074707>
- [23] F. Kuemmeth, S. Ilani, D. Ralph and P. McEuen, *Nature* **452**, 448 (2008). <https://www.nature.com/articles/nature06822>
- [24] G. A. Steele, F. Pei, E. A. Laird, J. M. Jol, H. B. Meerwaldt and L. P. Kouwenhoven, *Nat. Commun.* **4**, 1573 (2013). <https://www.nature.com/articles/ncomms2584>
- [25] M. Damnjanović and I. Milošević *Phys. Rep.* **581**, 143 (2015). <https://www.sciencedirect.com/science/article/abs/pii/S0370157315002288>
- [26] S. L. Altmann, *Mol. Phys.* **38**, 2 (1979). <https://doi.org/10.1080/00268977900101831>
- [27] N. Lazić, M. Milivojević, T. Vuković and M. Damnjanović, *J. Phys. A: Math. Theor.* **51**, 225203 (2018). <https://iopscience.iop.org/article/10.1088/1751-8121/aabe9a/pdf>
- [28] S. Reich, C. Thomsen and J. Maultzsch, (Wiley-VCH, Weinheim, 2004) *Carbon nanotubes*. <https://www.wiley.com/en-us/Carbon+Nanotubes%3A+Basic+Concepts+and+Physical+Properties-p-9783527403868>
- [29] M. Damnjanović, I. Milošević, E. Dobardžić, T. Vuković and B. Nikolić, (Springer-Verlag, Berlin, 2005), *Symmetry Based Fundamentals on Carbon Nanotubes*, Ch.2 (p41-88) in *Applied Physics of Nanotubes: Fundamentals of Theory, Optics and Transport Devices*, eds. Slava V Rotkin and Shekhar Subramoney. https://link.springer.com/chapter/10.1007/3-540-28075-8_2
- [30] S. Dmitrović, T. Vuković, Z. P. Popović, I. Milošević and M. Damnjanović, *J. Phys: Condens. Matter.* **25**, 145301 (2013). <https://iopscience.iop.org/article/10.1088/0953-8984/25/14/145301/meta>

- [31] S. Dmitrović, I. Milošević, M. Damnjanović and T. Vuković, *J. Phys. Chem. C* **119** (24), 13922-13928 (2015). <https://pubs.acs.org/doi/abs/10.1021/acs.jpcc.5b02455>
- [32] M. Damnjanović, (Fizički fakultet, Beograd, 2016), *Grupe i Hilbertovi prostori*. <http://www.ff.bg.ac.rs/Katedre/QMF/SiteQMF/pdf/y2k2016.pdf>
- [33] L. Jansen and M. Boon, (North-Holland, Amsterdam, 1967), *Theory of Finite Groups. Applications in Physics*. <https://www.amazon.com/Theory-finite-groups-Applications-mechanical/dp/B0007IU712>
- [34] I. Božović, M. Vujičić, F. Herbut, *J. Phys. A* **11**, 2133 (1978). <https://iopscience.iop.org/article/10.1088/0305-4470/11/11/003>
- [35] I. Božović, M. Vujičić, *J. Phys. A* **14**, 777 (1981). <https://iopscience.iop.org/article/10.1088/0305-4470/14/4/009>
- [36] M. Milivojević, N. Lazić, S. Dmitrović, M. Damnjanović, T. Vuković, *Phys. Status Solidi B* **255**, 1800184 (2018). <https://onlinelibrary.wiley.com/doi/abs/10.1002/pssb.201800184>
- [37] E. U. Condon and G. H. Shortley, (Cambridge University Press, Cambridge, 1935), *The Theory of Atomic Spectra*. <https://www.amazon.com/Theory-Atomic-Spectra-U-Condon/dp/0521092094>
- [38] K. V. Shanavas, Z. S. Popović and S. Satpathy, *Phys. Rev. B* **90**, 165108 (2014). <https://journals.aps.org/prb/abstract/10.1103/PhysRevB.90.165108>
- [39] F. Herman and S. Skillman, (Prentice Hall, Englewood Cliffs, NJ, 1963, p. 26), *Atomic Structure Calculations*. https://openlibrary.org/books/OL16552153M/Atomic_structure_calculations_by_Frank_Herman_and_Sherwood_Skillman
- [40] H. Min, J. E. Hill, N. A. Sinitsyn, B. R. Sahu, L. Kleinman and A. H. MacDonald, *Phys. Rev. B* **74**, 165310 (2006). <https://journals.aps.org/prb/abstract/10.1103/PhysRevB.74.165310>

- [41] F. Guinea, *New J. Phys.* **12**, 083063 (2010). <https://iopscience.iop.org/article/10.1088/1367-2630/12/8/083063/meta>
- [42] L. C. Lew Yan Voon and M. Willatzen, (Springer-Verlag, Berlin, 2009), *The k -p Method: Electronic Properties of Semiconductors*. <https://www.springer.com/gp/book/9783540928713>
- [43] T. Ando, *J. Phys. Soc. Jpn.* **69**, 1757-1763 (2000). <https://journals.jps.jp/doi/abs/10.1143/JPSJ.69.1757>
- [44] R. Winkler, (Springer-Verlag, Berlin, 2003), *Spin-Orbit Coupling Effects in Two-Dimensional Electron and Hole Systems*. <https://www.springer.com/gp/book/9783540011873>
- [45] J. Fabian, A. Matos-Abiague, C. Ertler, P. Stano and I. Zutić, *Acta Physica Slovaca* **57**, 565 (2007). <http://www.physics.sk/aps/pub.php?y=2007&pub=aps-07-04>
- [46] S. Konschuh, M. Gmitra and J. Fabian, *Phys. Rev. B* **82**, 245412 (2010). <https://journals.aps.org/prb/abstract/10.1103/PhysRevB.82.245412>
- [47] P. Li and I. Appelbaum, *Phys. Rev. B* **90**, 115439 (2014). <https://journals.aps.org/prb/abstract/10.1103/PhysRevB.90.115439>
- [48] A. Kormányos, G. Burkard, M. Gmitra, J. Fabian, V. Zólyomi, N. D. Drummond, V. Fal'ko, *2D Mater.* **2**, 022001 (2015). <https://iopscience.iop.org/article/10.1088/2053-1583/2/2/022001/meta>
- [49] P. E. Faria Junior, T. Campos, C. M. O. Bastos, M. Gmitra, J. Fabian and G. M. Sipahi, *Phys. Rev. B* **93**, 235204 (2016). <https://journals.aps.org/prb/abstract/10.1103/PhysRevB.93.235204>
- [50] R. Okuyama, W. Izumida and M. Eto, *J. Phys. Soc. Jpn.* **86**, 013702 (2017). <https://journals.jps.jp/doi/full/10.7566/JPSJ.86.013702>
- [51] J. M. Luttinger and W. Kohn *Phys. Rev.* **97**, 869 (1955). <https://journals.aps.org/pr/abstract/10.1103/PhysRev.97.869>

- [52] W. Izumida, R. Okuyama and R. Saito, *Phys. Rev. B* **91** 235442 (2015).
<https://journals.aps.org/prb/abstract/10.1103/PhysRevB.91.235442>
- [53] J. Kessler, (Springer-Verlag, Berlin, 1985) *Polarized electrons*. <https://www.springer.com/gp/book/9783540157366>
- [54] S. Iijima, *Nature* **354**, 5658 (1991). <https://www.nature.com/articles/354056a0>
- [55] S. Iijima and T. Ichihashi, *Nature* **363**, 603-605 (1993). <https://www.nature.com/articles/363603a0>
- [56] N. Hamada, Shin-ichi Sawada and A. Oshiyama, *Phys. Rev. Lett.* **68**, 1579 (1992). <https://journals.aps.org/prl/abstract/10.1103/PhysRevLett.68.1579>
- [57] R. Saito, M. Fujita, G. Dresselhaus and M. S. Dresselhaus, *Phys. Rev. B* **46**, 1804 (1992). <https://journals.aps.org/prb/abstract/10.1103/PhysRevB.46.1804>
- [58] R. Saito, M. Fujita, G. Dresselhaus and M. S. Dresselhaus, *Appl. Phys. Lett.* **60**, 2204 (1992). <https://aip.scitation.org/doi/abs/10.1063/1.107080>
- [59] J. W. Mintmire, B. I. Dunlap and C. T. White, *Phys. Rev. Lett.* **68**, 631 (1992).
<https://journals.aps.org/prl/abstract/10.1103/PhysRevLett.68.631>
- [60] R. Saito, G. Dresselhaus and M. S. Dresselhaus, (Imperial College Press, London, 1998) *Physical properties of carbon nanotubes*. <https://www.worldscientific.com/worldscibooks/10.1142/p080>
- [61] M. M. J. Treacy, T. W. Ebbesen and J. M. Gibson, *Nature* **381**, 678-680 (1996). <https://www.nature.com/articles/381678a0>
- [62] J. Hone, M. C. Llaguno, M. J. Biercuk, A. T. Johnson, B. Batlogg, Z. Benes and J. E. Fischer, *Appl. Phys. A* **72**, 339 (2002). <https://doi.org/10.1007/s003390201277>
- [63] K. S. Novoselov, A. K. Geim, S. V. Morozov, D. Jiang, Y. Zhang, S. V. Dubonos, I. V. Grigorieva and A. A. Firsov, *Science* **306**, 666 (2004). <https://science.sciencemag.org/content/306/5696/666>

- [64] M. Damnjanović, I. Milošević, T. Vuković and R. Sredanović, *Phys. Rev. B* **60**, 2728 (1999). <https://journals.aps.org/prb/abstract/10.1103/PhysRevB.60.2728>
- [65] N. Lazić, T. Vuković, G. Volonakis, I. Milošević, S. Logothetidis and M. Damnjanović, *J. Phys.: Condens. Matter* **24**, 485302 (2012). <https://iopscience.iop.org/article/10.1088/0953-8984/24/48/485302/meta>
- [66] M. Abud and G. Sartori, *Ann. Phys.* **150**, 307 (1983). <https://www.sciencedirect.com/science/article/pii/0003491683900179>
- [67] S. Dmitrović, PhD Thesis, (University of Belgrade, Serbia 2013), *Electronic and optical properties of deformed graphitic and helical nanotubes*; <https://fedorabg.bg.ac.rs/fedora/get/o:7012/bdef:Asset/view?language=en>.
- [68] J. C. Slonczewski and P. R. Weiss, *Phys. Rev.* **109**, 272 (1958). <https://journals.aps.org/pr/abstract/10.1103/PhysRev.109.272>
- [69] M. Gmitra, S. Konschuh, C. Ertler, C. Ambrosch-Draxl and J. Fabian, *Phys. Rev. B* **80**, 235431 (2009). <https://journals.aps.org/prb/abstract/10.1103/PhysRevB.80.235431>
- [70] D. Kochan, S. Irmer and J. Fabian, *Phys. Rev. B* **95**, 165415 (2017). <https://journals.aps.org/prb/abstract/10.1103/PhysRevB.95.165415>
- [71] D. Huertas-Hernando, F. Guinea and A. Brataas, *Phys. Rev. B* **74**, 155426 (2006). <https://journals.aps.org/prb/abstract/10.1103/PhysRevB.74.155426>
- [72] J. Jeong and H. Lee, *Phys. Rev. B* **80**, 075409 (2009). <https://journals.aps.org/prb/abstract/10.1103/PhysRevB.80.075409>
- [73] J. Klinovaja, M. J. Schmidt, B. Braunecker and D. Loss, *Phys. Rev. B* **84**, 085452 (2011). <https://journals.aps.org/prb/abstract/10.1103/PhysRevB.84.085452>
- [74] J. Zhou, Q. Liang and J. Dong, *Phys. Rev. B* **79**, 195427 (2009). <https://journals.aps.org/prb/abstract/10.1103/PhysRevB.79.195427>

- [75] V. V. Maslyuk, R. Gutierrez and G. Cuniberti, *Phys. Chem. Chem. Phys.* **19**, 8848-8853 (2017). <https://pubs.rsc.org/en/content/articlelanding/2017/cp/c7cp00059f#!divAbstract>
- [76] D. Porezag, T. Frauenheim, T. Köhler, G. Seifert and R. Kaschner, *Phys. Rev. B* **51**, 12947 (1995); M. Elstner, D. Porezag, G. Jungnickel, J. Elsner, M. Haugk, Th. Frauenheim, S. Suhai and G. Seifert, *Phys. Rev. B* **58**, 7260 (1998). <https://journals.aps.org/prb/abstract/10.1103/PhysRevB.51.12947> <https://journals.aps.org/prb/abstract/10.1103/PhysRevB.58.7260>
- [77] M. Damnjanović, T. Vuković and I. Milošević, *Solid State Comm.* **116**, 265-267 (2000). <https://www.sciencedirect.com/science/article/pii/S0038109800003197>
- [78] K. F. Mak, C. Lee, J. Hone, J. Shan and T. F. Heinz, *Phys. Rev. Lett.* **105**, 136805 (2010). <https://journals.aps.org/prl/abstract/10.1103/PhysRevLett.105.136805>
- [79] E. S. Kadantsev and P. Hawrylak, *Solid State Commun.* **152**, 909-913 (2012). <https://www.sciencedirect.com/science/article/pii/S0038109812000889?via%3Dihub>
- [80] E. Cappelluti, R. Roldán, J. A. Silva-Guillén, P. Ordejón and F. Guinea, *Phys. Rev. B* **88**, 075409 (2013). <https://journals.aps.org/prb/abstract/10.1103/PhysRevB.88.075409>
- [81] Z. Y. Zhu, Y. C. Cheng and U. Schwingenschlögl, *Phys. Rev. B* **84**, 153402 (2011). <https://journals.aps.org/prb/abstract/10.1103/PhysRevB.84.153402>
- [82] A. Kormányos, V. Zólyomi, N. D. Drummond, P. Rakyta, G. Burkard and Vladimir I. Fal'ko, *Phys. Rev. B* **88**, 045416 (2013). <https://journals.aps.org/prb/abstract/10.1103/PhysRevB.88.045416>
- [83] L. Sun, J. Yan, D. Zhan, L. Liu, H. Hu, H. Li, B. K. Tay, J.-L. Kuo, C.-C. Huang, D. W. Hewak, P. S. Lee and Z. X. Shen, *Phys. Rev. Lett.* **111**, 126801

- (2013). <https://journals.aps.org/prl/abstract/10.1103/PhysRevLett.111.126801>
- [84] K. Kosmider, J. W. González and J. Fernández-Rossier, *Phys. Rev. B* **88**, 245436 (2013). <https://journals.aps.org/prb/abstract/10.1103/PhysRevB.88.245436>
- [85] N. Alidoust, G. Bian, S.-Y. Xu, R. Sankar, M. Neupane, C. Liu, I. Belopolski, D.-X. Qu, J. D. Denlinger, F.-C. Chou and M. Z. Hasan, *Nat. Commun.* **5**, 4673 (2014). <https://www.nature.com/articles/ncomms5673>
- [86] G.-B. Liu, D. Xiao, Y. Yao, X. Xude and W. Yao, *Chem. Soc. Rev.* **44**, 2643-2663 (2015). <https://pubs.rsc.org/en/content/articlelanding/2015/cs/c4cs00301b#!divAbstract>
- [87] K. F. Mak, K. He, J. Shan and T. F. Heinz, *Nat. Nanotechnol.* **7**, 494-498 (2012). <https://www.nature.com/articles/nnano.2012.96>
- [88] R. S. Sundaram, M. Engel, A. Lombardo, R. Krupke, A. C. Ferrari, P. Avouris and M. Steiner, *Nano Lett.* **13**(4), 1416-1421 (2013). <https://pubs.acs.org/doi/abs/10.1021/nl400516a>
- [89] A. R. Klots, A. K. M. Newaz, B. Wang, D. Prasai, H. Krzyzanowska, J. Lin, D. Caudel, N. J. Ghimire, J. Yan, B. L. Ivanov, K. A. Velizhanin, A. Burger, D. G. Mandrus, N. H. Tolk, S. T. Pantelides and K. I. Bolotin, *Sci. Rep.* **4**, 6608 (2014). <https://www.nature.com/articles/srep06608>
- [90] D. Dumcenco, D. Ovchinnikov, K. Marinov, O. Lopez-Sanchez, D. Krasnozhan, M.-W. Chen, P. Gillet, A. Fontcuberta i Morral, A. Radenović and A. Kis, arXiv:1405.0129 (2014). <https://arxiv.org/abs/1405.0129v1>
- [91] W. Li, A. Glen Birdwell, M. Amani, R. A. Burke, X. Ling, Y.-H. Lee, X. Liang, L. Peng, C. A. Richter, J. Kong, D. J. Gundlach and N. V. Nguyen, *Phys. Rev. B* **90**, 195434 (2014). <https://journals.aps.org/prb/abstract/10.1103/PhysRevB.90.195434>
- [92] D. Kozawa, R. Kumar, A. Carvalho, K. Kumar Amara, W. Zhao, S. Wang, M. Toh, R. M. Ribeiro, A. H. Castro Neto, K. Matsuda and G. Eda, *Nat. Commun.* **5**, 4543 (2014). <https://www.nature.com/articles/ncomms5543>

- [93] K. Marinov, A. Avsar, K. Watanabe, T. Taniguchi and A. Kis, *Nat. Commun.* **8**, 1938 (2017). <https://www.nature.com/articles/s41467-017-02047-5>
- [94] R. Tenne, L. Margulis, M. Genut and G. Hodes, *Nature* **360**, 444-446 (1992); L. Margulis, G. Salitra, R. Tenne and M. Talianker, *Nature* **365**, 113-114 (1993). <https://www.nature.com/articles/360444a0> <https://www.nature.com/articles/365113b0>
- [95] R. Tenne, M. Homyonfer and Y. Feldman, *Chem. Mater.* **10**, 3225-3228 (1998). <https://pubs.acs.org/doi/abs/10.1021/cm9802189>
- [96] I. Milošević, T. Vuković, M. Damnjanović and B. Nikolić *Eur. Phys. J. B* **17**, 707-712 (2000). <https://epjb.epj.org/articles/epjb/abs/2000/20/b0210/b0210.html>
- [97] N. Zibouche, A. Kuc and T. Heine, *Eur. Phys. J. B* **85**, 49 (2012). <https://epjb.epj.org/articles/epjb/abs/2012/01/b110442/b110442.html>
- [98] G. Seifert, H. Terrones, M. Terrones, G. Jungnickel and T. Frauenheim, *Phys. Rev. Lett.* **85**, 146 (2000). <https://journals.aps.org/prl/abstract/10.1103/PhysRevLett.85.146>
- [99] G. Seifert, H. Terrones, M. Terrones, G. Jungnickel and T. Frauenheim, *Solid State Commun.* **114**, 245 (2000). <https://www.sciencedirect.com/science/article/pii/S0038109800000478>
- [100] I. Milošević, B. Nikolić, E. Dobardžić, M. Damnjanović, I. Popov and G. Seifert, *Phys. Rev. B* **76**, 233414 (2007). <https://journals.aps.org/prb/abstract/10.1103/PhysRevB.76.233414>
- [101] L. Margulis, P. Dluzewski, Y. Feldman and R. Tenne, *J. Microsc.* **181**, 68-71 (1996). <https://onlinelibrary.wiley.com/doi/abs/10.1046/j.1365-2818.1996.96377.x>
- [102] J. A. Wilson and A. D. Yoffe, *Adv. Phys.* **18**, 193 (1969). <https://doi.org/10.1080/00018736900101307>

- [103] K. D. Bronsema, J. L. de Boer and F. Jellinek *Z. Anorg. Allg. Chem.* **540**, 15 (1986). <https://onlinelibrary.wiley.com/doi/10.1002/zaac.19865400904>
- [104] A. A. Al-Hilli and B. L. Evans, *J. Cryst. Growth* **15**, 93 (1972). <https://www.sciencedirect.com/science/article/pii/0022024872901297>
- [105] E. A. Wood, (Bell System Monograph No. 4680, 1964), *80 Diaperiodic Groups in Three Dimensions*. <https://onlinelibrary.wiley.com/doi/abs/10.1002/j.1538-7305.1964.tb04077.x>
- [106] L. Bawden, S. P. Cooil, F. Mazzola, J. M. Riley, L. J. Collins-McIntyre, V. Sunko, K. W. B. Hunvik, M. Leandersson, C. M. Polley, T. Balasubramanian, T. K. Kim, M. Hoesch, J. W. Wells, G. Balakrishnan, M. S. Bahramy and P. D. C. King, *Nat. Commun.* **7**, 11711 (2016). <https://www.nature.com/articles/ncomms11711>
- [107] P. Dey, Luyi Yang, C. Robert, G. Wang, B. Urbaszek, X. Marie and S.A. Crooker, *Phys. Rev. Lett.* **119**, 137401 (2017). <https://journals.aps.org/prl/abstract/10.1103/PhysRevLett.119.137401>
- [108] C. J. Ciccarino, T. Christensen, R. Sundararaman and P. Narang, *Nano Lett.* **18** (9), 5709-5715 (2018). <https://pubs.acs.org/doi/abs/10.1021/acs.nanolett.8b02300>

Biografija

Marko Milivojević je rođen 1989. godine u Jagodini. Srednju školu je završio u Beogradu 2008. godine. Iste godine upisao je Fizički fakultet Univerziteta u Beogradu, smer Teorijska i eksperimentalna fizika, koji je završio 2012. godine s prosečnom ocenom 9.63. Na istom fakultetu upisao je master studije 2012. godine na smeru Teorijska i eksperimentalna fizika. Položio je sve predviđene ispite sa prosečnom ocenom 10, a master rad pod naslovom "Spinske reprezentacije i uređenja linijskih grupa" odbranio je 2013. godine. Marko Milivojević je u periodu 2014-2016 bio angažovan kao istraživač pripravnik a od 2016. god. kao istraživač saradnik na Fizičkom fakultetu. Trenutno je angažovan na projektu "Niskodimenzionalne nanostrukture" Ministarstva prosvete, nauke i tehnološkog razvoja Republike Srbije.

Dosadašnja istraživanja Marka Milivojevića spadaju u naučnu oblast kvantna i matematička fizika. Osnovna tema je analiza spin-orbit efekata na elektronske osobine struktura periodičnih u jednom pravcu, čija je simetrija opisana linijskim grupama.

Прилог 1.

Изјава о ауторству

Потписани-а - **Марко Миливојевић**

број индекса - **2013/8006**

Изјављујем

да је докторска дисертација под насловом

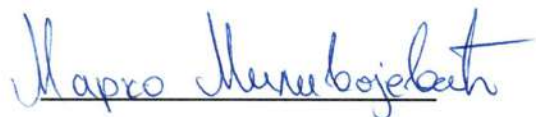
Spin-orbit interaction in low dimensional systems: symmetry based approach

(Спин-орбит интеракција у нискодимензионалним системима: симетријски приступ)

- резултат сопственог истраживачког рада,
- да предложена дисертација у целини ни у деловима није била предложена за добијање било које дипломе према студијским програмима других високошколских установа,
- да су резултати коректно наведени и
- да нисам кршио/ла ауторска права и користио интелектуалну својину других лица.

Потпис докторанда

У Београду, 16. 09. 2019.



Прилог 2.

Изјава о истоветности штампане и електронске верзије докторског рада

Име и презиме аутора - **Марко Миливојевић**

Број индекса - **2013/8006**

Студијски програм – **Квантна, математичка и нанофизика**

Наслов рада - **Spin-orbit interaction in low dimensional systems: symmetry based approach** (Спин-орбит интеракција у нискодимензионалним системима: симетријски приступ)

Ментор - **др Татјана Вуковић**

Изјављујем да је штампана верзија мог докторског рада истоветна електронској верзији коју сам предао/ла за објављивање на порталу **Дигиталног репозиторијума Универзитета у Београду**.

Дозвољавам да се објаве моји лични подаци везани за добијање академског звања доктора наука, као што су име и презиме, година и место рођења и датум одбране рада.

Ови лични подаци могу се објавити на мрежним страницама дигиталне библиотеке, у електронском каталогу и у публикацијама Универзитета у Београду.

Потпис докторанда

У Београду, 16. 09. 2019.



Прилог 3.

Изјава о коришћењу

Овлашћујем Универзитетску библиотеку „Светозар Марковић“ да у Дигитални репозиторијум Универзитета у Београду унесе моју докторску дисертацију под насловом:

Spin-orbit interaction in low dimensional systems: symmetry based approach (Спин-орбит интеракција у нискодимензионалним системима: симетријски приступ)

која је моје ауторско дело.

Дисертацију са свим прилозима предао/ла сам у електронском формату погодном за трајно архивирање.

Моју докторску дисертацију похрањену у Дигитални репозиторијум Универзитета у Београду могу да користе сви који поштују одредбе садржане у одабраном типу лиценце Креативне заједнице (Creative Commons) за коју сам се одлучио/ла.

1. Ауторство

2. Ауторство - некомерцијално

3. Ауторство – некомерцијално – без прераде

④. Ауторство – некомерцијално – делити под истим условима

5. Ауторство – без прераде

6. Ауторство – делити под истим условима

(Молимо да заокружите само једну од шест понуђених лиценци, кратак опис лиценци дат је на полеђини листа).

Потпис докторанда

У Београду, 16.09.2019.



1. **Ауторство** - Дозвољавање умножавање, дистрибуцију и јавно саопштавање дела, и прераде, ако се наведе име аутора на начин одређен од стране аутора или даваоца лиценце, чак и у комерцијалне сврхе. Ово је најслободнија од свих лиценци.

2. **Ауторство – некомерцијално.** Дозвољавање умножавање, дистрибуцију и јавно саопштавање дела, и прераде, ако се наведе име аутора на начин одређен од стране аутора или даваоца лиценце. Ова лиценца не дозвољава комерцијалну употребу дела.

3. **Ауторство - некомерцијално – без прераде.** Дозвољавање умножавање, дистрибуцију и јавно саопштавање дела, без промена, преобликовања или употребе дела у свом делу, ако се наведе име аутора на начин одређен од стране аутора или даваоца лиценце. Ова лиценца не дозвољава комерцијалну употребу дела. У односу на све остале лиценце, овом лиценцом се ограничава највећи обим права коришћења дела.

4. **Ауторство - некомерцијално – делити под истим условима.** Дозвољавање умножавање, дистрибуцију и јавно саопштавање дела, и прераде, ако се наведе име аутора на начин одређен од стране аутора или даваоца лиценце и ако се прерада дистрибуира под истом или сличном лиценцом. Ова лиценца не дозвољава комерцијалну употребу дела и прерада.

5. **Ауторство – без прераде.** Дозвољавање умножавање, дистрибуцију и јавно саопштавање дела, без промена, преобликовања или употребе дела у свом делу, ако се наведе име аутора на начин одређен од стране аутора или даваоца лиценце. Ова лиценца дозвољава комерцијалну употребу дела.

6. **Ауторство - делити под истим условима.** Дозвољавање умножавање, дистрибуцију и јавно саопштавање дела, и прераде, ако се наведе име аутора на начин одређен од стране аутора или даваоца лиценце и ако се прерада дистрибуира под истом или сличном лиценцом. Ова лиценца дозвољава комерцијалну употребу дела и прерада. Слична је софтверским лиценцама, односно лиценцама отвореног кода.